Die approbierte Originalversion dieser Diplom-/Masterarbeit ist an der Hauptbibliothek der Technischen Universität Wien aufgestellt (http://www.ub.tuwien.ac.at).

The approved original version of this diploma or master thesis is available at the main library of the Vienna University of Technology (http://www.ub.tuwien.ac.at/englweb/).

DIPLOMARBEIT

Impact of doping density in short-wavelength indium phosphide quantum cascade lasers

ausgeführt zum Zwecke der Erlangung des akademischen Grades eines Diplom-Ingenieurs

unter der Leitung von

a.o.Univ.Prof.Dr. Gottfried Strasser
Institut für Festkörperelektronik
E362

eingereicht an der Technischen Universität Wien
Fakultät für Elektrotechnik

von

Elvis Mujagić

Mat.Nr. 0225263
Steudelgasse 35/15
A-1100 Wien

Wien, im April 2007

Betreuer:

Dipl.Ing. Maximilian Austerer

a.o.Univ.Prof.Dr. Gottfried Strasser

Kurzfassung

$Quantenkaskaden\ Laser$ (QCLs) sind elektrisch gepumpte Halbleiterlaser für Wellenlängen im mittleren und fernen Infrarot. Im Gegensatz zu vielen Laserdioden bei denen die Lichterzeugung durch Rekombination der Elektronen mit den Löchern über die Bandlücke erfolgt, werden bei den QCLs die Intersubband-Übergänge zwischen Zuständen innerhalb des Leitungsbandes genutzt. Durch geignete Wahl der Halbleitermaterialien werden eindimensionale Heterostrukturen geschaffen. In den daraus resultierenden Quantentöpfen bilden sich Energiezustände aus, deren energetische Lage durch die Dicke der Töpfe bestimmt wird. Dieses ermöglicht einen enormen Freiheitsgrad bezüglich der Wahl der Emissionswellenlänge. QCLs zeichnen sich durch die Unabhängigkeit von der Bandlücke aus, aber auch durch die im Vergleich mit anderen Laserdioden viel geringere Temperaturabhängigkeit. Angetrieben durch eine Vielzahl von Anwendungen wie der Gasanalyse sowohl für umwelttechnische als auch medizinische Zwecke, Kommunikation und Militär, wurden QCLs für kurze Wellenlängen ($3 - 5\,\mu m$) demonstriert. Die besondere Herausforderung liegt in der Herstellung von Lasern, die bei Raumtemperatur im Dauerstrichbetrieb arbeiten.
Im Rahmen dieser Diplomarbeit wurden Laser hergestellt, deren Emissionslänge $3,8\,\mu m$ beträgt. Der Zugang zu dieser kurzen Wellenlänge wird durch den auf dem spannungskompensierten InGaAs/InAlAs/AlAs basiertem Heterostruktursytem ermöglicht, das auf einem InP Substrat aufgewachsen wurde. Um den Stromtransport zu ermöglichen werden QCLs dotiert, was auch deren Leistungsmerkmale bestimmt. Der Schwerpunkt dieser Arbeit lag in der Charakterisierung der Laser anhand ihrer elektrischen, optischen und thermischen Eigenschaften in Abhängigkeit von der Dotierungsdichte im Bereich von $0,7$ x $10^{17} cm^{-3}$ bis $3,9$ x $10^{17} cm^{-3}$. Die Messungen mehrerer Fabry-Perot QC laser bei 78 K ergaben eine maximale optische Ausgangsleistung von 1,6 W und einen maximalen Anstieg der Leistung von 1,12 W/A bei einer Dotierung von $1,7$ x $10^{17} cm^{-3}$. Für diese Dotierung wurden die grösste charakteristische Temperatur von $T_0^* = 294\,K$ als auch eine Leistungseffizienz von $3.63\,\%$ bei 78 K gemessen. Hierbei konnten die Laser im gepulsten Betrieb bis zur Raumtemperatur betrieben werden. Die Leistung bei 300 K betrug 10 mW. Die niedrigste Schwellstromdichte von $1,85\,kA/cm^2$ wurde bei einem mit $1,1$ x $10^{17} cm^{-3}$ dotiertem Laser erreicht. Der höchste Betriebsstrom der den dynamischen Bereich eines Lasers bestimmt, stieg von 4.54 A bis 18 A annähernd linear mir der Dotierung an. Während der Messungen wurde beobachtet, dass bei niedrig dotierten Proben die effektive Elektronendichte aufgrund von im Material vorhandenen Störstellen langsam reduziert wird, was eine stabile Funktion des Lasers verhindert.

Abstract

$Quantum\,cascade\,lasers$ (QCLs) are electrically pumped semiconductor lasers that emit in the mid- and far-infrared spectral region. In contrast to other laser diodes where the light is generated by recombination of electrons and holes across the band gap, in a QCL intersubband transitions between energy states within the conduction band are used. By means of diverse semiconductor materials one-dimensional heterostructures can be formed where the location of the energy states can be influenced by the thickness of the quantum wells. This provides a great freedom in tayloring the emission wavelength. Beside this band gap independence also the comparable low temperature influence is a further benefit of a QCL. Development of QCLs operating at short wavelength (3-5 μm) is driven by a number of applications including gas sensing for both environmental and medical uses, communication, and military countermeasures. Room temperature continuous wave operation has proven to be very challenging.
Within this work QCLs emitting at 3.8 μm were processed and investigated by means of electrical, optical and thermal characterization. These lasers are based on InGaAs/InAlAs/AlAs heterostructures grown strain-compensated on an InP substrate. In general the active region of a QCL is doped in order to provide electron transport. This also determines the performance of the laser. However, the characterization was focused on the influence of the doping density on the lasing properties in the range of 0.7 x $10^{17} cm^{-3}$ to 3.9 x $10^{17} cm^{-3}$. Several Fabry-Perot lasers were characterized, showing a clear dependence of optical power as well as threshold current density on doping density. Maximum values in case of peak optical power and slope eficiency of 1.6 W and 1.12 W/A, respectively, were observed for a doping level of 1.7 x $10^{17} cm^{-3}$ at 78 K. For this doping level also the highest characteristic temperature of $T_0^* = 294\,K$ and a wall-plug efficiency of $3.63\,\%$ at 78 K were obtained. In this case lasing was observed up to 300 K under pulsed condition. On the other hand lowest threshold current density was measured for a 0.7 x $10^{17} cm^{-3}$ doped sample. The maximum operating current increased almost linearly with doping concentration from 4.54 A to 18 A. The measurements showed that low doped lasers suffer from a reduced effective electron density due to traps in the material, thus avoiding stable lasing performance.

Contents

1 Introduction 3

1.1 Quantum cascade lasers 4

1.2 Thesis outline 6

2 Semiconductor physics 8

2.1 III-V compound semiconductors 8

2.1.1 Crystal structure 8

2.1.2 Band structure 8

2.1.3 Ternary InGaAs/InAlAs compounds 10

2.2 The Effect of the strain on the band structure 12

2.2.1 Critical layer thickness 12

2.2.2 Pseudomorphic growth 13

2.3 InGaAs/InAlAs heterostructures 17

2.3.1 Calculation of energy states 18

2.3.2 Intersubband scattering mechanism 20

2.3.3 Carrier transport 21

2.3.4 Population dynamics and threshold current density 22

3 Mid-infrared quantum cascade lasers 24

3.1 QCL design 24

3.1.1 Active zone 24

3.1.2 Injector 26

3.1.3 Strain-compensated structures 28

3.1.4 Cascading effect 32

3.2 Laser resonator 32

3.2.1 Optical constants 33

3.2.2 Vertical confinement 34

3.2.3 Lateral confinement 36

3.2.4 Fabry-Perot cavity 36

4 Fabrication and Characterization of QCLs 40
4.1 Technology 40
4.1.1 Molecular Beam Epitaxy 40
4.1.2 Reactive ion etching 43
4.1.3 Deposition technologies 46
4.2 Processing 49
4.3 Characterization 55
4.3.1 Electrical and optical measurement setups 55
4.3.2 Experimental results 58

5 Summary and outlook 70

A Appendix: Material parameters 72

References 74

Conference contributions 80

Chapter 1

Introduction

The first documented discussion of the possibility of light amplification by the use of stimulated emission in a semiconductor was made in an unpublished manuscript by John von Neumann in 1953 [1]. In this paper, von Neumann discussed using carrier injection across a p-n junction as one possibility of achieving stimulated emission in semiconductors, and calculated the radiation transition between two Brillouin zones.
In late 1962, the operation of homojunction semiconductor injection lasers based on a GaAs-material system was reported by several groups [2], [3], [4]. The drawbacks of these lasers where the light emission takes place due to radiative electron-hole recombination, were the poor carrier confinement and the high losses in the cladding layers. However, the progress of fabrication technologies allowed the enhancement of lasing properties. The advent of molecular beam epitaxy [5], [6] was an important step towards improving confinement of electrons and light by growing heterostructures with thickness control of atomic monolayers. As a consequence, this progress resulted in pulsed room temperature operation [7], [8] and finally in continous wave operation [9] of electrically driven semiconductor lasers.
Although, in principle the wavelength of the band gap semiconductor lasers can be designed by using diverse materials [10], [11], [12], the realization of long wavelength light emitters suffers from an increase of non-radiative scattering mechanism with decreasing band gap. An approach to avoid this restriction was done by demonstration of the first quantum cascade lasers in 1994 [13], which are based on intersubband transitions, allowing to design the wavelength in the mid-infrared region independent of the band gap energy. For further improvements of lasing properties it is desirable to investigate the influences of the relevant physical and technological parameters. In this diploma thesis the influence of the active region doping in QCLs is presented.

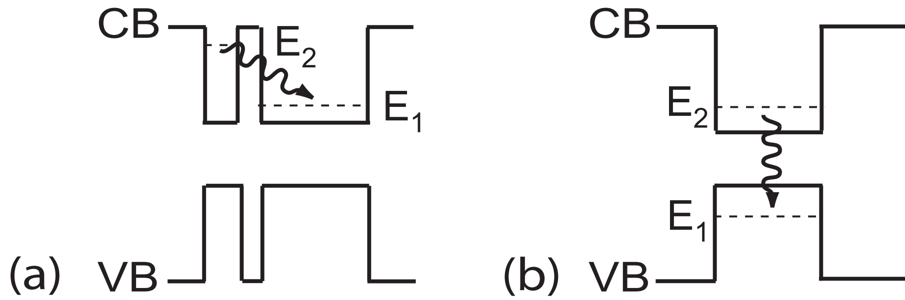

Figure 1.1: (a) Intersubband transition between two energy states in the conduction band. (b) Interband electron-hole recombination in a quantum well.

1.1 Quantum cascade lasers

The quantum cascade laser (QCL) is an electrically pumped semiconductor laser that emits in the mid-infrared region of the electromagnetic spectrum ($3\,\mu m - 15\,\mu m$). Unlike most semiconductor injection lasers that are based on electron-hole recombination to generate electromagnetic radiation, QCLs are unipolar devices that utilize intersubband transitions (Fig. 1.1) in a repetition of identically coupled multi-quantum-well structures.
The principle of a QCL is based on two fundamental quantum effects, namely carrier confinement and tunneling through barriers. In contrast to conventional band gap lasers these unipolar devices involve only one kind of carriers. Due to this fact the transition takes place between two sub-levels in the valance or conduction band (CB), allowing a wavelength design independent of the band gap energy. The emission spectra of the intraband (or intersubband) transitions are narrower compared to conventional semiconductor lasers (Fig. 1.2), which can be explained by the quasi-parabolic shape of the sub-bands. In QCLs transitions of electrons at unequal in-plane momenta contribute to the same wavelength. The deviation from the Dirac shaped spectra is given by scattering processes (homogeneous broadening) and growth imperfections yielding a spread in well thicknesses (inhomogeneous broadening).
In band gap lasers interband transitions off the close-to-zero in-plane-momentum lead to a broadening of the linewidth. The reason is the opposite curvature of the conduction and valence band (VB). In this case the rise of the quasi-Fermi levels ($E_{f,c}, E_{f,v}$) due to the carrier injection results in a comparable broadband photon emission.
The possibility of the amplification of electromagnetic waves in a semiconductor superlattice structure, was predicted first by Kazarinov and Suris theoretically [14], [15]. Initially the realisation of devices based on this theory failed due to the absence of adequate technologies and a deeper understanding of the underlying physics. The advances in epitaxial growth of semiconductor layers providing nanometer thickness control, led to the first experimental demonstration of a QCL by Faist *et al.* at the Bell Laboratories [13]. This QCL was realized as

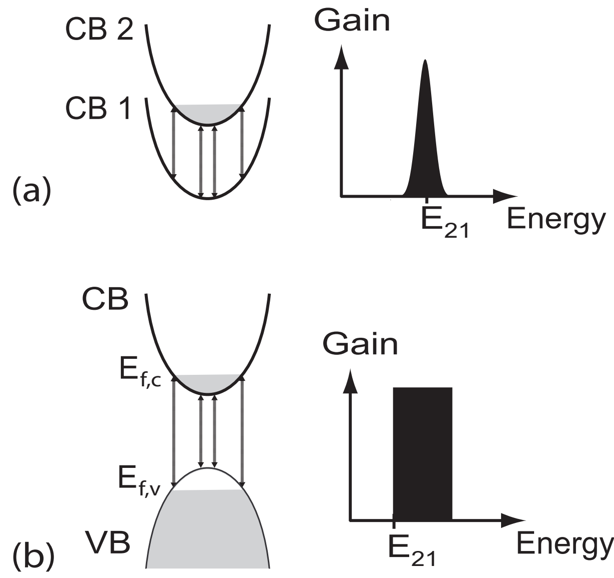

Figure 1.2: (a) Intersubband transition between two conduction subbands CB1 and CB2. The energies (indicated as arrow lengths) are almost equal for small in-plane wavevectors, yielding to a narrow gain spectrum. (b) The opposite curvature of the valence and conduction band leads to broader transition linewidth, since the quasi-Fermi levels $E_{f,v}$ and $E_{f,c}$ depend on the injected carriers.

an InAlAs/InGaAs superlattice structure grown on an InP substrate operating at a wavelength of 4.2 μm. Apart from this material system, first intersubband electroluminescence based on a GaAs semiconductor compound was presented in 1997 [16] followed by the demonstration of GaAs-QCLs [17], [18]. Since then there has been tremendous progress in QCL research, which has resulted in bidirectional [19], multiwavelength [20], ultrabroadband [21], above room-temperature continous operation [22], [23], operation in the terahertz region [24] and to the demonstration of short wavelength QC lasers [25], [26].
Fig. 1.3 gives a shematic view describing the principle of a QCL. One period consists of an injector and an active cell. Based on the tunneling effect electrons stream down a staircase of quantum wells and barriers, formed by the conduction band of the semiconductor heterostructures. The n-doped injector, providing an electron reservoir and preventing space charge formation, fills the upper laser level 3. The transition between levels 3 and 2 leads to a photon emission with an energy E_{32} corresponding to an emission wavelength

$$\lambda = \frac{hc}{E_{32}} \tag{1.1}$$

where h is the Planck constant and c the velocity of light in vacuum. The condition of stimulated emission is fulfilled by achieving population inversion across levels 3 and 2. This is ensured by a longer upper level-lifetime of few picoseconds compared to level 2 in the range

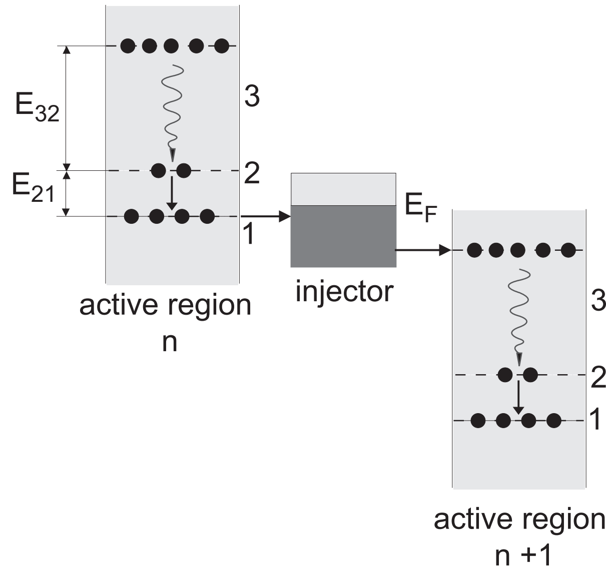

Figure 1.3: A schematic illustration of the QCL principle. Two active regions and an injector are shown. Level three of the left lasing region is populated by electrons from the preceding injector. The wavy arrow indicates the radiative transition between levels 3 and 2 resulting in a photon emission with energy E_{32}. Lower laser level 2 is depleted to level 1 via optical phonon emission ($E_{21} = \hbar\omega_{LO}$). Electrons travel from the ground level 1 through the adjacent injector to the upper laser level of the next lasing region.

of some 100 fs. The energy seperation E_{21} is chosen to be close to the longitudinal-optical (LO) phonon energy in order to achieve an efficient depopulation of the lower laser level by LO-phonon emission. The electrons from level 1 travel through the adjacent injector into the upper laser level of the next active region. Thus cascading the active region yields a multi-photon emission.

1.2 Thesis outline

After a short introduction in chapter one, chapter two starts with the physical aspects of III/V semiconductor compounds used in this work, concentrating on crystal structure and band structure. Futhermore the ternary InGaAs/InAlAs compounds are introduced and the strain effect in case of non-lattice matched growing of epilayers is discussed. This chapter closes with the calculation of the electronic states in semiconductor heterostructures as well as with the aspects of scattering mechanisms and transport properties.
Chapter three is dedicated to the design of quantum cascade lasers emitting in the mid-infrared region. First, several active region designs are presented including a discussion according to the advantages and drawbacks of each design. The injector, as a part of the active region,

acting as an electron reservoir is another point of discussion. In addition the properties of strain-compensated heterostructures, playing an important role in short wavelength QCLs, are described. The last part of this chapter treats the optical waveguide structures. This includes the discussion of the optical properties of the materials as well as the calculation of the waveguide modes in Fabry-Perot laser cavities providing a multi-mode emission spectrum.
Chapter four deals with the fabrication and characterization of the QCLs. Several technologies like gas-source molecular beam epitaxy, reactive ion etching and diverse deposition methods are presented in this chapter. Then a detailed description of the processing steps is given followed by a section about the electrical and optical measurement setups. Finally the experimental results regarding the doping dependent performance is presented.

Chapter 2

Semiconductor physics

In this chapter the physical properties of III-V compound semiconductors are presented. Starting with the description of the crystal structure and the explanation of the band structure, an introduction into the InGaAs/InAlAs material system is given. The effect of strain on band structure is discussed in detail. The last part of this chapter is dedicated to the electronic basics of heterostructures.

2.1 III-V compound semiconductors

The QCL design used in this thesis is based on gallium arsenide (GaAs), aluminium arsenide (AlAs), indium arsenide (InAs), indium phosphide (InP) as well as their ternary compounds. These are all III-V semiconductors, given the group III origin of Ga, Al and In, and the group V origin of As and P.

2.1.1 Crystal structure

At room temperature and ambient pressure all mentioned materials take up the zink blende structure which can be treated as *face-centered* cubic lattices with two atomic layers per unit cell (Fig. 2.1(a)). Figure 2.1(b) shows the *body-centered* reciprocal lattice. The first Brillouin zone, defined as the primitive cell of the reciprocal lattice, is centered at the high symmetry Γ-point at $\vec{k} = (0, 0, 0)$. Other symmetry points are X and Λ with $\langle 100 \rangle$ and $\langle 111 \rangle$ directions, respectively.

2.1.2 Band structure

In order to describe the electronic properties of such a crystal one has to solve the many-ion many-electron Schrödinger equation. The complexity of such a problem can be reduced by

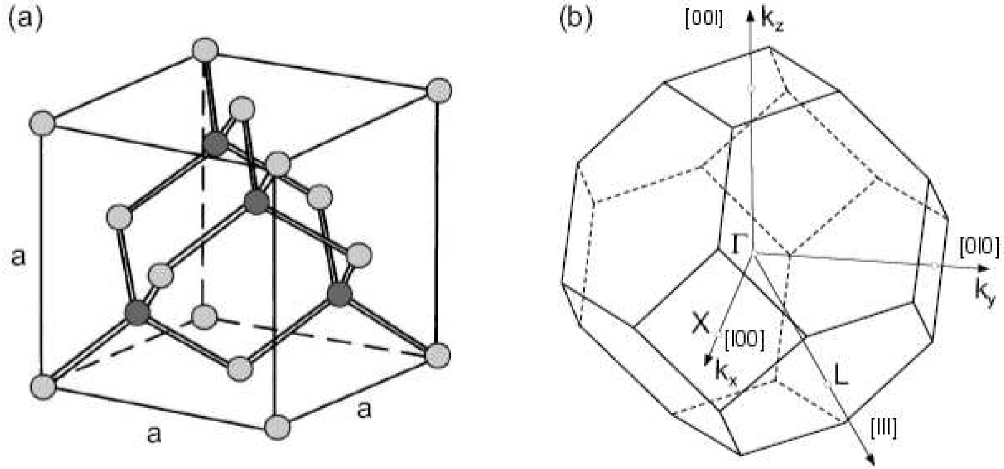

Figure 2.1: (a) Zinc blende structure of III/V semiconductors. (b) First Brillouin zone of the zinc blende structure with the most important symmetry-points and -lines [27].

the assumption that the ions are regarded as rigidly fixed at their lattice sites and any one of the valence electrons is treated to move in a potential formed by the ions and all other electrons. This yields the one-electron Schrödinger equation:

$$\left\{-\frac{\hbar^2}{2m_e}\nabla^2 + V(\mathbf{r})\right\}\psi_n(\mathbf{r}) = E_n\psi_n(\mathbf{r}) \tag{2.1}$$

where $\hbar = h/2\pi$ is the reduced Planck constant, m_e the electron mass and $E_n = E_n(\mathbf{k}) = \hbar^2 k^2/2m_e$ the energy values. The integer n refers to a countable set of solutions. Bloch's theorem for a periodic one-electron potential $V(\mathbf{r})$, states that the eigenfunctions $\psi_n(\mathbf{r})$ are given by

$$\psi_n(\mathbf{r}) = \exp{(i\mathbf{kr})}u_n(\mathbf{k},\mathbf{r}) \tag{2.2}$$

and have the same form as plane waves $\exp{(i\mathbf{kr})}$ multiplied by the function $u_n(\mathbf{k},\mathbf{r})$ which is normalized over the volume V and has the same periodicity as the potential. The associated energy relation $E_n(\mathbf{k})$ is known as the energy band structure.

Figure 2.2 illustrates the calculated band structures of GaAs, AlAs and InAs within the first Brillouin zone [28], [27]. Both GaAs and InAs are $direct\,semiconductors$, as the highest valence band states and the lowest conduction band states are at the same point Γ in the Brillouin zone. In contrast AlAs is an $indirect\,semiconductor$ with the lowest conduction band at the X point and the highest valence band at the Γ point. The energy difference between these two characteristic states is defined as the $band\,gap\,energy$. At $T = 300K$ the band gap energies of GaAs, AlAs and InAs are $E_g = 1,424\,eV$, $2,17\,eV$ and $0,36\,eV$, respectively [29].

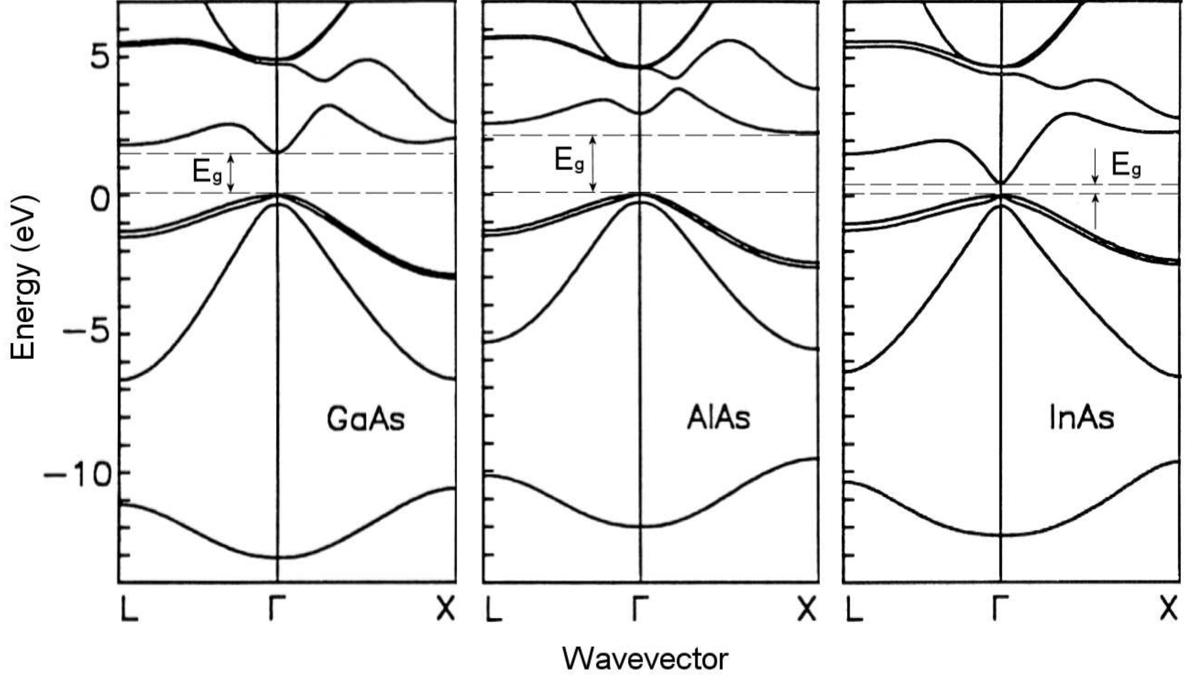

Figure 2.2: Calculated energy band structures of the III/V semiconductor compounds GaAs, AlAs and InAl within the first Brillouin zone [27].

2.1.3 Ternary InGaAs/InAlAs compounds

By replacing any fraction of group-III elements gallium or aluminium (in GaAs or AlAs, respectively) by indium, InGaAs or InAlAs semiconductors are formed, which belong to the $ternary$ semiconductor compounds. The material system used in this work is based on $\mathrm{In}_x\mathrm{Ga}_{1-x}\mathrm{As}$ and $\mathrm{In}_y\mathrm{Al}_{1-y}\mathrm{As}$, where fraction x (y) of Ga (Al) is substituted by In. The lattice parameter a of a ternary semiconductor compound $\mathrm{A}_x\mathrm{B}_{1-x}\mathrm{C}$ is given by linear interpolation of the binary compounds AC and BC corresponding lattice parameters:

$$a(A_xB_{1-x}C) = xa(AC) + (1-x)a(BC) \tag{2.3}$$

For both dicussed ternary alloys, the dependence of the energy gap on alloy composition is assumed to fit a simple quadratic form:

$$E_g(A_xB_{1-x}C) = xE_g(AC) + (1-x)E_g(BC) - x(1-x)\mathcal{C}_{E_g} \tag{2.4}$$

where the so-called ”bowing parameter” $\mathcal{C}_{E_g}$ accounts for the deviation from a linear interpolation. The semiconductor parameters used within this thesis can be found in appendix A. Figure 2.3 depicts the dependance of the band gap energy on the lattice parameter at $T = 300\,K$ for different binary III/V semiconductors. The connection lines denote the band gap behaviour of ternary semiconductor compounds.

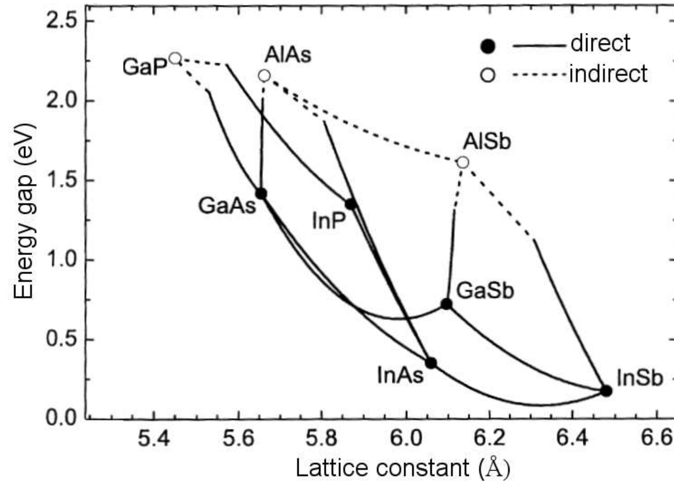

Figure 2.3: The various binary III/V semiconductors plotted as a function of lattice constant and energy gap at $T = 300\,K$. The full lines indicate a direct-gap ternary semiconductor and the broken lines indicate an indirect-gap ternary semiconductor [30].

The main advantage of the InGaAs/InAlAs/InP material system compared to the GaAs/AlGaAs-based system are the lower effective mass resulting in a higher oscillator strength and a longer optical phonon lifetime. Since InP has lower refractive index compared to the active region, it can be used as a waveguide. This fact leads to a waveguide design where the active material can be directly deposited on the substrate, providing an efficient optical confinement. In contrast GaAs has the highest refractive index in the GaAs-based system. The sophisticated growth and processing technology of GaAs make this material attractive for fabricating well-engineered waveguide structures. $In_xGa_{1-x}As/In_yAl_{1-y}As$ structures grown lattice matched on InP substrate can be realized with In contents of $x = 0.53$ and $y = 0.52$. In this case, following equation 2.4, the band gap energies of $In_{0.53}Ga_{0.47}As$ and $In_{0.52}Al_{0.48}As$ are 0.74 eV and 1.45 eV, respectively. In figure 2.4 the band gap energies are plotted versus the mole fraction. Note that AlAs turns from an indirect semiconductor to a direct InAlAs material for a certain indium fraction.

For short-wavelength QCLs treated in this work, a high transition energy is necessary, which is limited by the conduction band discontinuity given by the lattice matched system. An approach to avoid or at least push this limitation to higher energies by making use of the strain effect in heterostructures, is discussed in the next section.

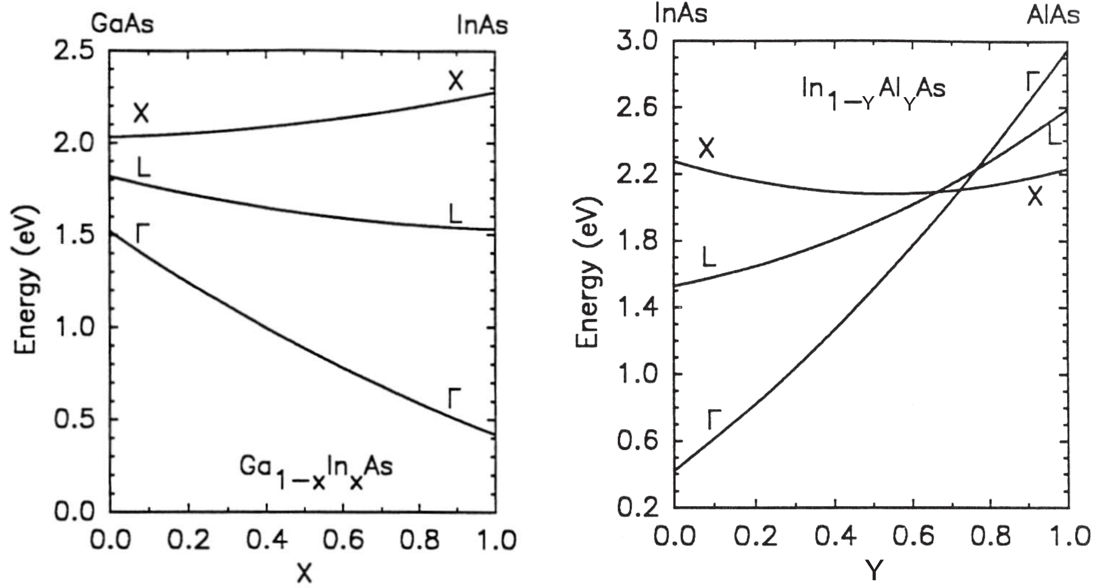

Figure 2.4: Conduction-band energy minima at Γ,X and L relative to the top of this valence band as functions of alloy compositions X and Y in $\mathrm{In}_x\mathrm{Ga}_{1-x}\mathrm{As}$ and $\mathrm{In}_y\mathrm{Al}_{1-y}\mathrm{As}$, respectively [27].

2.2 The Effect of the strain on the band structure

Using appropriate growth technologies like molecular beam epitaxy (MBE) and metal organic vapor phase epitaxy (MOVPE), thin semiconductors layers can be grown on a substrate material. When a thin film of a semiconductor with a lattice constant different from that of the substrate is grown, one can loosely characterize two regions. If the thickness of the overlayer is small, the layer is under biaxial strain where the in-plane lattice constant is the same as that of the substrate. If the overlayer thickness is too large, the layer has a network of disslocations. The thickness separating these two regions is called the critical thickness and varies inversely with the lattice mismatch between the substrate and the overlayer. In the following the physics associated with the strain and the effect on the electronic structure is discussed.

2.2.1 Critical layer thickness

If the missfit between a grown epilayer and a substrate is sufficiently small, the first atomic layers which are deposited will be strained to match the substrate and a coherent interface will be formed. But, as the layer thickness increases, the homogeneous strain energy becomes larger. As a specific thickness is reached, it becomes energetically favourable to introduce misfit dislocations.

The existence of this critical thickness was first discussed by van the Merwe [31] using a

one-dimensional lattice to determine the critical lattice-mismatch for defect formation. However, a much more simple and more easily utilized mismatch epitaxy theory was developed by J. W. Matthews and A. E. Blakeslee introducing the $mechanical\, equilibrium\, theory$ [32]. In this theory the mechanical equilibrium of a grown-in substrate threading dislocation determines the onset of interfacial misfit dislocations. By balancing the forces on a pre-existing dislocation an expression for the critical thickness d_c can be derived:

$$d_c = \frac{b(1 - v cos^2 \beta_1)}{8\pi(1 + v) cos \beta_2} \left[ln \left(\frac{d_c}{b} \right) + 1 \right] \left| \frac{a_0}{a - a_0} \right| \tag{2.5}$$

where $b = a_0\sqrt{2}$ is the absolute value of the dislocation Burgers vector **b**. The intrinsic lattice parameter is given by a and a_0 for epilayer and substrate, respectively. In the zink blende crystal structure Burgers vectors have 60° dislocations, defining $\beta_1 = \beta_2 = 60°$ [33]. The Poisson ratio reads $v = C_{12}/(C_{11} + C_{12})$. C_{11} and C_{12} are the elastic constants of the epilayer.

The theory developed by R. People and J. C Bean states that the substrate is initially free of threading dislocations [34]. Values for the critical layer thickness are obtained by assuming an interfacial misfit dislocation which is generated when the arial strain energy density of the film exceeds the self-energy of an isolated screw dislocation at a certain distance from the free surface. In this case one reads

$$d_c = \frac{b^2(1 - v)}{16\pi\sqrt{2}(1 + v)} ln \left(\frac{d_c}{b} \right) \left| \frac{a_0}{a - a_0} \right|^2 \tag{2.6}$$

with same parameters as used in equation 2.5.

Figure 2.5 shows the calculated critical thicknesses for $In_xGa_{1-x}As/In_yAl_{1-y}As$ against the In-content x, following the previously mentioned theories. The vertical dashed lines indicate the situation of structures grown on InP lattice matched, corresponding to $x = 0.53$ and $y = 0.52$. Due to neglecting the threading dislocations in the substrate, there is a clear deviation of calculated values using People and Bean equation compared to Matthews and Blakeslee model.

2.2.2 Pseudomorphic growth

Growing of semiconductor heterostructures is not only possible for lattice-matched materials, but even for those one which differ in lattice constant by several percent. This so-called $pseudomorphic\, growth$ is characterized by an in-plane lattice parameter which remains the same throughout the structure but changes perpendicular to the growth direction. In this case the lattice constant of the epilayers is fitted to that of the relatively thick substrate. These strains can cause profound changes in the electronic properties, and therefore provide extra flexibility in device design.

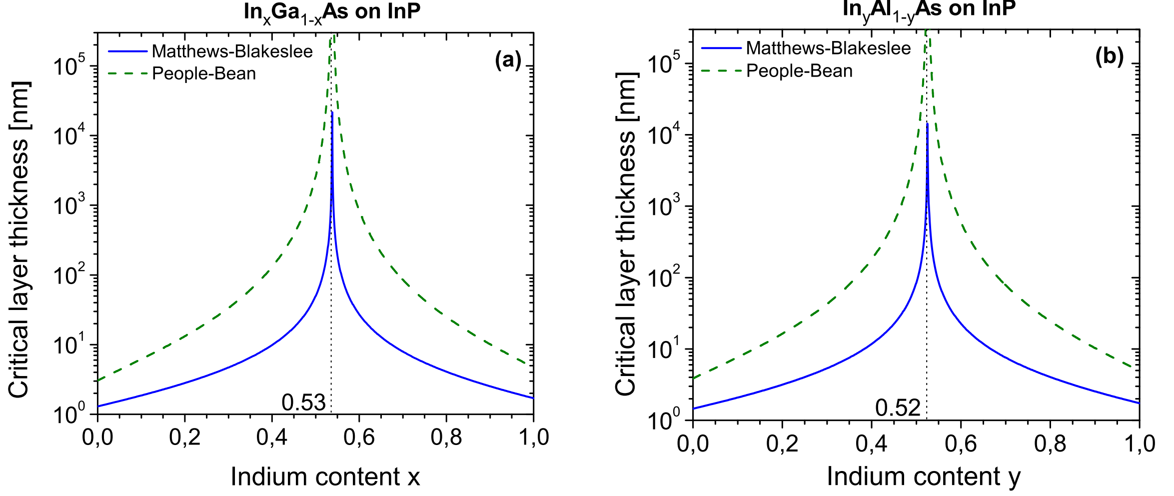

Figure 2.5: Calculated critical thicknesses of (a) $\mathrm{In}_x\mathrm{Ga}_{1-x}\mathrm{As}$ and (b) $\mathrm{In}_y\mathrm{Al}_{1-y}\mathrm{As}$ grown on InP versus indium fraction x and y, respectively. Calculations were done using equations 2.5 (model of Matthews and Blakeslee, solid line) and 2.6 (model of People and Bean, dashed line).

Figure 2.6 shows an epilayer growth with lattice parameter a on a substrate with latice constant a_0. If $a < a_0$ the layers will exhibit tensile strain in contrast to an epilayer with $a > a0$. In this case the lattice is compressed in order to match the substrate geometry.
Assuming the interface orientation (001), the lattice constant $a_\perp$ perpendicular to the growth direction can be written as:

$$a_\perp = a\left[1 - 2\frac{C_{12}}{C_{11}}\left(\frac{a_0 - a}{a}\right)\right] \tag{2.7}$$

With this result we can calculate the strain components $\epsilon_\parallel$ parallel and $\epsilon_\perp$ perpendicular to the plane of the interface [35]:

$$\epsilon_\parallel = \frac{a_\parallel}{a} - 1 = \frac{a_0 - a}{a} \tag{2.8}$$

$$\epsilon_\perp = \frac{a_\perp}{a} - 1 = \frac{a_\perp - a}{a} = -2\frac{C_{12}}{C_{11}}\left(\frac{a_0 - a}{a}\right) \tag{2.9}$$

In general, if a thin layer is grown on a substrate the value $a_\parallel$ is determined by the substrate, thus $a_\parallel = a_0$ is assumed in equation 2.8.
This deformation of the cubic unit cell results in a relative volume change

$$\frac{\Delta\mathcal{V}}{\mathcal{V}} = 2\epsilon_\perp + \epsilon_\parallel = 2\left(1 - \frac{C_{12}}{C_{11}}\right)\left(\frac{a_0 - a}{a}\right) \tag{2.10}$$

The biaxial strain has two components. One ist the $hydrostatic$ part which enters into the overall band lineups by an isotropic volume change of the cubic unit cell. The $nonhydrostatic$

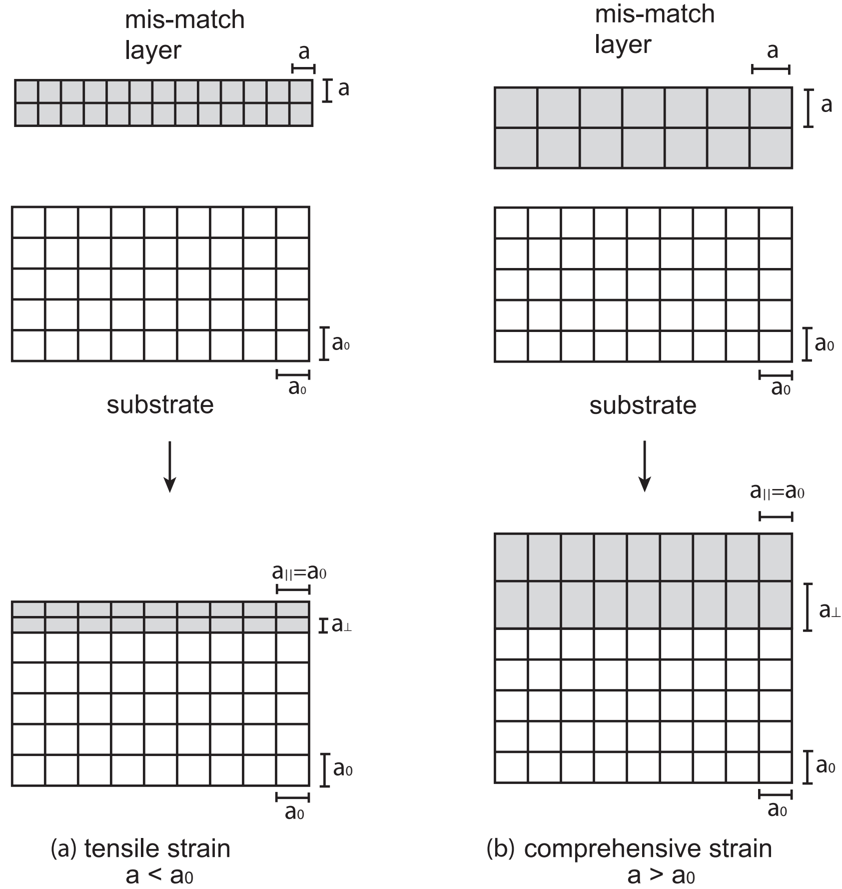

Figure 2.6: Schematic demonstration of a pseudomorphic growth of epilayers with lattice constant a on a substrate with lattice constant a_0. Tensile strain is introduced for (a) $a < a_0$ and if (b) $a > a_0$ the layers will exhibit comprehensive strain.

strain component ($shear\ strain$) leads to a tetragonal deformation of the crystal which causes splittings of degenerate bands (Fig. 2.7).
The hydrostatic potential leads to a shift of the conduction band and the heavy-holes (HH), light-holes (LH) and the splitt-off (SO) valence bands. The corresponding shifting energies are given by ΔE_{CB}^{hyd} and ΔE_{VB}^{hyd}, respectively.

$$\Delta E_{CB}^{hyd} = a_C \frac{\Delta \mathcal{V}}{\mathcal{V}} \tag{2.11}$$

$$\Delta E_{VB}^{hyd} = a_V \frac{\Delta \mathcal{V}}{\mathcal{V}} \tag{2.12}$$

For the III-V semiconductors the hydrostatic deformation potentials a_C and a_V are defined as $a_C < 0$ and $a_V > 0$ (for conduction and valence bands, respectively) [35].
Important effects on the band structure also occur, however, due to the shear strains which break the symmetry and split otherwise degenerate HH- and LH-bands at the Γ point. The

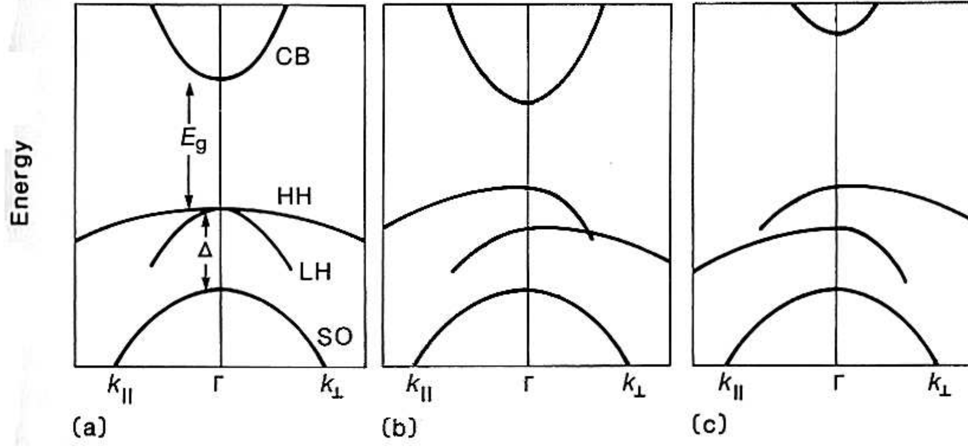

Figure 2.7: Illustration of the influence of strain on the band structure, according to [35]. (a) Lattice matched condition. Shift of the conduction band and the splitting of degenerated heavy holes (HH) and light holes (LH) bands in presence of (b) tensile and (c) compressive strain. Taken from [30].

additional energy shifts ΔE_{HH}^{tet}, ΔE_{LH}^{tet} and ΔE_{SO}^{tet} for the HH-, LH- and SO-bands are given by

$$\Delta E_{HH}^{tet} = \frac{1}{3}\Delta_{SO} - \frac{1}{2}\delta E \tag{2.13}$$

$$\Delta E_{LH}^{tet} = -\frac{1}{6}\Delta_{SO} + \frac{1}{4}\delta E + \frac{1}{2}\sqrt{\Delta_{SO}^2 + \Delta_{SO}\delta E + \frac{9}{4}(\delta E)^2} \tag{2.14}$$

$$\Delta E_{SO}^{tet} = -\frac{1}{6}\Delta_{SO} + \frac{1}{4}\delta E - \frac{1}{2}\sqrt{\Delta_{SO}^2 + \Delta_{SO}\delta E + \frac{9}{4}(\delta E)^2} \tag{2.15}$$

with

$$\delta E = -2b^{tet}\left(1 - \frac{C_{12}}{C_{11}}\right)\left(\frac{a_0 - a}{a}\right) \tag{2.16}$$

where b^{tet} is the shear deformation potential for a strain of tetragonal symmetry. For all semiconductors discussed in this work it is defined as $b^{tet} < 0$ [35]. Δ_{SO} is the spin-orbit splitting. Figure 2.8 clarifies the influence of strain on the band structure. In case of tensile strain ($a < a_0$) the conduction band and all valence bands are shifted by $\Delta E_{CB}^{hyd} < 0$ and $\Delta E_{VB}^{tet} > 0$, respectively. Due to $\delta E > 0$ the relation $\Delta E_{LH}^{tet} > \Delta E_{HH}^{tet}$ is given and the shear strain causes a splitting of degenerated bands. This results in a band gap energy defined by the conduction and the LH-valence band (Fig. 2.8(a)). An epilayer growth with a lattice constant larger than that of the substrate ($a > a_0$) leads to $\Delta E_{CB}^{hyd} > 0$ and $\Delta E_{VB}^{hyd} < 0$. Here, $\delta E < 0$ gives $\Delta E_{HH}^{tet} > \Delta E_{LH}^{tet}$. The band gap is limited by the conduction and the HH-valence band (Fig. 2.8(b)). In general hydrostatic strain has no influence on the conduction band.

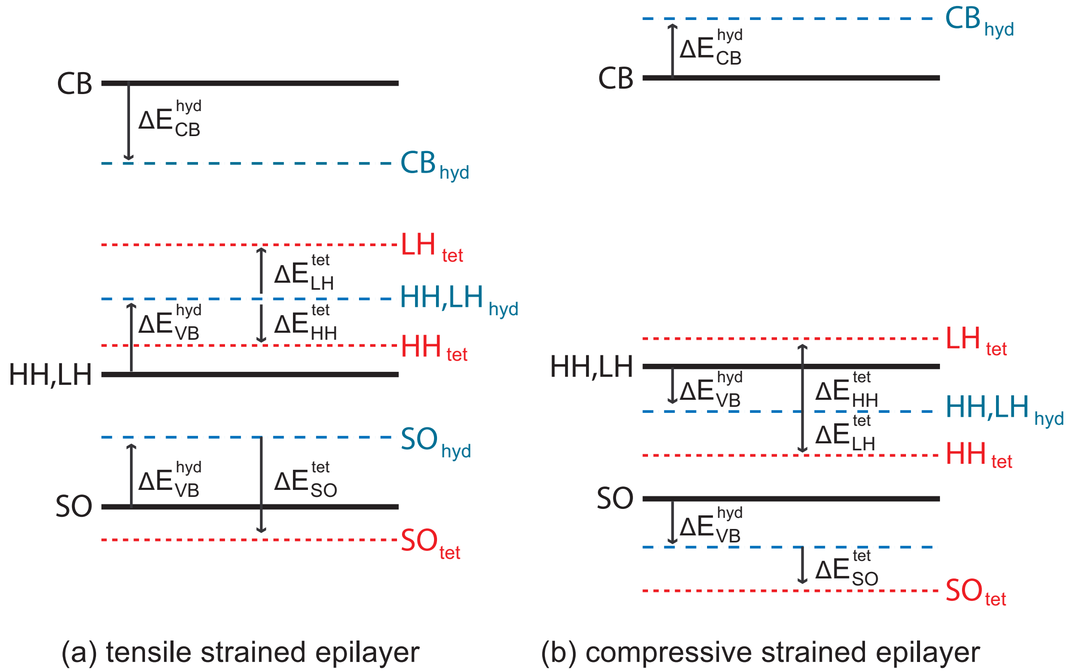

Figure 2.8: Schematic description of the energetic shift due to the hydrostatic and shear strain in case of (a) tensile and (b) compressive strained epilayers.

2.3 InGaAs/InAlAs heterostructures

When different materials A and B are grown on the same substrate, the structure is called a $heterostructure$, which characteristics strongly depend on the physical and chemical properties of both materials. In this thesis quantum wells of type I heterostructures based on the InGaAs/InAlAs-material system are considered (Fig. 2.9). In this case the conduction band of semiconductor B with a smaller band gap becomes a minimum and the valence band a maximum, and therefore electrons and holes are confined in this region. The regions of the conduction band minimum and maximum are called the $well\ layer$ and $barrier\ layer$. When the barrier layer is thick enough, electrons are not able to penetrate and are confined in the quantum well region resulting in quantization of the electron motion perpendicular to the heterointerface, forming a subband structure. For the Γ valley, the conduction band offset between InGaAs/InAlAs is about 70% of ΔE_g and hence in the valence band about 30% [36]. For the lattice matched $In_xGa_{1-x}As/In_yAl_{1-y}As$ heterojunction system $\Delta E_C = 520\,meV$ is given [37]. This larger offset makes the conduction band more interesting for a QCL design than the valence band. All QCLs presented in this work are based on this fact.

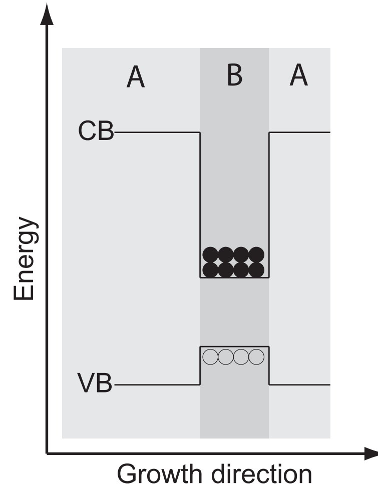

Figure 2.9: Type I interface in heterostructures.

2.3.1 Calculation of energy states

An understanding of the basic effects is best obtained by considering $ideal\ quantum\ confinement$ conditions, for which the elementary excitations are completely confined inside the microstructure and the electronic wave functions vanish beyond the surfaces (Fig. 2.10(a)). For this idealized situation, we can write the confinement potential as

$$V(z) = \begin{cases} 0 & \text{for } |z| \leq L/2 \\ \infty & \text{for } |z| \geq L/2 \end{cases} \tag{2.17}$$

where L stands for the quantum well thickness. Then the electron wave functions (envelope functions) $\phi_n(z)$ are obtained by solving the one-electron Schrödinger equation:

$$-\frac{\hbar^2}{2m_0^*}\frac{d^2}{dz^2}\phi_n(z) = E_n\phi_n(z) \tag{2.18}$$

The corresponding eigenvalues are given by

$$E_n = \frac{\hbar^2\pi^2}{2m_0^*} \cdot \frac{n^2}{L} \tag{2.19}$$

where m_0^* is the electron effective mass and n is the quantum number of the well. A more realistic description has to include the finite barrier heights due to the limited conduction band (or valence band) offset, leading to

$$V(z) = \begin{cases} 0 & \text{for } |z| \leq L/2 \\ V_c & \text{for } |z| \geq L/2 \end{cases} \tag{2.20}$$

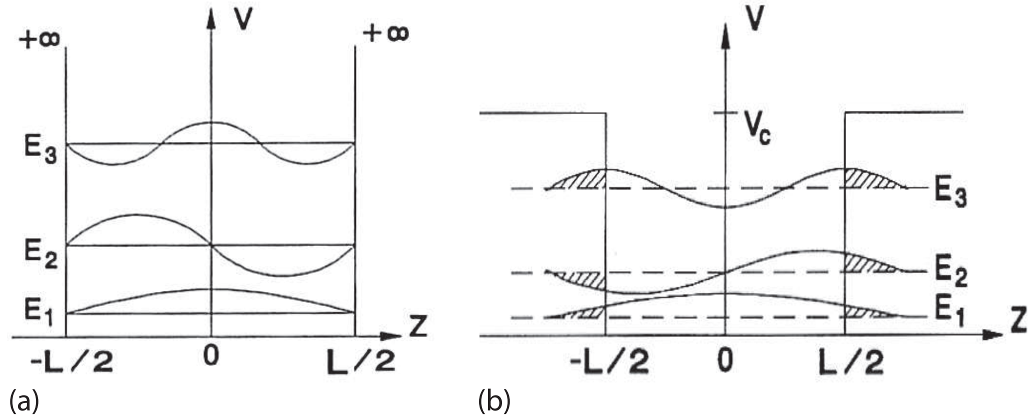

Figure 2.10: (a) Simplified quantum well model and electronic states with infinite potential barrier. (b) More realistic description incorporating finite barrier height due to a limited conduction band offset [38].

This leads to somewhat lower subband energies and a penetration of the wavefunction into the barrier material. Figure 2.10(b) shows that the wavefunctions inside the barriers are not vanishing, giving a rise to a finite tunneling probability, if barriers are thin enough. The analysis follows closely the treatment of the infinite potential, with the Schrödinger equation for the (x, y) motion being unchanged. However, including the finite potential and the material dependent electron effective masses $m_0^*(z)$, one reads:

$$\left\{-\frac{\hbar^2}{2}\frac{d}{dz}\left[\frac{1}{m_0^*(z)}\frac{d}{dz}\right] + V(z)\right\}\phi_n(z) = E_n\phi_n(z) \tag{2.21}$$

with the boundary conditions

$$\phi_n^A(z_0) = \phi_n^B(z_0) \tag{2.22}$$

$$\frac{1}{m_{0,A}^*}\frac{d\phi_n^A(z_0)}{dz} = \frac{1}{m_{0,B}^*}\frac{d\phi_n^B(z_0)}{dz} \tag{2.23}$$

A and B indicate the different materials and $z = z_0$ means the interface, where the boundary conditions have to be applied. The electron motion in the (x, y) plane is not confined and thus the energy in a subband n accounts for

$$E_{n,k_\parallel} = E_n + \frac{\hbar^2 k_\parallel^2}{2m_0^*} \tag{2.24}$$

with $k_\parallel$ being the in-plane momentum. For a proper calculation of the energy eigenvalues the non-parabolicity of the energy dispersion has to be considered. This arises from the influence

of the valence band and is treated by introducing the energy band dependent electron effective mass $m^*(E)$:

$$m^*(E) = m_0^* \left(1 + \frac{E}{E_g^*}\right) \tag{2.25}$$

with the effective band gap energy E_g^* [39] and E measured from the conduction band edge. The non-parabolicity coefficient γ is defined as:

$$\gamma^{-1} = \frac{2m_0^* E_g^*}{\hbar^2} \tag{2.26}$$

For InGaAs wells $\gamma = 1.13 * 10^{-14}\, cm^2$ and $E_g^* = 0.79\, eV$ are given [39].
In order to determine the strength of the optical transitions between two involved states, the optical matrix element is introduced. The dipol matrix element z_{if} between states i and f writes

$$z_{if} = \frac{\hbar}{2(E_f - E_i)} \left\langle \Phi_i \left| \frac{1}{m^*(E_{i,z})} p_z + p_z \frac{1}{m^*(E_{j,z})} \right| \Phi_j \right\rangle, \tag{2.27}$$

where $p_z = -i\hbar(\partial/\partial z)$ is the momentum operator. The wavefunctions are normalized according to

$$1 = \left\langle \phi_i \left| 1 + \frac{E - V(z)}{E - V(z) + E_g^*(z)} \right| \phi_i \right\rangle \tag{2.28}$$

2.3.2 Intersubband scattering mechanism

Several relaxation machanisms like acoustic phonon emission, electron-electron scattering, interface scattering, impurity scattering and alloy scattering exist in semiconductor devices. The fastest intersubband scattering process in a QC structure is the longitudinal-optical (LO) phonon assisted scattering. Lifetime values ranging from below 100 femtoseconds to as much as several picoseconds are confirmed by experiments. The fact that in the mid-infrared operating QCLs the lasing energy ist always larger than the LO phonon energy significantly reduces the efficiency of this devices. On the other hand this fast scattering process is used to reach a fast depopulation of the lower laser level by designing a level beneath with an energy seperation of the LO phonon energy or slightly higher in order to increase the population inversion. The LO phonon scattering rate $\gamma = 1/\tau$ is defined as [40], [41]

$$\begin{aligned} \frac{1}{\tau_{if}} &= \frac{m^* e^2 \omega_{LO}}{2\hbar^2 4\pi\varepsilon_0\, q_{if}} \left(\frac{1}{\varepsilon_\infty} - \frac{1}{\varepsilon_{static}}\right) \left(1 + \frac{1}{e^{\frac{\hbar\omega_{LO}}{k_B T}} - 1}\right) \times \\ & 2\pi \int dz \int dz' \phi_i(z)\phi_f(z) e^{-q_{if}(z-z')} \phi_i(z')\phi_f(z') \quad , \end{aligned} \tag{2.29}$$

where q_{if} is the phonon wavevector. Further parameters are ε_0 defined as the dielectric constant of vacuum, ε_∞ is the high frequency and ε_{static} the static dielectric constant , e is the

electronic charge, c is the velocity of light and k_B the Boltzmann constant. For $In_{0.53}Ga_{0.47}As$ the (GaAs-like) LO phonon energy $\hbar\omega_{LO} = 34\,meV$ [42], [43], $\varepsilon_\infty = 11.6$ and $\varepsilon_{static} = 13.9$ are used [29]. For $In_{0.52}Al_{0.48}As$ the AlAs-like phonon energy is given by $\hbar\omega_{LO} = 46\,meV$ [44], [45]. In QCLs the intersubband lifetime is determined by the emission of LO phonons. In this case the absolute value of the phonon wavevector can be written as

$$q_{if} = \sqrt{\frac{2m^*}{\hbar}(\omega_0 - \omega_{LO})} \tag{2.30}$$

where the in-plane momentum of the electrons in the initial state is assumed as $k_{i\parallel} = 0$. The transition angular frequency ω_0 is given by $(E_i - E_f)/\hbar$. E_i, E_f are the initial and final subband energies, respectively. In general the influence of the acoustic phonons can be neglected since the lifetime is about $100\,ps$, except at energy differences lower than LO phonon energy ($\Delta E < \hbar\omega_{LO}$) and at low temperatures [46]. In this case optical phonon scattering is forbidden.

2.3.3 Carrier transport

The carrier transport path is enabled when an appropriate electric field is applied, where the injector ground state g gets degenerated with the upper laser level 3 of the active cell and tunneling through the barrier takes place. Then the electron relaxes into the lower laser level by emitting a photon. The depletion of level 2 is caused by resonant LO phonon scattering and the electron travels through the injector into the upper laser level of the next cascade. The tunneling time at resonance, by assuming a QCL designed to operate in the strong coupling regime, can be calculated as [47], [48]

$$\tau_{tunnel} \approx \frac{h}{2\,\Delta E}, \tag{2.31}$$

where ΔE is the energy splitting between energy levels g and 3 at resonance. Here, a quasi-equilibrium is reached between the injector and the upper laser level, providing typical tunneling times in the sub-picosecond regime. Similarly, the exit barrier is designed to extract electrons out of the active cell into the adjecent injector. However, the current density is determined by the lifetime of the upper laser level τ_3 and the carrier sheet density N_s in the injector ground state

$$J \approx \frac{eN_s}{2\tau_3}, \tag{2.32}$$

These equations only describe the situation under fully resonant conditions, whereas sufficient tunneling current can flow over a certain range of applied electric fields. The current has to be large enough that the gain compensate the loss, which is the reason for observing laser action for a wide range of electric fields in QCLs with a large gain coefficient and a low-loss waveguide.

2.3.4 Population dynamics and threshold current density

So far, the ideal carrier transport has been described. The real path is bypassed by other scattering channels, which in general increase the threshold current by additional current paths. Figure 2.11 shows the different transition possibilities, where the parasitic paths are indicated by dashed lines. The scattering from the injector ground state g directly into the bottom states 2 and 1 can be treated as a parallel current to the actual laser current. This bypassing is described by the injection efficiency η into the upper laser state 3. Further the scattering directly from the level 3 into lower states of the injector results in a reduced upper laser level lifetime τ_3. Finally, when the level 3 is close to the barrier edge, the electrons may escape into the continuum via tunneling or thermal excitation at higher temperatures. Once in the continuum, electrons are freely accelerated by the electric field and are not expected to participate in the laser action any longer. This mechanism also leads to a reduced upper laser level lifetime, and therefore, directly reduces the gain coefficient. This results in a lifetime τ_{esc}. The lifetime of level 3 is calculated as follows

$$\frac{1}{\tau_3} = \frac{1}{\tau_{32}} + \frac{1}{\tau_{31}} + \frac{1}{\tau_{esc}} \tag{2.33}$$

where τ_{32} and τ_{31} are the intersubband scattering times due to LO phonon transition between states 3-2 and 3-1, respectively.

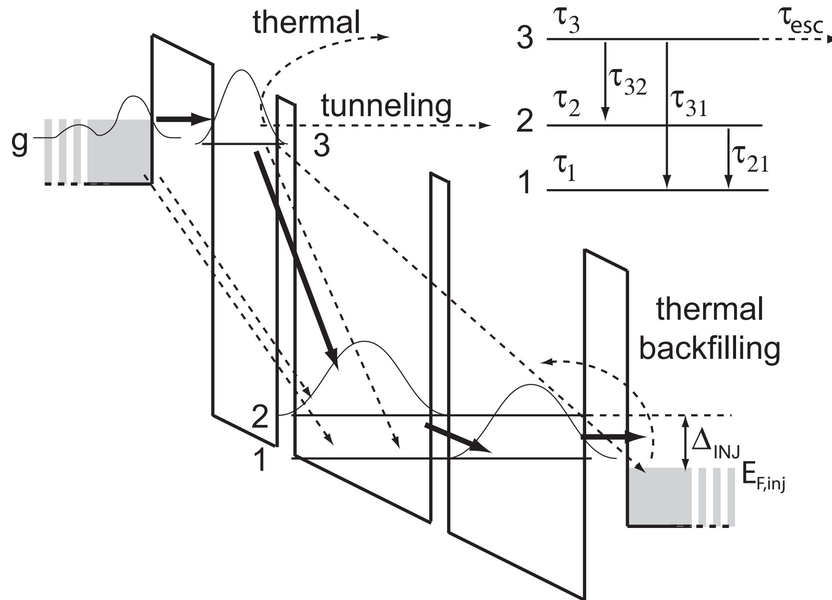

Figure 2.11: Conduction band structure of a three-well QCL design. The dashed arrows indicate the various electron scattering machanisms beyond those participating in laser action. Inset shows the relevant transitions in a QCL as well as the energy level lifetimes and scattering times.

As mentioned before the injector is doped in order to provide an electron reservoir, where the doping density determines the Fermi energy level $E_{F,inj}$ in the injector. At elevated temperatures this can increase the probability of thermal filling of the lower laser level with injector electrons. This decreases the population inversion. However, this effect depends on the temperature and the energy seperation Δ_{INJ} between the injector Fermi level and level 2 of the preceding lasing cell, which can be influenced by a proper active region design. The rate equations for the three level laser system read

$$\frac{dn_3}{dt} = \eta\frac{I}{e} + \sigma N n_2 - n_3\tau_3^{-1} - \sigma N n_3 \quad (2.34)$$

$$\frac{dn_2}{dt} = (1-\eta)\frac{I}{e} + n_3\tau_{32}^{-1} + n_{therm}\tau_2^{-1} + \sigma N n_3 - \sigma N n_2 - n_2\tau_2^{-1} \quad (2.35)$$

$$\frac{dN}{dt} = (N\sigma n_3 - N\sigma n_2 - \alpha N)c/n_{eff} \quad (2.36)$$

where ηI is the injected current, N is the lasing-mode photon density per unit length in one active region, n_{therm} is the electron sheet density of the injector electrons having appropriate energy due to thermal excitation, α are the optical losses in the resonator made up of the mirror losses α_m and waveguide losses α_w, $\alpha = \alpha_m + \alpha_w$ (see section 3.2). Light speed is termed by c and n_{eff} is the effective refractive index of the guided mode. The transition cross section σ is given by

$$\sigma = \frac{4\pi e^2 z_{if}^2}{\varepsilon_0 n_{eff}\lambda 2\gamma_{if} L_p}, \quad (2.37)$$

The term $2\gamma_{if}$ describes the broadening of the transition which is the full width at half maximum (FWHM) of the electroluminescence spectrum [49]. λ is the wavelength in vacuum, z_{if} is the optical matrix element and L_p is the length of one period (injector and lasing region) of the active region.

Evaluating the equations 2.34-2.36 for steady state conditions (i.e. $\frac{dn_3}{dt} = \frac{dn_2}{dt} = \frac{dN}{dt} = 0$) and neglecting the thermal backfilling effect yields an expression for the gain per unit length G (unit: m^{-1}) that reads as

$$G = \sigma(n_3 - n_2) = \frac{4\pi e\, z_{32}^2}{\varepsilon_0 n_{eff}\lambda 2\gamma_{if} L_p} J \left[\eta\tau_3(1 - \frac{\tau_2}{\tau_{32}}) - (1-\eta)\tau_2\right] \quad (2.38)$$

with the occupation densities n_3 and n_2 of laser levels 3 and 2, respectively. The current density is termed as J and τ_2 ist the total lifetime of the lower laser level 2. The gain can also be expressed as $g = G/J$ and is called $gain\, coefficient$ (unit: m/A). The influence of the thermal backfilling can be taken into account by expressing the threshold current density

$$J_{th} = \frac{\alpha}{\Gamma g} + e\left[\eta\tau_3\left(1 - \frac{\tau_2}{\tau_{32}}\right) - (1-\eta)\tau_2\right]^{-1} n_{therm} \quad (2.39)$$

Chapter 3

Mid-infrared quantum cascade lasers

The advances in epitaxial layer growth of semiconductor materials allowed the fabrication of semiconductor superlattice structures. By dint of heterostructures formed by semiconductor materials with different band gap energies quantum cascade lasers can be realized. Such devices based on intersubband transition provide several advantages compared to interband transition, like narrower line width with a lower thermal dependence as well as "giant" dipol matrix elements resulting in a proper lasing performance [50]. Such a QCL consists of a lasing (active) region and an injector. A possibility to influence the conduction band discontinuity limited by the incorporated semiconductor compounds is described, leading to the so-called "short-wavelength" lasers emitting at $3\,\mu m - 5\,\mu m$. Besides the active region, the QCLs need a laser resonator for operation, which is a further point of discussion in this chapter.

3.1 QCL design

3.1.1 Active zone

The lasing action in a QCL laser takes place in the active zone of the multilayer structure. There are different designs for the active zone which all have the common lasing principle: electrons provided by a reservoir tunnel through a barrier into the upper laser level. Then these electrons relax into a lower laser level by emitting a photon. In order to achieve population inversion the electrons need to exit from the lowest level into the following downstream injector region at a high rate. However, where the radiative transition takes place and how the inversion is achieved, is characteristic for each design.

Three-well design

One of the simplest embodiment of a QCL consists of two wells, one providing the electronic states 3 and 2 necessary for the radiative transition and the other one for depleting the lower

laser level [51]. The so-called *three-well vertical* transition system is an improved design, where an additional thin well is inserted between the injector region and an active region (Fig. 3.1(a)). This reduces the electron scattering from the injector directly into the laser ground states 2 and 1, thus increasing the injection efficiency [51]. Here, the wavefunctions of the upper and lower laser state which are involved in the laser action, are essentially located in the same region of the real space. This leads to a low applied voltage sensitivity of the wavelength, since the energy seperation of the two states is largely independent of the applied electric field. In schematic conduction band diagrams the latter is visualized by the linear slope of the electronic potential. Furthermore the collocation of the wavefunctions leads to a comparatively large optical dipole matrix element which enhances the gain coefficient. On the other hand the large wavefunction overlap results in comparatively short electron scattering times.

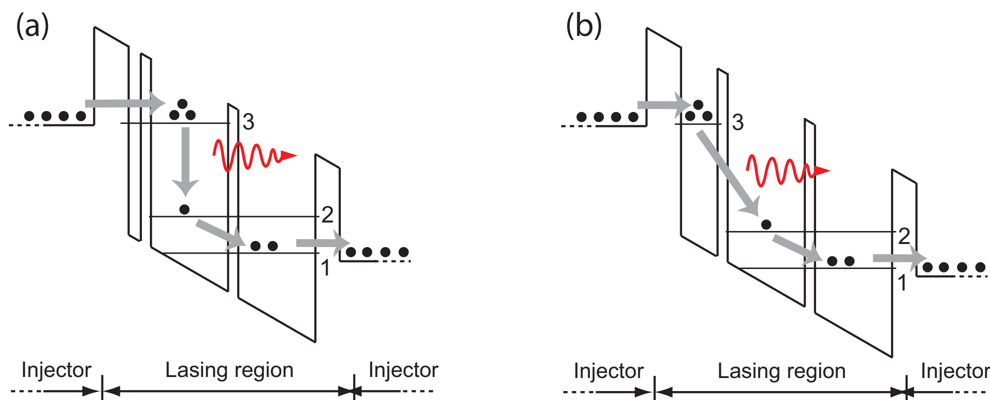

Figure 3.1: Conduction band line-up of a three-well QCL design based on (a) vertical and (b) diagonal transition. The lasing transition is taking place between level 3 and 2 indicated by wavy arrows. In both cases, lower laser level 2 is depleted via fast resonant LO-phonon emission.

The first demonstrated QCL [13] is basically a three-well design based on a *diagonal* transition (Fig 3.1(b)). In this case the upper and lower state wavefunctions are clearly located in spatially different regions which gives rise to longer scattering times but also smaller dipole matrix element and a strong dependence of the wavelength on the applied electric field through a voltage-induced Stark effect.

Superlattice design

The first *superlattice* active region QCL were introduced in 1997 [52]. In general this structure consists of a periodic stack of nanometer-thick layers of quantum wells and barriers where the conduction band is splitted in minibands seperated by minigaps. Here, laser action takes place between miniband edges (Fig.3.2). These lasers excel through their large current carrying capabilities and high gain due to the vertical transition. Also the depletion of the lower

laser state is enhanced, because in minibands electrons relax much faster by small-wavevector optical phonons. On the other hand the lack of resonant tunneling in the upper laser level a manifold of bypass channels appear yielding a reduction of the upper state lifetime.

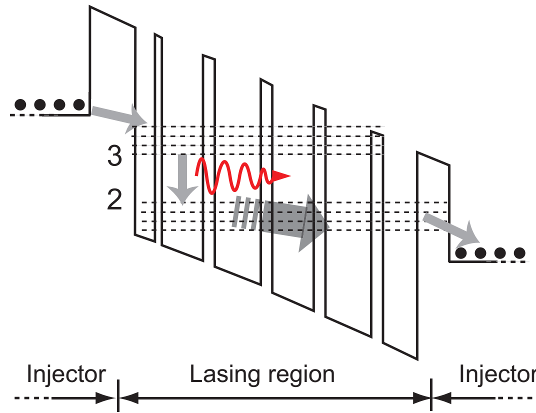

Figure 3.2: Conduction band diagram for a typical superlattice active region. The lasing transition (wavy arrow) is taking place between the lowest state of the upper miniband and the uppermost level of the lower miniband. The manifold of states in the latter leads to a fast depopulation of the lower laser level.

Bound-to-continuum design

A *bound-to-continuum* based QCL first demonstrated by Faist *et al.* [53], combines the benefits of the two already mentioned designs. The lower laser level is the uppermost state in the lower tilted miniband, thus providing a fast depopulation, whereas the upper state is a single level as in the three-well design (Fig.3.3). This fact and the vertical transition give rise to an efficient filling of the upper state and a high oscillator strength. By incorporating a diagonal transition system Pflügl *et al.* demonstrated bound-to-continuum GaAs/AlGaAs QCLs working at temperatures above 100° C in pulsed operation [54].

3.1.2 Injector

As can be seen in the schematic descriptions mentioned in the previous section, a lasing region is surrounded by the so-called injector structures. The injector has to transport the electrons from one lasing region to the next. It also depletes the lower lasing level of the previous lasing region and provide electron injection into the downstream upper lasing level. However, it should be mentioned that by using a double-QW superlattice active region it is possible to incorporate the essential features of the injector into the active region itself [51]. This allows a realization of QCLs without the firm requirement of injector regions.

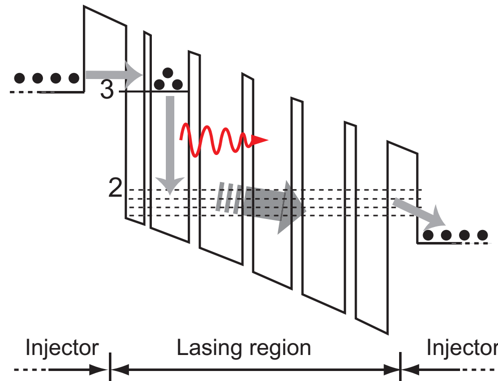

Figure 3.3: Conduction band line-up of a bound-to-continuum design. The transition taking place between the localized state at level 3 and the upper state 2 of the supperlattice continuum contributes to photon emission. This design provides a high dipole matrix element due to the vertical lasing transition as well as a fast superlattice depletion of the lower laser state.

Superlattice

The coupling of several quantum wells depends on the barrier thickness seperating them. The narrower the barrier the stronger the coupling, due to the interaction of exponentialy decaying tails of the quantum well bound-state wave functions (Fig. 2.10(b)). By reducing the barrier width a strong coupling can be reached in order to form minibands, and the term ”superlattice” (SL) can be assigned to these artificial periodic structures, where the lattice constant is one order of magnitude larger compared to the solid state crystal. These minibands are separated from each other by minigaps, both having energies in the $10\,meV$ region. The effect of the mentioned strong coupling with applied electric field is illustrated in figure 3.4. Due to the biasing the minibands get tilted and the electron wavefunctions are localized over a distance $\lambda = \frac{\Delta}{eF}$ for a given electric field F. Δ describes the miniband width and e is the electric charge. This is the so-called Wannier-Stark-effect [55], [56].
As mentioned in the previous section superlattices can be used either for the lasing zone as well as to provide electron transport. By applying a sufficient electric field the miniband and the energy ground levels 2 and 1 can be brought in resonance, which leads to a fast depletion of the latter. Furthermore the minigap acts as a forbidden zone where any motion of electrons is not allowed. This ”Bragg-reflector” suppresses tunneling out of the level 3 into the continuum what increases the inversion population between the upper and lower laser level. An alternative SL-QC laser design to achieve flat minibands is found in the so-called $chirped$ superlattice QC lasers [51]. Here, the period of the SL is varying, from wide to narrow quantum wells in the direction of the electron motion. At zero bias, the states of the wells are localized because the variation in the thickness of the adjacent layers is such that the corresponding energy levels are out of resonance. If an external field with an appropriate value is applied, these states are brought in resonance, forming minibands and minigaps.

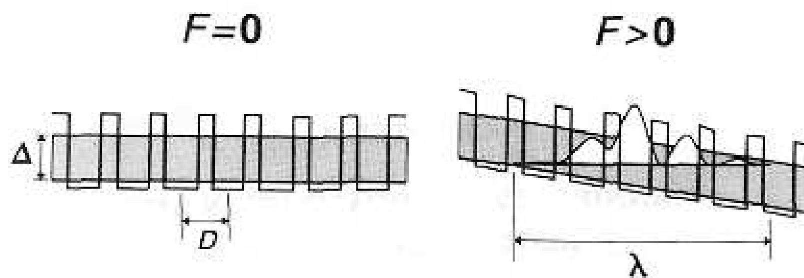

Figure 3.4: A superlattice with a miniband is illustrated without (left) and with (right) external electric field. In biased condition the localization length λ of the Wannier-Stark states is determined by the miniband width Δ and the electric field F [57].

Doping of the injector

In order to provide an electron transport within the QCL structure several injector epilayers are n-doped, hence serving as an electron reservoir. The lasing region itself is not doped to prevent emission line broadening due to impurity scattering [58]. It is known from experiments and theory that the superlattices break into different electric field domains within which the energy levels are locked in resonance. In a laser structure, a homogenous and stable electric field distribution is an absolute necessity. Therefore, the injector has to be doped so that the negative charge is exactly compensated by the fixed positive donors. Additionaly the operating point must be a stable point of the current-voltage characteristics to prevent the breakdown of the active region into different field domains. On the other hand increasing the doping density leads to a higher Fermi energy of the injector, increasing the possibility of a thermal backfilling of the lower laser level of the preceding active zone. This yields a reduced inversion population. Thus a doping level should be chosen that the energy distance Δ_{INJ} of the mentioned states should be substantially larger than the thermal energy k_BT. Futhermore, free-carrier losses must be minimized.
The objective of this thesis is to study the effect of injector doping variation and to determine the optimal doping density in order to improve the performance of QCLs.

3.1.3 Strain-compensated structures

The performance of QCLs tending to high energy emission is limited by the conduction band dicontinuity of the employed material composition. The shorter the desired wavelength the higher the energy distance between the upper and lower laser states. In this case the upper state is shifted toward the conduction band edge of the used semiconductor providing the barrier, which reduces the effective barrier height. When the barrier is lowered two loss mechanisms

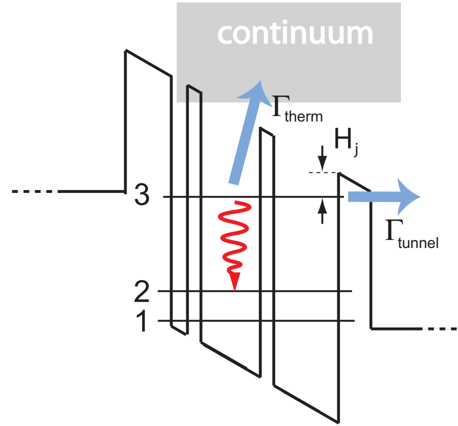

Figure 3.5: The loss mechanisms due to the thermal emission into the continuum (gray shaded) as well as tunneling out of the active region are shown. Both are reducing the lifetime of electrons in the upper laser level.

appear affecting the electrons in the energy level 3. On the one hand the thermal emission into the quasi-continuum, on the other hand the tunneling through barriers out of the active zone are leading to a decreased inversion (Fig. 3.5). This can be considered by the loss rates [59], [60]:

$$\Gamma_{therm,j} \propto exp\left(-\frac{H_j}{k_B T}\right) \quad (3.1)$$

$$\Gamma_{tunnel,j} \propto exp\left(-\frac{2L_B}{\hbar}\sqrt{2m^*_{e,B}H_j}\right) \quad (3.2)$$

This equations describe the effect of electron escaping from a quantum well state j by thermal emission into the continuum and tunneling out of the active cell. The term H_j is the effective barrier energy, T is the temperature, L_B is the width of the exit barrier and $m^*_{e,B}$ the electron mass in the barrier material. Due to the exponential dependence on H_j the upper laser level is most affected. This reduces the population inversion between states 3 and 2 at elevated emission energy, giving a rise to stop lasing.

In order to circumvent this discrepance the conduction band discontinuity has to be enlarged [61]. In $In_xGa_{1-x}As/In_yAl_{1-y}As$ structures grown lattice matched on InP the value $\Delta E_C = 520\,meV$ is given. A possibility to influence the conduction band offset has been discussed in chapter 2.2 by introducing the strain effect in semiconductor heterostructures. Following this theory ΔE_C can be extended by incorporating quantum wells with a band gap energy lower than $In_{0.53}Ga_{0.47}As$ and barrier materials which offer a higher band gap energy compared to $In_{0.52}Al_{0.48}As$. This can be fulfilled by using compressive strained quantum wells with an indium content $x > 0.53$ and tensile strained barriers with $y < 0.52$. One should remember that strain causes some limitation in case of the epitaxial growth. Following the theory of

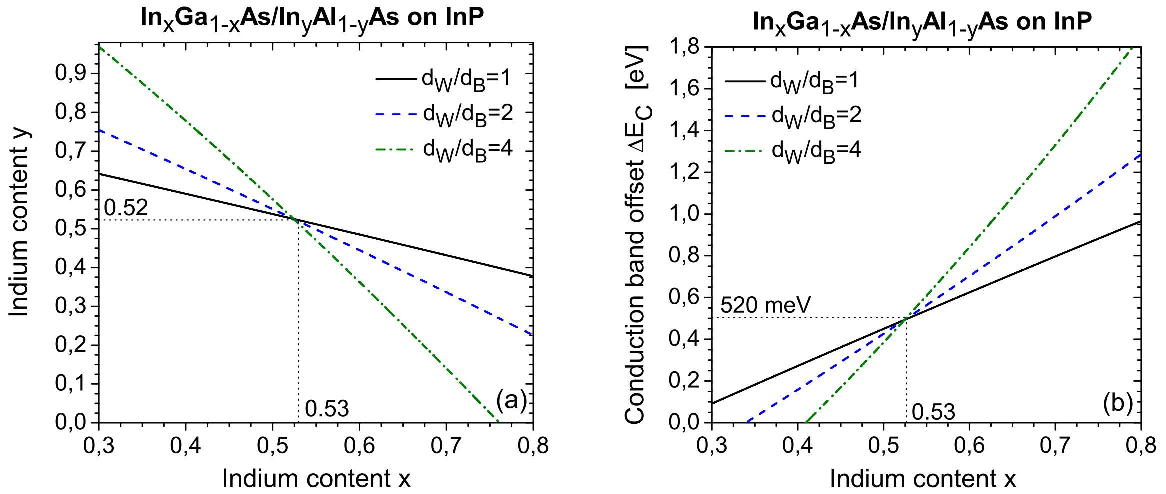

Figure 3.6: (a) Calculated indium fraction y as a function of fraction x for different barrier/well total thickness ratios. This calculation satisfies the strain compensation condition (Eq. 3.3). (b) The conduction band discontinuity ΔE_C as a function of x according to Van de Walle's model-solid theory.

Matthews and Blakeslee the layer thickness should not exceed the critical thickness d_c, in order to provide a pseudomorphic growth. If a usual epilayer thickness of 5 nm used in the active cell and the injector is assumed the condition for $d_c > 5\,nm$ reads $0.53 < x < 0.76$ and $0.29 < y < 0.52$ (Fig. 2.5). In this way ΔE_C can be tailored in a certain region. However, the net heterostructure strain caused by the several strained QWs and barriers can result in relaxations if the thickness is to large. Thus the total compressive strain of the QWs has to be compensated by the total tensile strain of the barriers over the entire periode of a QCL. This condition for dislocation free structures can be written as

$$\frac{a_{QW,\perp} - a_0}{a_0} d_{QW} + \frac{a_{B,\perp} - a_0}{a_0} d_B = 0 \tag{3.3}$$

where $a_{QW,\perp}$ and $a_{B,\perp}$ are the lattice constants of strained QWs and barriers perpendicular to the epilayer surface, respectively. The lattice parameters of InP are termed as a_0 and d_{QW} (d_B) as the total QW (barrier) thickness per cascade. In order to calculate the corresponding indium content values x and y equation 3.3 has to be solved for a given ration d_{QW}/d_B. Figure 3.6(a) shows the calculated relation between x and y for $d_{QW}/d_B = 1$, 2 and 4. All data points along a line plot fulfill the condition of strain compensation. This means that for an assumed content x the increasing comprehensive strain due to higher d_{QW}/d_B ratio has to be counterbalanced by a higher tensile strain caused by a lower indium content y. When the corresponding values are determined the conduction band discontinuity can be calculated. Figure 3.6(b) shows ΔE_C as a function of x according to Van de Walle's model-solid theory (chapter 2.2.2). For $x > 0.53$ and $y < 0.52$ band offset higher than $\Delta E_C = 520\,meV$ for

lattice matched $In_{0.53}Ga_{0.47}As/In_{0.52}Al_0.48As$ can be realized. However, tailoring ΔE_C needs to satisfy the condition 3.3 in order to compensate the strains in each epilayer. Thus this concept has to be carried out self-consistent in contrast to the lattice matched system, requiring more effort. Lasers based on this kind of design are called $strain\text{-}compensated$ QCLs. The enhanced conduction band discontinuity provides a larger freedom in design. First of all the effective barrier height H_j can be increased compared to a lattice matched structure, what decreases the loss rate of thermal emission into the continuum and tunneling out of the active cell, as discussed before. A further advantage is the possibility of faster depopulation of the lower laser level by an additional ground state. Due to the large offset it is possible to shift all states up energetically and insert an additional well. Here, the radiative transition takes place between states 4 and 3 (Fig. 3.7). The individual layer thicknesses are chosen to seperate the levels 3-2 as well as 2-1 by $\hbar\omega_{LO}$ in order to deplete the lower laser level by emission of LO-phonons. Beside the improved population inversion due to the $"double\text{-}phonon\, resonance"$ [62], [63] such a "four-well" design also increases the energy distance Δ_{INJ} between the Fermi energy of the injector and level 3. This gives a rise to an improved QCL performance at elevated temperatures.

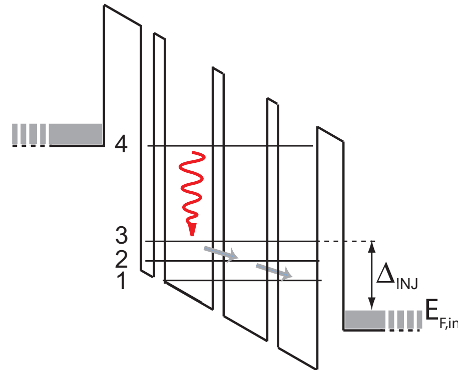

Figure 3.7: Conduction band line-up of a four-level design. Here the population inversion is improved by a double-phonon emission (transitions 3-2 and 2-1).

The QCLs characterized within this thesis benefit from another property of the enhanced band offset, namely the ability to emit at higher energies. This herein described $short\, wavelength$ QCLs emit at $3.8\,\mu m$, where the active region consists of AlAs barriers and $In_{0.74}Ga_{0.26}As$ QWs, yielding $\Delta E_C = 1.33\,meV$. An important issue which one needs to consider are indirect valleys in all the used materials: $In_{0.74}Ga_{0.26}As$, AlAs, and $In_{0.55}Al_{0.45}As$. Intersubband absorption in the Γ-valley can be observed even if the excited state is above an indirect valley minima. But a laser active region design has necessary to be done in a way, that an upper lasing state is below all indirect valley minima [64]. Otherwise inter-valley scattering will reduce population inversion between the lasing states, and thus prevent the lasing conditions. In this design two different barrier materials ($In_{0.55}Al_{0.45}As$ plus AlAs), used in the active re-

gion, made it possible to tune the barrier thicknesses and the net strain almost independently. This solution, makes the band engineering in the present $In_{0.74}Ga_{0.26}As$ material system as easy as in the case of the lattice matched $In_{0.53}Ga_{0.47}As/In_{0.52}Al_{0.48}As$ combination.
In general incorporating the strain-compensated $In_xGa_{1-x}As/In_yAl_{1-y}As/InP$ material system leads to a rigorous enhancement of the QCL performance. This fact resulted in the demonstration of short-wavelength QCLs [65], [66], [25] , high-temperature continous wave operation QCLs [67] and devices emitting at the shortest wavelength of $3.05\,\mu m$ [26], presented so far for this material system.

3.1.4 Cascading effect

As discussed in section 3.1.1 the electron transition in a lasing cell results in the emission of one photon, thus cascading of N_P active cells yields a multi-photon generation. Several studies of the dependence of the device performance on the number of stages in mid-infrared QCLs have been performed, ranging from $N_P = 1$ to 100 [51]. While laser action from a QCL with only one stage ($N_P = 1$) [51] is remarkable as it underlined the high optical gain that can be achieved by band gap engineering, the QCL with $N_P = 100$ stages highlights the cascading scheme, that allows stacking a very large number of active regions into a single cascade. In order to design high power and low threshold current devices the number of cascades has to be increased. On the other hand this elevates the voltage drop across the entire N_P stage cascade given by

$$V_S(N_P) = \frac{(E_{32} + E_{21})}{e} N_P \propto N_P \tag{3.4}$$

and gives a rise in dissipated power $P(N_P) = V_S(N_P) \cdot I(N_P)$. The energy drop per stage is given by $E_{32} + E_{21} = E_{Photon} + E_{LO-phonon}$. An agreement between low power consumption and high power has been shown for $N_P = 22$ experimentally [51]. The active core of the QCLs analyzed in this thesis consists of 30 injector/lasing zone periods.

3.2 Laser resonator

Beside the active region where the photon generation takes place the light has to be confined in order to provide proper lasing performance. This requirement is fulfilled by the laser resonator. By keeping the light longer inside the cavity more power is gained and the threshold current is decreased, both leading to an enhanced QCL performance.
The devices discussed in this work are based on the $Fabry$-$Perot$ type laser cavity usually providing a multi-mode emission spectrum. For desirable single mode emission, within the gain spectrum of the active material, several approaches were taken like microcavities [68], [69], coupled cavity [70] and external cavity lasers [71]. Another possibility to achieve single mode operation can be achieved by incorporating a Bragg grating on the top of the laser ridge.

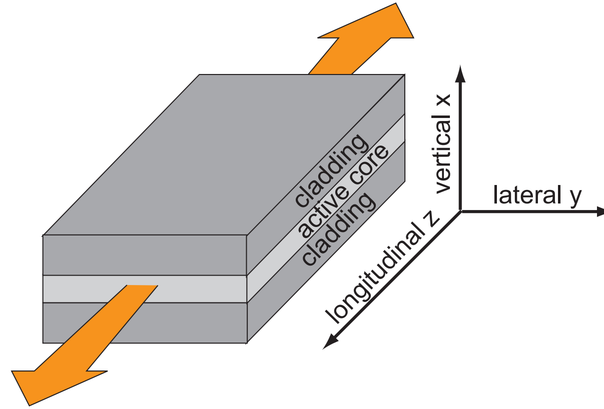

Figure 3.8: Schematic description of a QCL waveguide including the definition of directions.

In these distributed feedback (DFB) lasers the single line emission is obtained by proper grating design [72], [73]. However, these QCLs are based on the edge emitting principle. The light generated in QCLs is due to intersubband selection rules transverse magnetic (TM) polarized (electric field is parallel to growth direction) [74], which is a drawback in case of surface emission because fabricating vertical cavity surface emission lasers is not feasible. The demonstration of surface emission by using a second-order DFB grating for light diffraction [75], [76], [77] as well as photonic crystal QCLs [78] circumvented this limitation.

3.2.1 Optical constants

For an accurate waveguide design the knowledge of optical properties of the used materials is required. The complex refractive index η can be calculated using the Drude formula [79]:

$$\eta = n + i\kappa = \sqrt{\varepsilon_\infty \left(1 - \frac{\omega_p^2}{\omega^2 \left(1 + \frac{i}{\omega\tau}\right)}\right)} \tag{3.5}$$

where $\omega = 2\pi c/\lambda$ is the angular frequency, ε_∞ is the high frequency dielectric constant. The plasma frequency is given by

$$\omega_p = \sqrt{\frac{N_d e^2}{\varepsilon_0 \varepsilon_\infty m_0^*}} \tag{3.6}$$

depending on the free carrier concentration N_d. The scattering time τ is calculated from the electron mobility μ by $\tau = \mu m_0^*/e$. The dependence of the mobility on the doping concentration is approximated using the Hilsum formula [80]

$$\mu = \frac{\mu_0}{1 + \sqrt{N_d/N_0}} \tag{3.7}$$

material	N_d(cm^{-3})	n	κ
InP	1e17	3.08	5e-5
InP	2e17	3.08	1e-4
InP	4e18	2.98	2e-3
InGaAs	5e16	3.42	4e-5
InGaAs/InAlAs/AlAs active region	0.7e17	3.25	4e-5
	1.1e17	3.25	6e-5
	1.7e17	3.25	9e-5
	3.9e17	3.24	2e-4
gold	-	1.12	28
SiN	-	2	4e-3

Table 3.1: Refractive indices at 3.8 μm for different materials used for the wavegiude calculation. For the active region the refractive index was calculated considering the different active region doping of the QCL processed within this thesis. N_d is the donor concentration, n and κ are the real and imaginary parts of the complex refractive index, respectively.

The coefficients μ_0 and N_0 as well as other values necessary to calculate the refractive indices and absorption coefficients for AlAs, InP and lattice matched InGaAs and InAlAs are taken from [81]. The refractive index of gold (Au) was taken from [82] and the value for SiN can be found in [83]. To provide current transport the waveguide layers have to be doped. In calculations of the refractive index this fact is considered by introducing the doping dependent mobility. Free carrier absorption in these layers, and at high doping levels the strongly noticeable onset of the plasma edge, usually reduce the refractive index compared to the purely dielectric value. The intensity absorption coefficient is given by

$$\alpha = 4\pi\kappa/\lambda. \tag{3.8}$$

3.2.2 Vertical confinement

As mentioned before in a QCL waveguide a transverse optical confinement in both lateral and vertical direction must be ensured in order to provide a sufficient overlap between the optical field and the active zone. Vertical light confinement is achieved by exploiting variable refractive indices of the incorporating semiconductor layers. The material system is chosen to provide appropriate and sufficiently large refractive index variations to build a high refractive index waveguide core containing the active material and lower refractive index cladding layers.

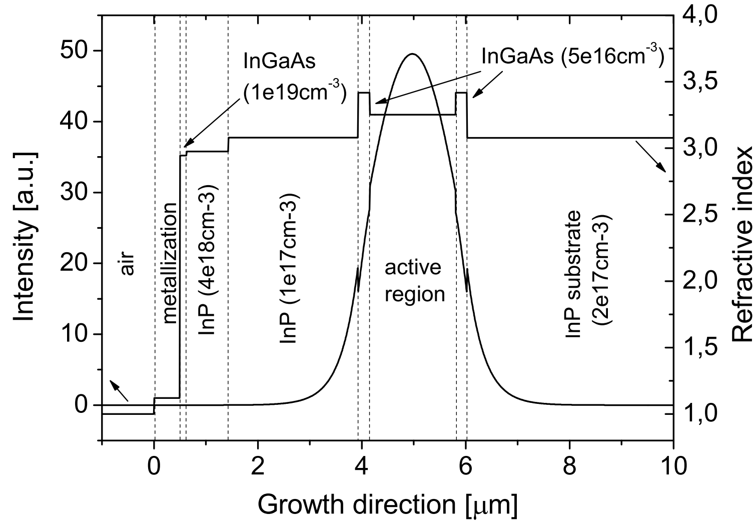

Figure 3.9: Refractive index and calculated mode profile for sample HUB1664 emitting at 3.8 μm. The numbers in the brackets give the donor concentration of the layers.

The active region of the QCLs investigated in this work is based on InGaAs/InAlAs/AlAs material system grown on InP substrate. The cladding layers are provided by utilizing InP, which offers naturally lower refractive index than the active region due to the InGaAs fraction in the latter. By sandwiching the active region between two comparably thin InGaAs layers the refractive index contrast can be increased, especially when the lasing cascade is chosen rather thin. Figure 3.9 shows the calculated mode profile for a dielectric InP-based waveguide structure. The doping of the semiconductor layers on the one hand provides a carrier transport but also a possibility to tailor the refractive index. An increased doping concentration results in a decreased real part of the refractive index as well as elevated imaginary part. The latter leads to higher waveguide losses α_w (Eq. 3.8). Designing a waveguide needs to optimize two characteristic parameters, on the one hand the waveguide losses α_w but also the confinement factor Γ to obtain a low laser threshold. Γ is defined as the overlap of the guided mode with the active region

$$\Gamma = \frac{\int_{act} |E|^2 dz}{\int_{-\infty}^{\infty} |E|^2 dz} \tag{3.9}$$

with E as the transverse electromagnetic field distribution in the slab waveguide. In the GaAs materal system the GaAs/AlGaAs structures are grown on a GaAs substrate, where GaAs provides the highest refractive index. To make this material suitable as cladding layers it must be highly doped. This so-called double plasmon waveguides [84] result in elevated free carrier losses. Thus the InP material system is the better choice in the case of waveguiding due to the lower waveguide losses and the possibility of incorporating the substrate into the cladding layer.

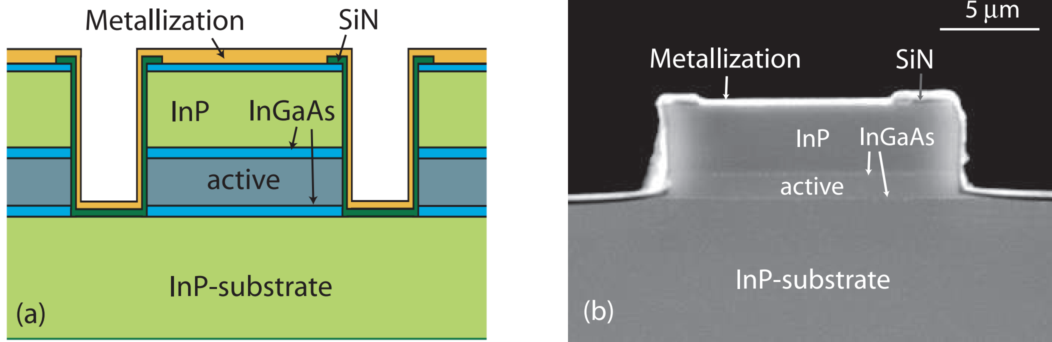

Figure 3.10: (a) Schematic view of a cross section of a deep etched QCL ridge. (b) Scanning electron microscope (SEM) image of a facet of a 14 μm wide ridge.

3.2.3 Lateral confinement

Within this thesis the QCLs are etched into narrow $(10$ to $20\,\mu m)$ ridges providing efficient current and lateral light confinement. The side walls are passivated by silicon nitride (SiN) with a comparable low refractive index (η = 2+i0.0001 at 3.8 μm) providing a high refractive index contrast between active region and insulation, necessary for waveguiding. SiN layer is then overlayed with contact metallization, which inherently increases the waveguide loss due to the interaction of the mode with the metal layers (Figure 3.10). The mode calculations were performed by assuming transverse electric (TE) (electric field parallel to the single layers) and TM polarized light for lateral (see figure 3.11) and vertical confinement, respectively.

3.2.4 Fabry-Perot cavity

The most straightforward way to obtain light confinement in the longitudinal direction is given by cleaving the laser bars perpendicular to the laser ridges. The cleaved facets then act as mirrors, which have to be partially transmitting in order to couple out light. The reflectivity R of a facet in case of normal incident plane waves can be calculated by means of refractive index difference of the used materials according to

$$R = \left(\frac{n_{eff} - n_{air}}{n_{eff} + n_{air}}\right)^2 \tag{3.10}$$

For an interface formed by a InGaAs/InAlAs heterostructure with $n_{eff} \approx 3.2$ and air $(n_{air} = 1)$ the reflectivity is calculated to $R \approx 0.27$. For every guided vertical and lateral mode standing waves are present, the so-called longitudinal modes, that fulfill the condition

$$m\frac{\lambda}{2} = n_{eff}L \tag{3.11}$$

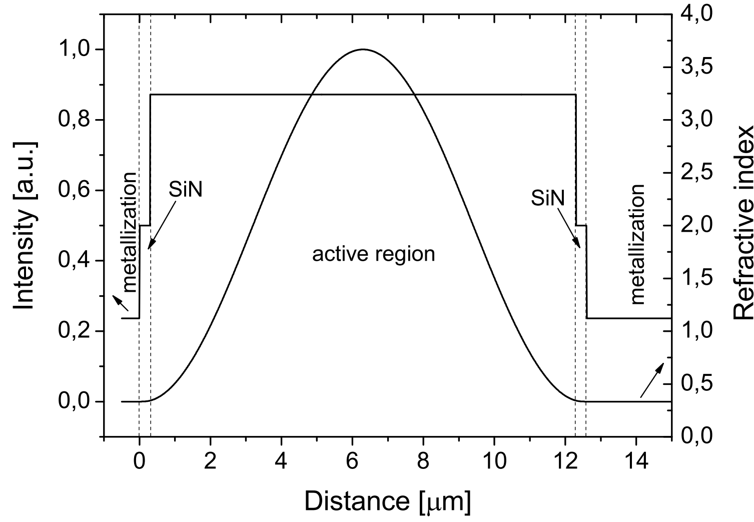

Figure 3.11: Refractive index and calculated mode profile for the zero lateral mode. The calculation was performed for a 12 μm wide ridge of the sample HUB1664 covered by SiN-insulation (300 nm) and an Au-metallization layer (500 nm).

with L as the length of the resonator and an integer $m > 0$. λ is the emission wavelength. In general the refractive index n_{eff} of the active region shows a resonant absorption curve near the respective wavelength λ due to the Lorentzian shaped laser gain. This effect can be considered by the refractive group index n_{group}

$$n_{group} = n_{eff} + \nu \frac{dn_{eff}}{d\nu} \tag{3.12}$$

where ν is the longitudinal mode wavenumber. The $free\text{-}spectral\text{-}range$ (FSR) defined as the spectral mode spacing is given by

$$\Delta\nu = \frac{1}{2n_{group}L} \tag{3.13}$$

The spectral gain width of a typical QCL is of the order of 80 cm^{-1} and thus much broader than the FSR ($\nu \approx 0.8$ cm^{-1} for a 2 mm long cavity). Thus a Fabry-Perot laser features a broad emission spectrum, containing multiple longitudinal modes.

Considering a propagating longitudinal mode along the cavity, the intensity I_0 of the latter at a certain point inside the cavity gets amplified as well as attenuated over the full length L resulting in a intensity I. This in fact is attributed to the gain G per unit length and the waveguide losses α_w per unit length, respectively. This gives the relation:

$$I = I_0 \cdot R_1 R_2 e^{(\Gamma G - \alpha_w)2L} \tag{3.14}$$

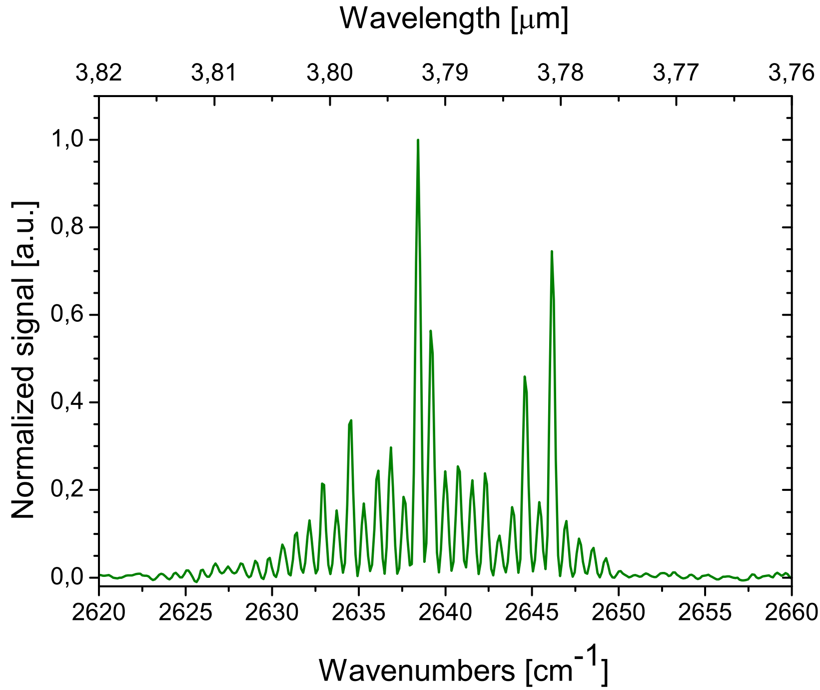

Figure 3.12: A typical multimode Fabry-Perot emission spectrum, obtained from a 1.97 mm long and 14 μm wide laser at 78 K (HUB1660). The laser was operated at a drive current of 0.86 A (1.1 I_{th}).

with Γ as the confinement factor. Beside the waveguide losses also the reflectivities R_1 and R_2 result in a mirror- or outcoupling loss of

$$\alpha_m = -\frac{\ln(R_1 R_2)}{2L} \tag{3.15}$$

When the loss mechanisms are completely compensated by the gain after a roundtrip propagation, the lasing threshold with equation 3.14 reads

$$R_1 R_2 e^{(\Gamma G - \alpha_w)2L} = 1 \tag{3.16}$$

The corresponding threshold current density J_{th} (Eq. 2.39 neglecting thermal backfilling) can be calculated as

$$J_{th} = \frac{\alpha_w + \alpha_m}{\Gamma g} \tag{3.17}$$

The term g is the gain coefficient which is expressed as $g = G/J$ including the laser current density J and the gain G per unit length. It can be assumed that the waveguide loss, mirror loss and confinement factor remain unchanged with temperature. However, the gain coefficient is clearly temperature dependent. Competing with the radiative transition, electron scattering times for LO phonon emission are reduced due to the larger phonon population at higher temperatures. Furthermore the broadening of the gain spectrum and the thermally backfilling

of the bottom laser level by the injector result in a reduced population inversion. All mentioned mechanisms contribute to an increased threshold current density at elevated temperature. For QCLs a typical description of the temperature dependence of the laser threshold can be given by an exponential fit

$$J_{th}(T) = J_0\, e^{T/T_0} \tag{3.18}$$

where T_0 is the so-called characteristic temperature, which ranges for different QCLs from 100 to 200 K. A high T_0 states a weak temperature dependance of the threshold current, thus providing better QCL performance. For fitting the threshold current versus temperature over the entire temperature range of laser operation (i.e. from 4.2 K to above room temperature (RT)) a modified version of equation 3.18 is used

$$J_{th}(T) = J_0\, e^{T/T_0} + J_1 \tag{3.19}$$

with an temperature independent portion of threshold current.
The knowledge of the loss mechanisms also allows to estimate the slope efficiency (i.e. the increase in optical power of a outcoupling facet per unit current) as

$$\frac{\partial P}{\partial I} = \frac{1}{2}\frac{h\nu}{e} N_p \frac{a_m}{a_m + a_w}\left(1 - \frac{\tau_2}{\tau_{32}}\right) \tag{3.20}$$

where $h\nu$ is the photon energy, N_p the number of periods (injector and lasing region). Further τ_2 and τ_{32} are the lifetimes of the lower laser level and the intersubband relaxation time between states 3 and 2 (see chapter 2.3.4), respectively.

Chapter 4

Fabrication and Characterization of QCLs

So far, semiconductor basics as well as designing of QCLs have been discussed. Properties of the InGaAs/InAlAs semiconductor compounds and physical effects in such heterostructures have been presented. This chapter is addressed to the fabrication of QCLs with an introduction into the applied technologies. The second part of this chapter is dedicated to the experimental techniques used for the electrical and optical characterization of QCLs. Finally the results are presented and discussed.

4.1 Technology

All the structures discussed in this thesis were grown by gas source MBE (GSMBE) [85] at the Department of Physics, Humboldt University Berlin. The processing of QCLs involved etching of the ridge waveguide structures by means of reactive ion etching (RIE) was carried out on an Oxford Systems PlasmaLab 100. Passivation layers were deposited via plasma enhanced chemical vapor deposition (PECVD) in the Oxford Systems PlasmaLab 80. Metallization was provided by an electron beam evaporator in a Leybold LH560 evaporation system as well as sputtering by an Ardenne LS320 radio frequency (RF) magnetron sputtering system.

4.1.1 Molecular Beam Epitaxy

The introduction of molecular beam epitaxy (MBE) [5] was a tremendous milestone towards the fabrication of ultrathin controlled semiconductor heterostructures, providing atomic layer crystal growth combined with control of the layer chemical composition. The GSMBE is a modified version of the conventional MBE but is based on the same epitaxial principle. Here, thin films are evaporated monolayer by monolayer on a single crystalline substrate that is kept at elevated temperatures. A special feature of GSMBE is that the group V elements (As, P) are produced by thermal cracking of gases, usually hydride arsine (AsH_3) and phosphine (PH_3),

whereas the group III solid sources (Al, Ga, In, Si) are provided by effusion cells (Knudsen cells), common in a solid source MBE. Silicon is used for n-type doping. At proper preset conditions (temperature, pressure) cracking produces group V elements:

$$2AsH_3 \rightarrow As_2 + 3H_2 \quad (4.1)$$

$$2PH_3 \rightarrow P_2 + 3H_2 \quad (4.2)$$

The atomic beams can be switched on and off by dint of mechanical shutters. Each effusion cell filled with elements is equiped with a heater. When heated the material inside the cell sublimates or vaporizes. By means of molecular or atomic beams of the Knudsen or cracking cells, which are directed towards a rotating substrate holder, deposition takes place with a typical growth rate of 1 μm/hour. This ensures the formation of layers with crystalline perfection. By heating the substrate the deposited atoms obtain the kinetic energy for rearranging themselves to the energerically lowest position namely to the corresponding criytalline structure. The rotating of the substrate holder compensates the eccentrity of the effusion and cracking cells. The dopant effusion rates are too low to be measured *in situ*. Therefore the doping level has to be calibrated *ex situ* by capacitance-voltage, profiling and Hall-effect measurements. Growth mode and material quality is controlled *in situ* by reflection high energy electron diffraction (RHEED).

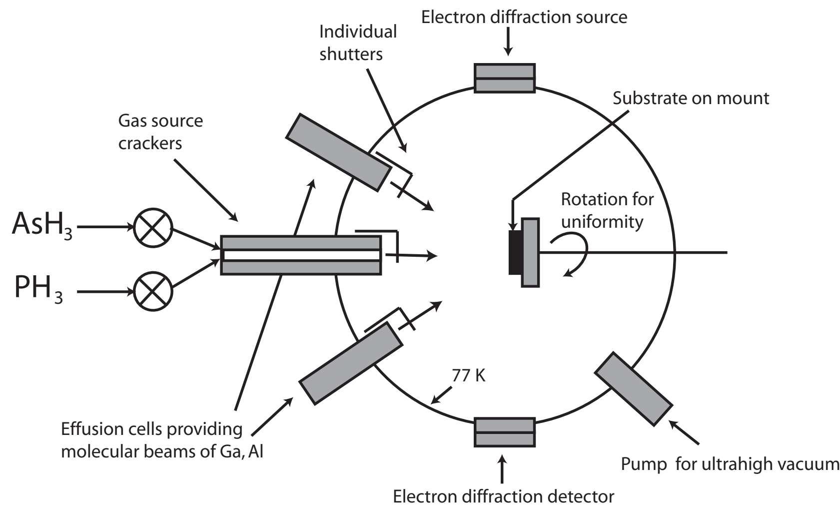

Figure 4.1: Schamatic drawing of a MBE facility.

Optimal MBE growth conditions are achieved by adjusting the III/V flux ratio for each growth temperature. While for the lattice matched InGaAs-InAlAs structures on InP 500-520 °C growth temperature range seems to be optimized and widely used, lower growth temperatures of 400-450 °C, however, appear to be necessary to grow coherently highly strained $In_{0.74}Ga_{0.26}As$-AlAs heterostructures [86].

Layer (Substrate → Surface)		X (%)	Y (%)	Thickness (Å)	Doping
S: n^- InP Substrate				350 µm	2 e17
Si: InGaAs		52		2200	5 e16
Loop 30					
InGaAs		*74*		*39*	
AlAs	***I***			*12*	
InGaAs		*74*		*32*	
AlAs				*10*	
InGaAs	***N***	*74*		*27*	*d*
AlAs				*10*	
InGaAs		*74*		*23*	*d*
InAlAs	***J***		*52*	*8*	*d*
AlAs				*10*	
InGaAs		*74*		*21*	*d*
InAlAs	***E***		*52*	*10*	
AlAs				*10*	
InGaAs		*74*		*20*	
InAlAs	***C***		*52*	*20*	
AlAs				*10*	
InGaAs		*74*		*17*	
InAlAs	***T***		*52*	*19*	
AlAs				*10*	
InGaAs		*74*		*15*	
InAlAs	***O***		*52*	*19*	
AlAs				*10*	
InGaAs		*74*		*13*	
InAlAs	***R***		*52*	*24*	
AlAs				*10*	
InGaAs	*A*	*74*		*16*	
AlAs	*C*			*10*	
InGaAs	*T*	*74*		*45*	
AlAs	*I*			*14*	
InGaAs	*V*	*74*		*41*	
AlAs	*E*			*13*	
Endloop					
InGaAs		*74*		*39*	
AlAs	***I***			*12*	
InGaAs		*74*		*32*	
AlAs				*10*	
InGaAs	***N***	*74*		*27*	d
AlAs				*10*	
InGaAs		*74*		*23*	d
InAlAs	***J***		*52*	*8*	d
AlAs				*10*	
InGaAs		*74*		*21*	d
InAlAs	***E***		*52*	*10*	
AlAs				*10*	
InGaAs		*74*		*20*	
InAlAs	***C***		*52*	*20*	
AlAs				*10*	
InGaAs		*74*		*17*	
InAlAs	***T***		*52*	*19*	
AlAs				*10*	
InGaAs		*74*		*15*	
InAlAs	***O***		*52*	*19*	
AlAs				*10*	
InGaAs		*74*		*13*	
InAlAs	***R***		*52*	*24*	
AlAs				*10*	
Si: InGaAs		52		2200	5 e16
Si: InP				25000	1 e17
Si: InP				8000	4 e18
Si: InGaAs		52		1300	1 e19

Table 4.1: Growth sheet of samples HUB1658/60/64/69 used for processing. Label d indicates the doped layers. See table 4.2 and text beneath for details.

sample	average doping (1e17 cm^{-3})
HUB1664	0.7
HUB1660	1.1
HUB1658	1.7
HUB1669	3.9

Table 4.2: Average active region doping densities of samples HUB1658/60/64/69.

In order to investigate the influence of doping density on the QCL performance, four samples were grown. All samples have the same nominal structure, but different average doping of the active regions. The growthsheet for the laser material is given in table 4.1. The columns X(%) and Y(%) denote the mole fraction of indium in InGaAs and InAlAs, respectively. The Si doping concentrations are given in cm^{-3}. The injector/active cell is repeated 40 times. The epitaxial layers of the injector labeled with d, denote that this layers are doped contributing to an average doping density of the entire active region. The doping densities for each sample can be taken from table 4.2.

4.1.2 Reactive ion etching

The etching of the structures plays an important role in the case of QCL processing. All etching steps were done by reactive ion etching (RIE), including the etching of the etch mask layers and the SiN insulation as well as the forming of the InGaAs/InAlAs/AlAs/InP ridge structures.

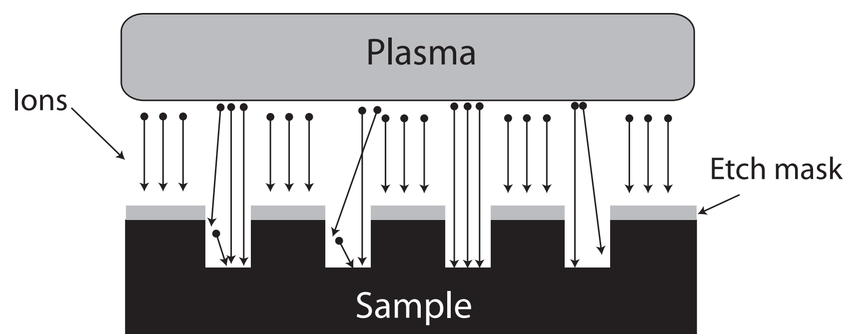

Figure 4.2: Illustration of the working principle of the reactive ion etching.

The plasma etching itself was explored as cheaper alternative to wet solvent resist stripping and then adopted for patterning SiN of its selectivity over resist mask and underlying metallization. In a RIE process the etching of the samples takes place inside a reactor chamber in which several gases are introduced. To ignite a plasma certain conditions concerning the

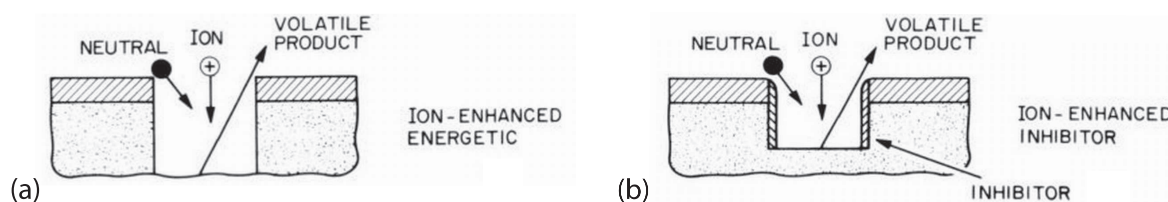

Figure 4.3: (a) Ion enhanced energetical and (b) ion enhanced inhibitor process in RIE [87].

applied voltage, chamber pressure and the dimensions of the chamber have to be fulfilled. Once the plasma has striked it is possible to vary the parameters without losing the discharge. Within this conditions the gas molecules are cracked into ions, which are accelerated towards the material surface being etched. There a reaction takes place forming another gaseous material, which is called the chemical part of reactive ion etching. By gaining more energy the ions are able to knock out atoms out of the etched material leading to a physical aspect of dry etching, without a chemical reaction.
The advantage of RIE is the fast directional removal caused by two proposed mechanisms namely ion-enhanced energetical and ion-enhanced inhibitor processes (Fig. 4.3). In the energy driven regime the ion bombardement modifies the surface in different manners. By damaging the surface highly reactive dangling bonds can be formed as well as disruptions of the lattice structure and even bond-braking of adsorbed surface compounds can take place. This makes the surface more reactive to neutral radicals at the etching bottom and enhances the etching rate but also the aspect ratio (ratio between the height and width of etched trenches). In a ion-inhibitor driven regime the high aspect ratios can be observed due to the sidewall passivation by volatile etching products. These are deposited on vertical as well as horizontal etched surfaces making them inert to the etch. The ion transport perpendicular to the surface removes the passivation layer at the bottom and reduces the thickness of the deposited film on the vertical sidewalls. This leads to an etch rate enhancement only at the bottom surface resulting in a high anisotropy. These ion enhanced processes rely on the possibility of tuning the ratio of physical to chemical etching which can be varied via the chamber pressure and the RF power. The flux of neutrals (note that only a few percent of the atoms are ionized in the plasma process) can be altered independently of the ion flux via the pressure, since the ionization degree of the process plasmas remains constant over the entire range of pressures (1 mbar to several 100 mbar). Therefore, lower pressure increases the physical part of dry etching which is also supported by the increased free mean path of the ions. More energy is gained by passing the RF electric field.
In general by changing the balance of physical and chemical etching it is possible to influence the anisotropy of the etching, since the chemical part is isotropic and the physical part highly anisotropic. The combination of both processes allows vertical as well as rounded etch profiles.

Endpoint detection

In order to control the etch depth several methods exist like residual gas analyzing of etch by-products as well as measuring the increase in pressure when the etching stops. In our facility optical endpoint detection is used. This optical endpoint detection set-up is convenient for monitoring etches of multi-layered structures in which there is a high contrast in the layers' refractive indices at $\lambda_0 = 655nm$. This endpoint detection system consists of a laser source directed perpendicular to the sample, various optics and a camera. In the case of a transparent layer the light is reflected at the top and bottom interface of the layer. When the film thickness changes due to the etching, constructive and destructive interferences occur given by

$$\Delta d = \frac{\lambda_0}{2n} \tag{4.3}$$

The recorded intensity shows oscillations indicating changes in the etchant thickness. When the film is completely removed the oscillations stop. In case of etching a reflective material with a transparent etch mask the reflected intensity shows superposition of both oscillations. In order to distinguish the material corresponding signal one needs a high etchant to mask selectivity.

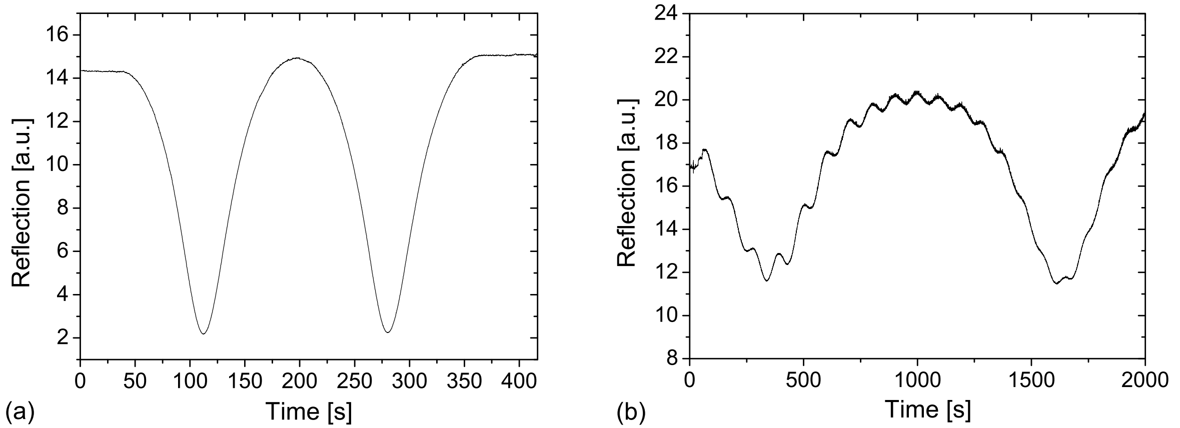

Figure 4.4: Two recorded interferometric endpoint detection oscillations. (a) Etching of $\sim$ 320 nm SiN passivation layer. (b) shows the superposition of the oscillations during the deep etching of InP (high etch rate) with a SiN hard mask (low etch rate).

4.1.3 Deposition technologies

Plasma enhanced chemical vapor deposition

Plasma enhanced chemical vapor deposition (PECVD) is an excellent alternative for depositing a variety of thin films at lower temperatures than those utilized in CVD reactors without settling for a lower film quality. For example, high quality silicon nitride films can be deposited at 300 °C while CVD requires temperatures in the range of 900 °C to produce films with similar quality.

$$3\mathrm{SiH_4} + 4\mathrm{NH_3} \rightarrow \mathrm{Si_3N_4} + 12\mathrm{H_2} \qquad \mathrm{CVD}$$

$$\mathrm{SiH_4} + \mathrm{NH_3} \rightarrow \mathrm{SiNH} + 3\mathrm{H_2} \qquad \mathrm{PECVD}$$

PECVD uses electrical energy to generate a glow discharge in which the energy is transferred into a gas mixture. This transforms the gas mixture into reactive radicals, ions, neutral atoms and molecules. These atomic and molecular fragments interact with a substrate and, depending on the nature of these interactions, either etching or deposition processes occur at the substrate. Since the formation of the reactive and energetic species in the gas occurs by collision in the gas phase, the substrate can be maintained at a low temperature. Hence, film formation can occur on substrates at a temperature which is lower than that in a conventional CVD process, which is a major advantage of PECVD. Some of the desirable properties of PECVD films are good adhesion, low pinhole density, good step coverage, and uniformity. PECVD silicon nitride films contain 15 to 30 % of H bonded either to Si or N. This yields different Si/N ratios which greatly affect the material properties. Deposition at higher pressure tends to build Si poor films. The lower Si content results in an increased etch rate and a higher dielectric strength. Furthermore the refractive index decreases. In our case PECVD was used for $\mathrm{Si}_x\mathrm{N}_y$ deposition used as passivation as well as etch mask in high aspect ratio RIE processes. A radial flow parallel plate reactor as shown in figure 4.5 was used.

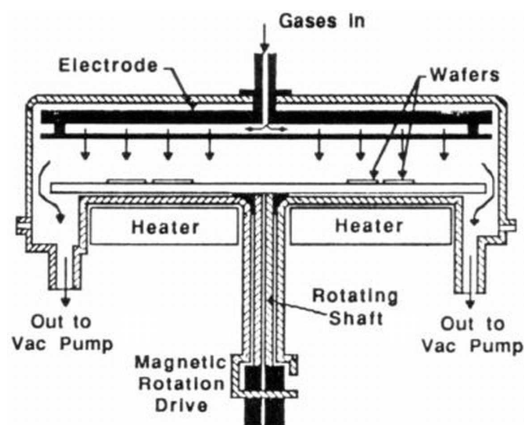

Figure 4.5: Schematic view of a planar reactor [88].

Sputtering

Sputtering is a process operating on an atomic or molecular scale whereby an atom or molecule of a surface is ejected when the surface is struck by a fast incident particle. The momentum of the incident atom is transfered to the atoms in the target material and this momentum transfer can often lead to the ejection of a surface atom - the sputtering process.

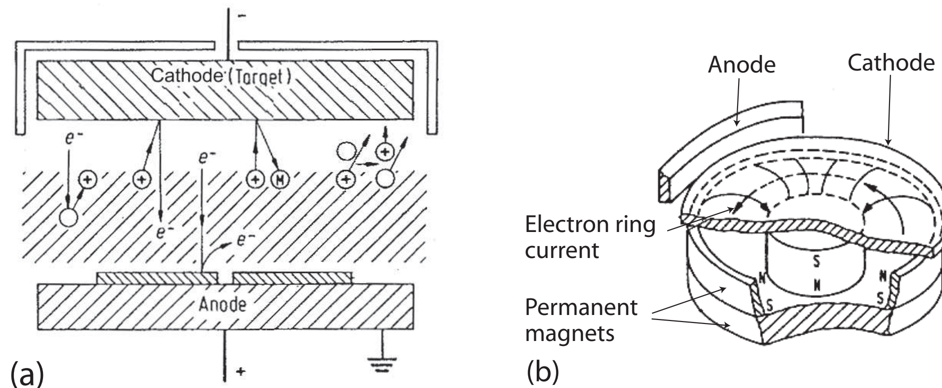

Figure 4.6: (a) Schematic working principle of a sputter deposition facility. (b) A magnetron schematic for improving the sputter rate [89].

In our case a magnetron RF sputter deposition facility is employed to sputter either metals like Au, Ti and Cr or insulators like ZnSe. A schematic of such a simple system is shown in figure (4.6(a)). An electric field is applied between two electrodes causing electrons to be accelerated. These electrons collide with neutral atoms leading to ionization and the generation of ions. To provide ions as bombarding particles an argon plasma is utilized, ensuring that there is no chemical reaction between the incident ions and the target material. The incident ions mainly eject neutral target atoms that are deposited on the substrate to be coated. The magnetron arrangement of the target allows very high sputter rates at small pressures as the ionization degree of the plasma is increased by introducing a magnetic field near the target's surface. The magnetic field is perpendicular to the electric field. Therefore a cylindrical electron current can be formed increasing the lifetime of the electrons in the plasma (Fig. 4.6(b)). One measure of the sputtering process is that of sputtering yield Y. This is defined as the number of atoms sputtered from the surface per incident ion. This number depends on the incorporated target material (Fig. 4.7(a)), and can be tuned by the energy of the incident ions, which is influenced by the RF power and the working pressure . For ion energies below 20 eV the sputter yield is vanishingly small, because this is below the material depending activation energy. It then increases monotonically and almost linearly up to about 1 keV. A typical dependence is shown in figure 4.7(b). The sputtering yield continues to increase, but less than linearly, up to energies of few tens of keV. It then starts to decrease as the incident ions tend

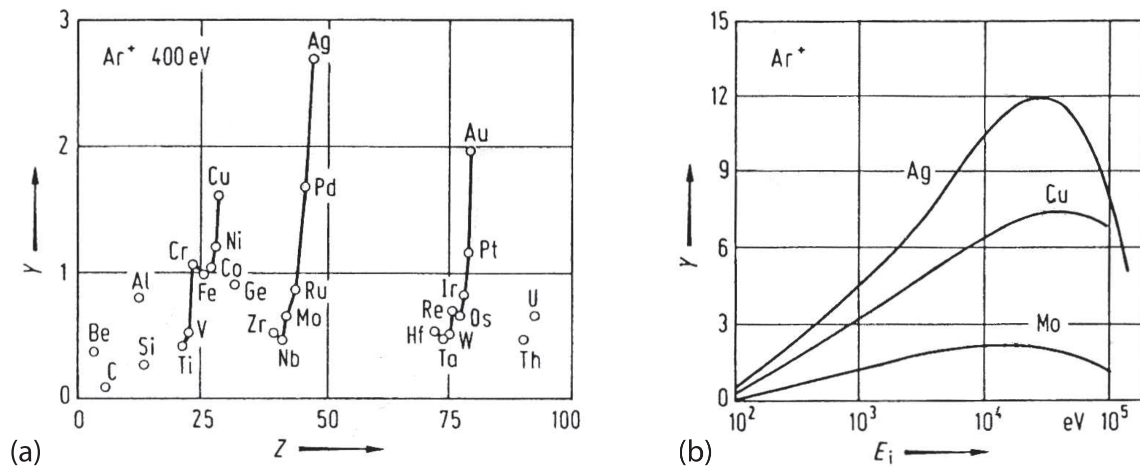

Figure 4.7: (a) Sputter yields Y for different target materials at the ion energy of 400 eV (atomic number Z). (b) shows the dependence of sputter yield on the ion energy E_i for several materials [89].

to penetrate into the sputtering target, rather than causing sputtering. The energy region used for deposition is located where the linear dependency occurs. The ion loses energy to several atoms in a collision cascade and more neutrals can be ejected if more energy is placed. The deposition is non directional comparable to PECVD but shows a smaller side wall deposition.

Evaporation

Evaporation is a common method of thin metal film deposition. The source material is evaporated in a vacuum. The vacuum allows vapor particles to travel directly to the target object (substrate), where they condense back to a solid state (Fig. 4.8(a)). The working pressure is significantly smaller (longer free mean path) than it is for PECVD or sputter deposition which results in a directed deposition only covering areas aimed to the target (in general no side wall deposition). An energy source that evaporates the material to be deposited can be realized as resistive heating or by coupling in RF power via a coil. Another possibility is the electron beam method in which a target anode is bombarded with an, via magnetic beam directed, electron beam formed by a charged filament under high vacuum (Fig. 4.8(b)). The electron beam causes atoms from the target to transform into the gaseous phase. These atoms then precipitate into solid form, coating everything in the vacuum chamber with a thin layer of the anode material.

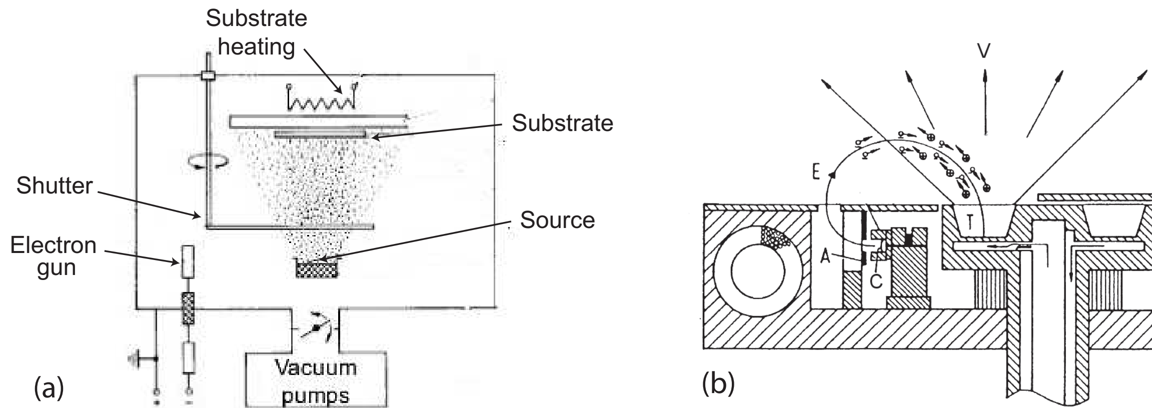

Figure 4.8: (a) Schematic of a typical evaporation system. (b) Electron beam evaporator [89].

4.2 Processing

The processing of the GSMBE grown material was done in the clean room of the Zentrum für Mikro- und Nanostrukturen (ZMNS) at the Technical University of Vienna. Device processing includes the patterning of the structures by optical lithography, the etching of the laser ridges, deposition of insulation layers, thinning of the substrate and providing contact metallization at the top and the back.

In detail, all samples discussed within this thesis, were processed into 10 to 18 μm wide ridge waveguide structures via RIE. The structures were electrically insulated by a $\sim$300 nm SiN layer which was opened along the ridges. Ohmic top contact was realized by electron beam evaporation of Ge/Au/Ni/Au and sputtering of Ti/Au making extended contact pads. The electrical insulation of the lasers from each other was done by a lift off process. The samples were thined to 250 μm before applying Ge/Au/Ni/Au as back ohmic contact. The processed chip holding the laser ridge waveguides was cleaved perpendicular to the ridges in order to provide as-cleaved facets serving as laser mirrors. The annealing of the ohmic contacts was performed by rapid thermal annealing at 365°C for 30 s. Finally the laser bars were soldered epilayer-up by indium on copper mounting plates and contacted by ultrasonic wire bonding.

The etching of the samples based on the InP material system was performed by utilizing a $SiCl_4Ar$ plasma at 240°C. Etching of In consisting material at room temperature leads to a deposition of $InCl_x$ (which is not volatile at lower temperatures) which impedes InP etching drastically. Thus, high temperatures are necessary requireing SiN as etch mask instead of a photoresist, which would melt under these conditions.

List of abbreviations

In the following discriptions several abbreviations are used, which are summarized here.

- AZ5214: Photoresist-Hoechst
- AZ726MIF: Developer-Hoechst
- maP275: positive Photoresist-micro resist technology
- maD331: Developer-micro resist technology
- KOH: Kaliumhydroxide
- HMDS: Hexamethyldisilazane
- H_2O: deionized water
- sccm: standard cubic centimeter per minute
- mask aligner Süss MJB3: (CI1) constant intensity 12 mW/cm^2 @ 365 nm (i-line of Hg lamp)
- RIE: reactive ion etching
- PLOX: Plasma oxidation
- p_{base}: base pressure
- p_{work}: working pressure

All lithography steps (exposure) in the following were done with the maskaligner ”Karl Süss” MJB3 (365nm) with 12 mW/cm^2.

Protocol

- Oxide removement
  KOH (20%) 1 min; rinsing with H_2O 1 min; drying with N_2
- Hard mask patterning
  - PECVD-SiN deposition
    $p_{\mathrm{base}} = 20$ mbar, $p_{\mathrm{work}} = 1$ Torr, gas flow 700 sccm (2% SiH_4/N_2) + 18 sccm NH_3, 10 W RF power, 300° C, typ. deposition rate 11 nm/min, ~700 nm
  - Lithography
    spin coating: photoresist AZ5214 (1:0), 35 s @ 4000 rpm
    baking: 1 min @ 100°C
    exposure: mask ”rim A” (removing of the edges), 60 s
    developing: AZ726MIF, 60 s, rinsing, drying
    exposure: mask ”Ridge small”, 5 s
    developing: AZ726MIF, 25 s, rinsing, drying
  - RIE-Hard mask etching
    $p_{\mathrm{base}} = 8 \times 10^{-6}$ mbar, $p_{\mathrm{work}} = 15$ mTorr, 40 sccm SF_6, 60 W RF power, T $\approx$ 30° C, typ. etch rate 100-150 nm/min, etch depth ~700 nm, Quartz carrier
  - Removal of excess photoresist
    PLOX: 20 s @ 300 W (with TePla 100-E)
    Aceton: ultrasonic bath 30s @ 10%
    Isopropanol
- Etching of ridges
  - RIE-Deep etching
    $p_{\mathrm{base}} = 8 \times 10^{-6}$ mbar, $p_{\mathrm{work}} = 3$ mTorr, 5 sccm $SiCl_4$ + 40 sccm Ar, 200 W RF power, T $\approx$ 240° C, typ. etch rate 100-120 nm/min, etch depth ~5.5 μ m, Silicon carrier
  - Removal of SiN hard mask
    $p_{\mathrm{base}} = 8 \times 10^{-6}$ mbar, $p_{\mathrm{work}} = 15$ mTorr, 40 sccm SF_6, 60 W RF power, T $\approx$ 30° C, typ. etch rate 100-150 nm/min, etch depth ~700 nm, Quartz carrier

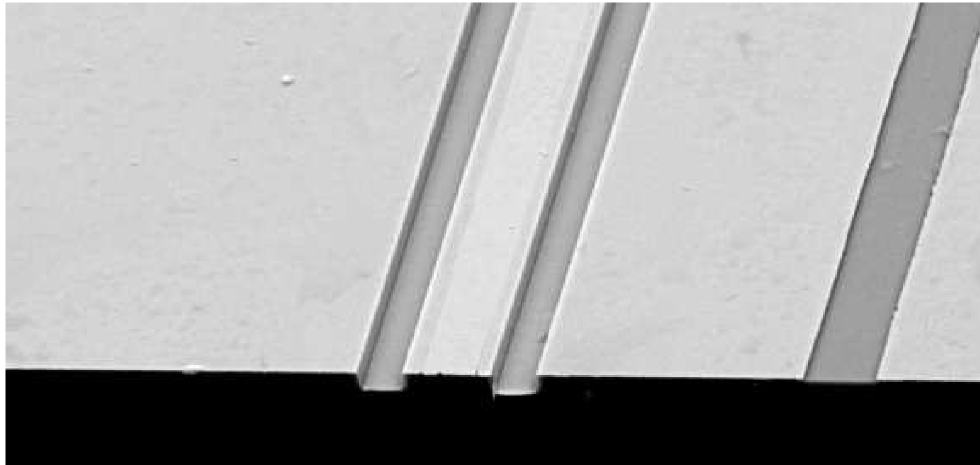

Figure 4.9: SEM picture of a deep etched 14μm wide laser ridge.

- Electrical insulation
  - PECVD-SiN deposition
    $p_{\text{base}} = 20$ mbar, $p_{\text{work}} = 1$ Torr, gas flow 700 sccm (2% SiH_4/N_2) + 18 sccm NH_3, 10 W RF power, 300° C, typ. deposition rate 11 nm/min, ∼300 nm
  - Lithography
    spin coating: photoresist maP275 (1:0), 35 s @ 8000 rpm
    baking: 5 min @ 100°C
    exposure: mask ”rim A” (removing of the edges), 40 s
    developing: maD331, 100 s, rinsing, drying
    exposure: mask ”Isolation small”, 15 s
    developing: maD331, 100 s, rinsing, drying
  - RIE-Insulation opening on top of the ridges
    $p_{\text{base}} = 8\,\text{x}\,10^{-6}$ mbar, $p_{\text{work}} = 3$ mTorr, 5 sccm $SiCl_4$ + 40 sccm Ar, 60 W RF power, T ≈ 240° C, typ. etch rate 100-120 nm/min, etch depth ∼300 nm, Quartz carrier
- Top contact metallization
  - Evaporating ohmic contact

Ge: 15 nm
Au: 30 nm
Ni: 14 nm
Au: 150 nm

- Lift-off
  Aceton: 10 min
  Ultrasonic: 2 min @ 10%
  Isopropanol

- Lithography
  spin coating: HMDS , 35 s @ 4000 rpm
  baking: 30 s @ 100°C
  spin coating: photoresist maP275 (1:0), 35 s @ 8000 rpm
  baking: 5 min @ 100°C
  exposure: mask ”Metal 1”, 35 s
  developing: maD331, 100 s, rinsing, drying

- Ti/Au extended contact pads
  Ti sputtern: 2 x 30 s @ 25 W
  Au sputtern: 12 x 45 s @ 25 W
  typ. deposition rate: Ti 5 nm/min, Au 50 nm/min

- Lift-off
  Aceton: 10 min
  Ultrasonic: 2 min @ 10%
  Isopropanol

• Back contact metallization

- Substrate thinning
  Sample sticked epilayer-down with wax to a holder @ 100° C, thinned to a final thickness of 200 -250 μm, removed with aceton

- Evaporating ohmic contact

Ge: 15 nm
Au: 30 nm
Ni: 14 nm
Au: 150 nm

sample	length (mm)
HUB1664B_B1	1.96
HUB1660A_B2	1.97
HUB1658A_B1	2
HUB1669A_B1	1.93

Table 4.3: A list of the processed laser bars and the corrsponding lengths.

After the processing the samples were cleaved into ~2 mm long laser bars with several 10 to 18 μm wide laser ridges. These were soldered by indium to copper mounting plates at 170° C. The laser ridges were contacted to the copper plates with an ultrasonic wire bonder (Kulicke & Soffa Model 4523AD Bonder, 100 μm diameter gold wire). See table 4.2 for a list of processed laser bars.

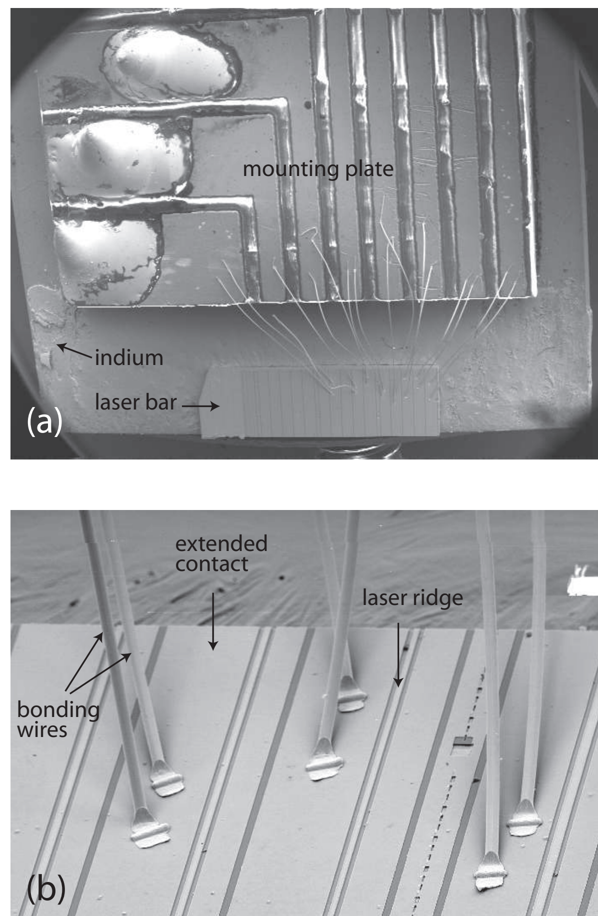

Figure 4.10: (a) The laser bar is soldered with indium to the copper mounting plate. (b) SEM close-up of the wire bonded laser ridges.

4.3 Characterization

4.3.1 Electrical and optical measurement setups

The processed QCLs were characterized with respect to their current-voltage (IV) as well as their optical power versus current (LI) characteristics. Futhermore emission spectra and far-field mode profiles were investigated.
The mounting plate holding the laser bar was mounted on a copper cold finger inside a liquid-nitrogen flow cryostate. Each laser ridge was electrically contacted with input ports fixed to the cryostate. The temperature of the cold finger was adjusted within the region T = 78 K...300 K by means of a heater and a temperature controller. The zinc selenide (ZnSe) cryostate window (focus f = 1.5 inch, diameter d = 1 inch) that is used for out-coupling has a transmittance of $T = 0.67$ at 4 μm for normal incidence. The measurements were performed in a pulsed applied voltage mode.

Current-voltage characterization

For pulsed mode operation two pulse generators (HP 8114A and AVTECH AVL2B) were utilized. Measuring of voltage and current was done by a Tektronix TDS 3032B digital oscilloscope. In general, electrical connections were carried out using coaxial cables, with an impedance of 50 Ω. Due to the short pulses (100ns) the circuit is realized impedance matched for clearly defined driving pulses. Therefore, one input is connected with a serial 48 Ω resistance that, together with the working resistance of the QCL ($R_{QCL} \approx 2\,\Omega$), matches the coaxial cable impedance. This 48 Ω input is used to drive the QCL via the pulser. Sensing the current was performed by an I/V transducer into 50 Ω and has to be corrected due to the

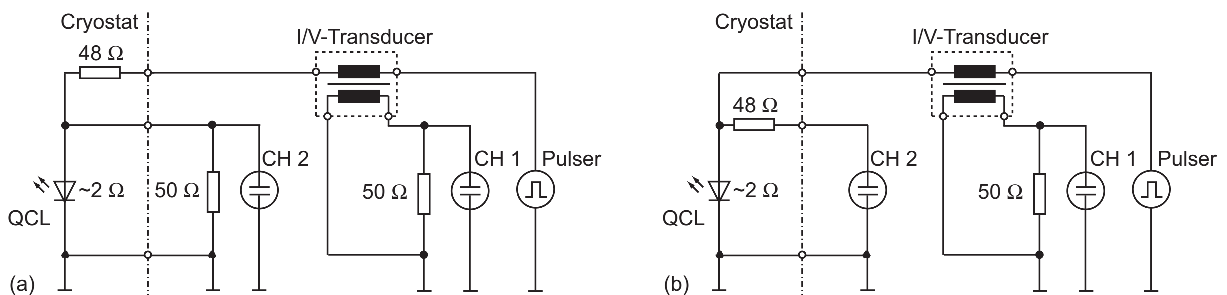

Figure 4.11: (a) Standard wiring plan for driving the laser and measuring current and voltage. For an impedance matched operation an additional 48 Ω is utilized. The current is sensed by means of an I/V transducer. The oscilloscope channels are terminated with a 50 Ω resistor. (b) For higher driving currents the lasers were current-fed at the input without the matching resistor.

parallel voltage line current. The second direct port is used to measure the voltage being terminated with 50 Ω at the oscilloscope. Figure 4.11(a) shows the impedance matched setup. The pulses, supplied by the AVTECH pulse generator, are limited to 100 ns short pulses and a repetition rate of 5 kHz. The peak output power is given by 2450 W into 50 Ω. In order to circumvent the pulse limitation, the HP pulser was used, providing long pulses (duty cycle up to nearly 100%) and pulse frequences up to 9 MHz. However, its peak power into 50 Ω is limited to 50 W. For higher driving currents the input lines were switched, thus feeding the laser directly. This on the other hand leads to a worse matching for the voltage measurement at the input that was connected to the 48 Ω port without the 50 Ω at the oscilloscope (Fig. 4.11(b)).

Optical power characterization

The optical peak power from one laser facet was measured via the Princeton 5210 Lock-In Amplifier which is triggered by the pulse generator TTL signal. The input voltage of the Lock-In is the electrical signal generated by the internal room temperature internal deuterated triglycine sulfate (DTGS) detector of the Fourier-transform infrared (FTIR) spectrometer. For the LI-characteristics, the current was measured with the oscilloscope, as mentioned before.

Fourier transform infrared spectroscopy

The emíssion spectra of the mid-infrared devices were recorded using a Bruker Equinox IFS55 Fourier-transform (FT) spectrometer with a spectral range of 1.3 to 27 μm and a nominal resolution of 0.2 cm^{-1}. A FT spectrometer is based on a Michelson interferometer where the incident light is splitted by a semitransparent mirror and propagates along the two arms of the interferometer. The optical path of one arm is kept constant, whereas the optical path of the other arm is changed via a moving mirror. The two beams are then recombined by a beam splitter and directed to the detector. The interferogram, i.e. the detector signal as function of mirror position, is recorded and Fourier transformed in order to obtain the energy spectrum. The spontaneous emission, featuring relatively weak signals, was measured in amplitude modulation step scan mode. Here, the mirror stops at discrete positions and the detector signal is registered at the modulation frequency by a lock-in amplifier. This leads to a significantly low noise emission spectra.
Figure 4.12 demonstrates the complete setup. The copper plate holding the laser bar is fixed to the cold finger placed in the cryostate. The latter is placed in front of an anti-reflection coated ZnSe lens (focus f = 1.5 inch, diameter d = 2 inch) in order to collimate the light. This laser beam is then fed through the spectrometer to the detector. The internal DTGS detector is integrating the signal with very high time constants compared to the applied frequences. Instead, in order to consider the relatively fast heating of the laser during a puls, which results

in a spectral shift, an external Peltier cooled Vigo Systems detector is used. The combination of this detector with fast response and the Boxcar technique, relatively clear emission spectra were obtained. For spontaneous emission measurements an external liquid-nitrogen cooled indium antimonide (InSb) detector was utilized, which provides a higher sensitivity than the DTGS detector.

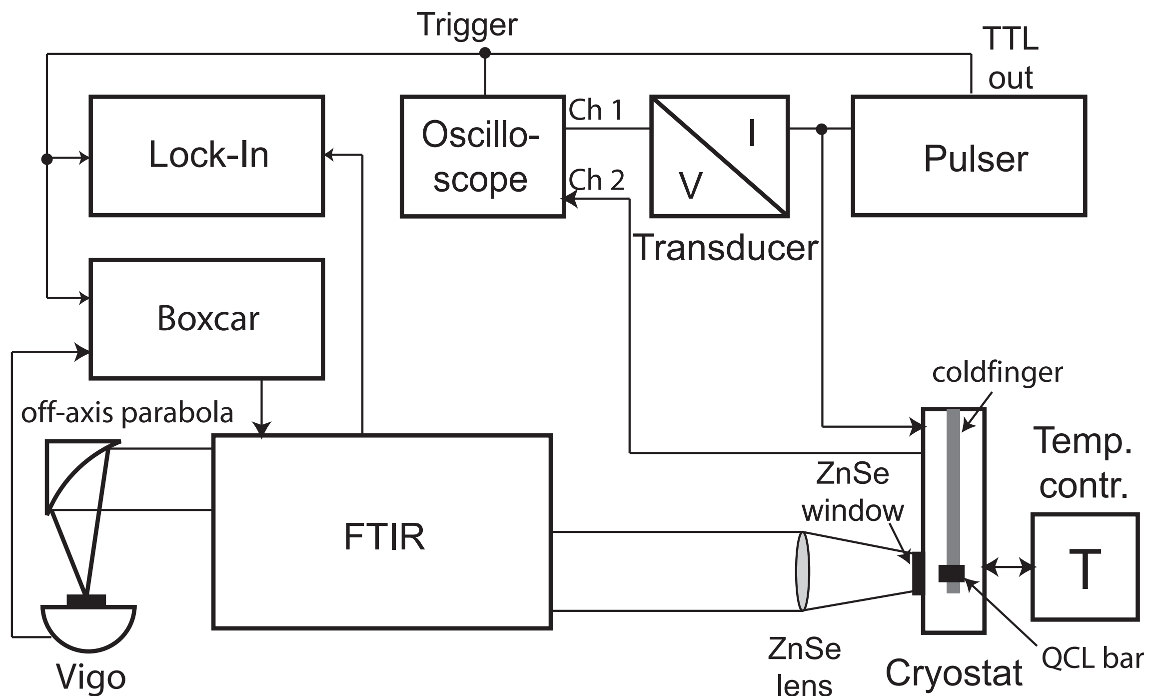

Figure 4.12: An overview of the QCL measurement setup. The mounting plate holding the laser bar is fixed to the cold finger, which is placed in the liquid-nitrogen cooled cryostate. The temperature is held constant by a temperature controller. The light is coupled out via a ZnSe window and collimated by a anti-reflection coated ZnSe lens. For spectrum measurements the beam is fed through the fourier-transform-infrared spectrometer, and focused by a gold-coated off-axis parabola onto the Vigo detector. The detected signal is sampled by the Boxcar, that is triggered by the pulser, and then forwarded to the FTIR to be Fourier transformed. Light intensity is measured with a lock-in amplifier, that is locked onto the puls repetition rate via a TTL signal supplied by the pulser. Current and voltage are measured with a digital oscilloscope also triggered by the pulser.

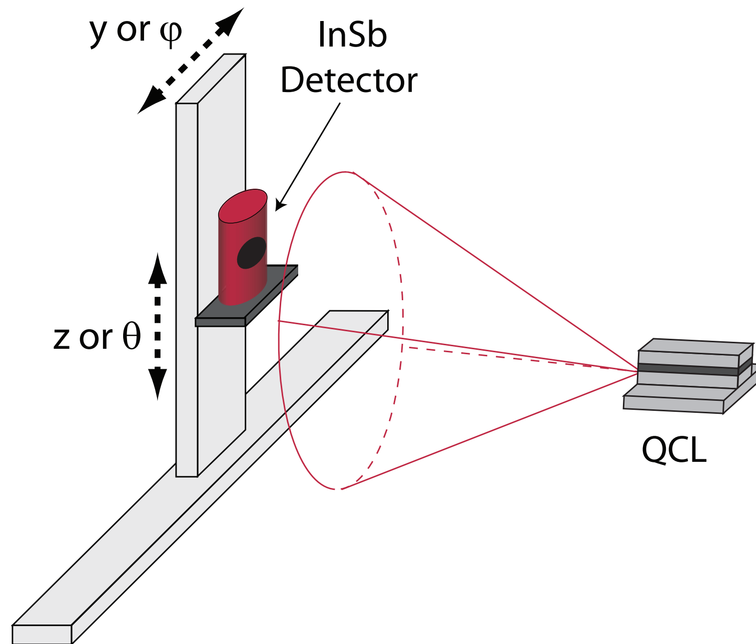

Figure 4.13: A scheme of the farfield measurement setup. An InSb detector is mounted on a translation stage.

Farfield measurements

The far-field mode patterns were obtained with the liquid-nitrogen cooled InSb detector placed on a translation stage. The detector signal is fed to the Lock-in amplifier. The position of the stage can be controlled in two directions by software, thus two- as well as one-dimensional far-field plots can be recorded.

4.3.2 Experimental results

Active region

Figure 4.14 the shows active region design of the QCLs presented in this thesis. This design is similar to the bound-to-continuum design but with a thinner injection barrier [86]. Laser action takes place between the injector state 2 and the ground state 1 of the single QW active region. The lower lasing state 1 is depopulated fast due to the carrier tunneling into the manifold of states of the miniband I, of the next injector stage. In this case, the huge population inversion is constantly provided. The gain, however, depends strongly on the applied field. As the field increases on the one hand the energy separation of the states 2 and 1 increases due to increased potential drop between the two states but also the spatial overlap between states 2 and 1 increases. Thus, gain (also the dipole matrix element of the 2-to-1 transition) can be treated as the tuning factor in this design. The consequence of the comparable thin barrier

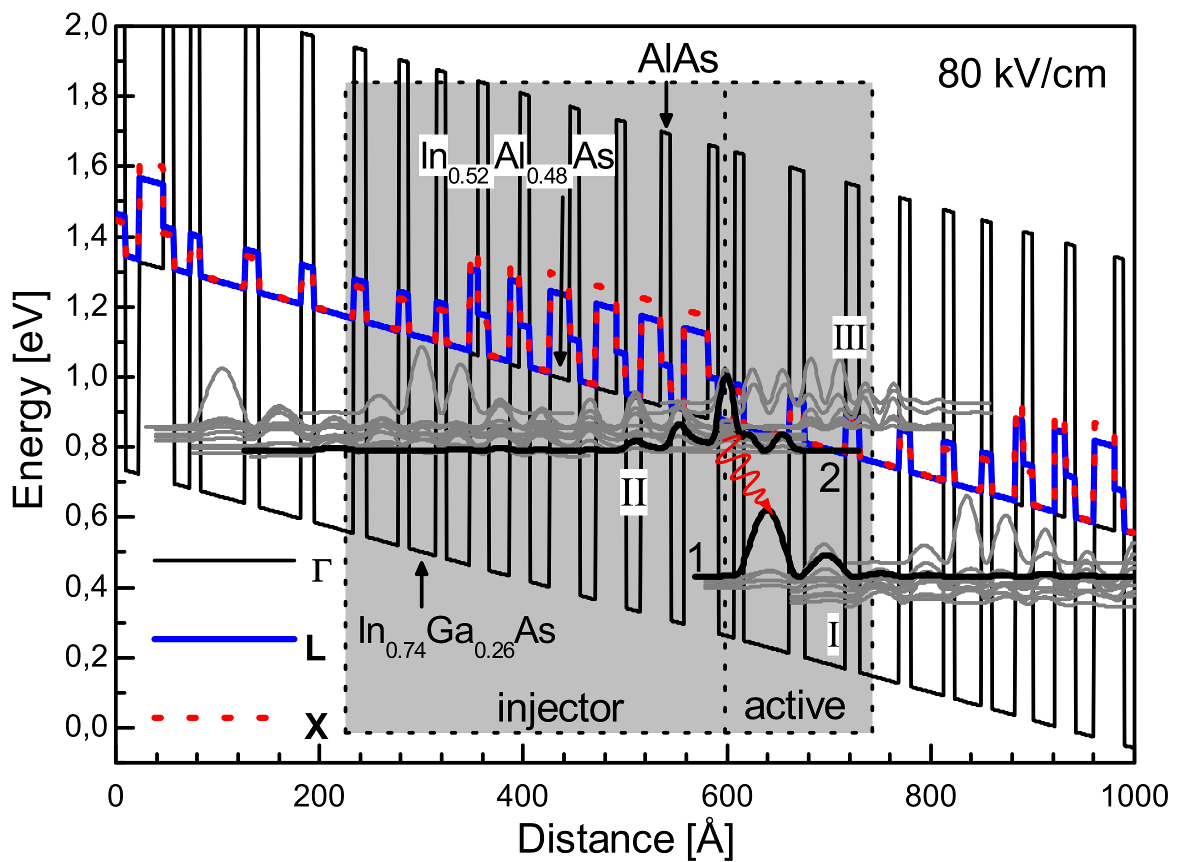

Figure 4.14: Conduction band diagram and selected wavefunctions (moduli squared giving the probability function). Injector and active regions are shown under an applied bias of 80 kV/cm. The laser transition takes place between states 2 and 1. Beside the direct valley Γ also the indirect valleys L ans X are illustrated.

is that some states of the injector miniband II (separated by 1-10 meV from the upper lasing state 2 [86]) also spatially overlap with the lower lasing state 1. These multiple transitions result in a broad gain spectra, as reflected in the broad electroluminescence (Fig. 4.15). Despite the broad gain, this design allows population inversion for multiple transitions due to the high injection efficiency into the upper lasing state, the low carrier leakage into the miniband III and into the indirect valleys.

Incorporating three semiconductor compounds (InGaAs/InAlAs/AlAs) in the injector and active region design, an independent manipulation of the conduction band profile (injector region miniband) as well as the strain profile over a single cascade, can be achieved. Two component $In_{0.52}Al_{0.48}As$/AlAs) barriers, used in the active cell, allowed tuning the quantum well and barrier thicknesses almost independently.

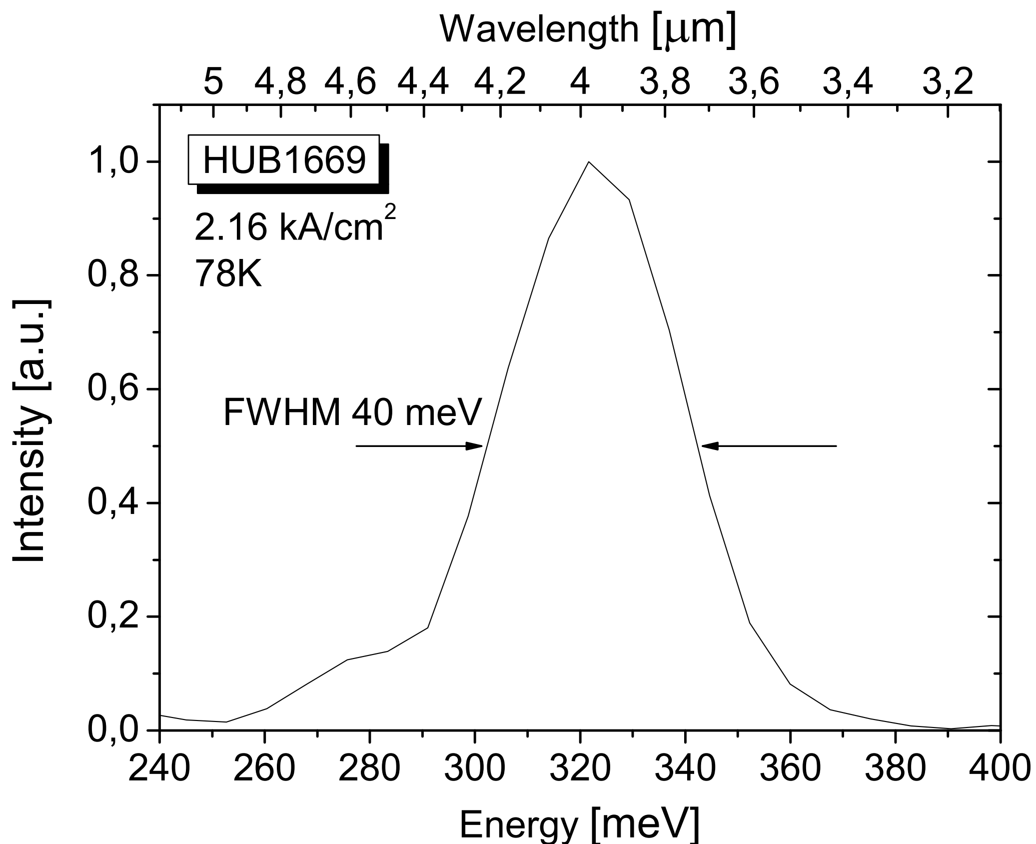

Figure 4.15: Spontaneous emission spectrum of sample HUB1669 recorded at a drive current density of 2.16 kA/cm^2 at 78 K. This current condition is well below threshold.

Doping dependent characteristics

The dependence of the threshold current density, the maximum current density, the optical peak power and the emission wavelength on the active region doping density at 78 K is shown in figure 4.16(a), (b), (c) and (d), respectively. The lowest threshold current density of $J_{th} = 1.85\,kA\,/cm^2$ was observed for a doping level 1.1 x $10^{17}\,cm^{-3}$ (HUB1660). Since increasing of doping leads to higher losses (free carrier absorption) one would expect a monomonotonic rise in laser threshold [90]. For doping densities 0.7 x $10^{17}\,cm^{-3}$

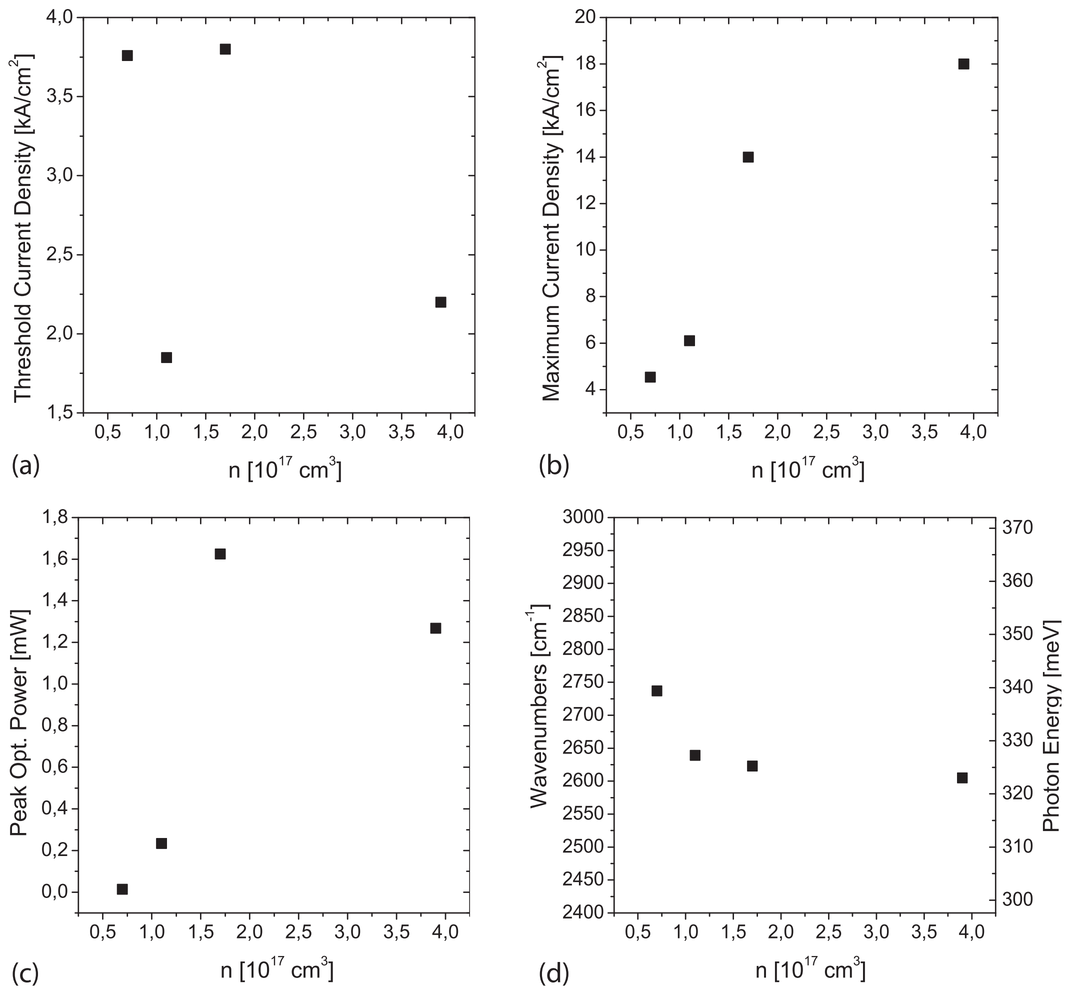

Figure 4.16: Doping dependence of (a) threshold current density, (b) maximum current density, (c) peak optical power and (d) emission energy of 12 μm wide laser ridges (see table 4.2 on page 54 for exact lengths) at 78 K. The lasers were operated in pulsed mode (repetition length 5kHz and 100 ns pulse length).

(HUB1664), 1.7 x $10^{17}\,cm^{-3}$ (HUB1658) and 3.9 x $10^{17}\,cm^{-3}$ (HUB1669) the thresholds $3.76\,kA\,/cm^2$, $3.8\,kA\,/cm^2$ and $2.2\,kA\,/cm^2$ were found, respectively. This, however, gives a non-linear behaviour. One possible explanation for the higher threshold current density for the lowest doping could base on the about 100 wavenumbers higher emission characteristic

(Fig. 4.16(d)). This higher emission energy reduces the effective barrier height which leads to thermal emission into the continuum as well as tunneling out of the active region (see section 3.1.3). Both loss mechanisms reduce the lifetime in the upper laser level. Hovever, due the higher emission energy compared to the other samples, in this case this leads to a higher threshold. For the 1.7 x $10^{17}\,cm^{-3}$ doped sample the emission wavelength is almost the same as that one of the lower threshold samples, so the explanation mentioned before should not be correct in this case. Also the possibility of bad cleaved facets, what would increase the mirror losses, should be neglected since several laser ridges were characterized showing the same behaviour. The maximum current density shows almost a linear dependence on doping which is described by equation 2.32 (Fig. 4.16(d)). A maximum optical peak power $P = 1.625\,W$ was observed for the doping level 1.7 x $10^{17}\,cm^{-3}$ (Fig. 4.16(c)). The emission wavelength was determined as $\lambda \approx 3.8\,\mu m$. In general, no strong deviation (20 wavenumbers between dopings 1.1 x $10^{17}\,cm^{-3}$ and 3.9 x $10^{17}\,cm^{-3}$) in case of emission wavelength was found except for the lowest doped sample. On the one hand this can be attributed to the structure design, on the other hand the doping dependent field distribution can influence the lasing transition energy at low doping densities [91].

Temperature dependence

Figure 4.17 shows the logarithmic plot of the threshold current density recorded at different temperatures. The symbols indicate the experimental data and the solid lines denote an ex-

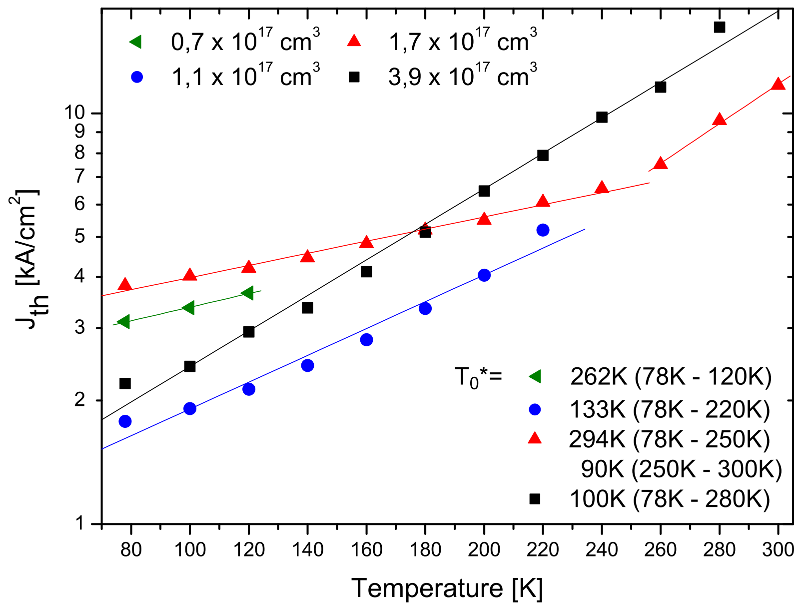

Figure 4.17: Threshold current density J_{th} as a function of heat sink temperatures. Symbols indicate the experimental data for $12\,\mu m$ wide and $\sim\ 2\,mm$ long laser ridges and solid lines denote an exponential fit.

ponential fit using equation 3.18. From these fits the characteristic temperature T_0^*, that is a measure for the temperature sensitivity, were extracted. The higher T_0^* the lower the temperature sensitivity. A maximum $T_0^* = 294\,K$ was found for the sample HUB1658 in the temperature range $78\,K - 250\,K$. Between 250 K and 300 K the thermal emission into the continuum and the tunneling out of the active region becomes more significant yielding a lower $T_0^* = 90\,K$. For the highest doped sample the lasing performance is influenced by the backfilling of the lower laser state due to the higher Fermi energy caused by the high doping. In this case $T_0^* = 100\,K$ was obtained over the entire lasing range.
The peak optical power over the temperature is shown in figure 4.18. Again, sample HUB1658 shows the best performance with a lasing region of $78\,K - 300\,K$. At room temperature an optical power of 10 mW was measured. Beside the lowest obtained power the lasing region of the lowest doped sample is reduced to 120 K, what is again an indication of the loss mechanisms due to the reduced effective barrier height to the continuum.
The slope efficiency $\partial P_{opt}/\partial I$ defined as the ratio between the change in optical power and the laser current is plotted in figure 4.19. At 78 K the maximum power efficiency of $1.12\,W/A$ was obtained for sample HUB1658. The parabolic fit shown in the inset of figure 4.19) estimates a maximum power efficiency $1.32\,W/A$ at a doping level of 2.52 x $10^{17}\,cm^{-3}$).

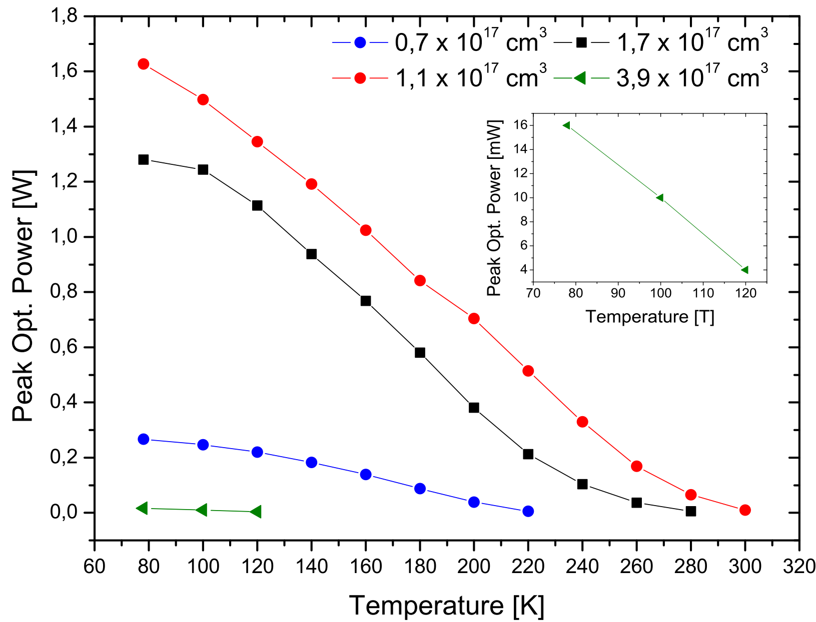

Figure 4.18: Peak optical power as a function of heat sink temperatures for $12\,\mu m$ wide and $\sim 2\,mm$ long laser ridges. Solid lines denote connection lines of the discrete data and not a fit. Inset shows the data for sample HUB1664.

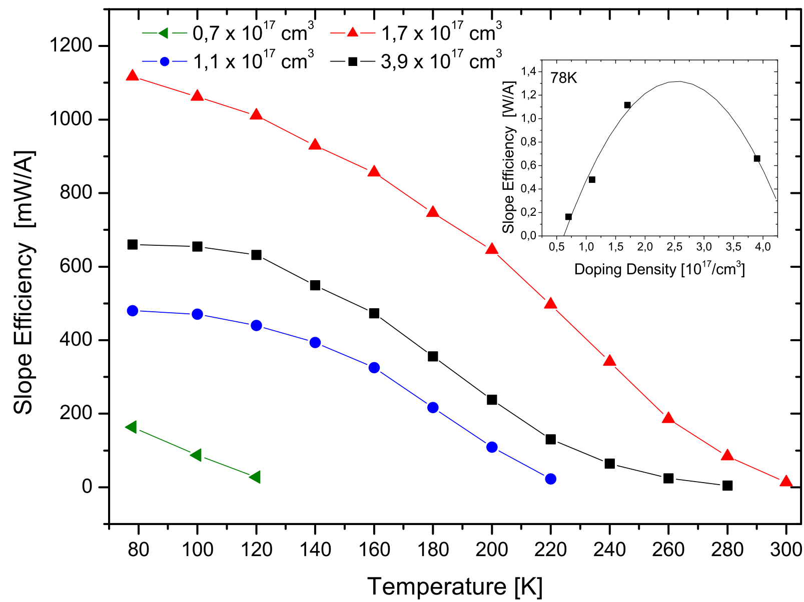

Figure 4.19: Slope efficiency as a function of heat sink temperatures for $12\,\mu m$ wide and $\sim 2\,mm$ long laser ridges. Solid lines denote connection lines of the discrete data and not a fit.

X-ray Diffraction

High-resolution X-ray diffraction (HRXRD) was performed on all samples and is shown in figure 4.20. The highest peak indicates the diffraction at the InP substrate as well as the

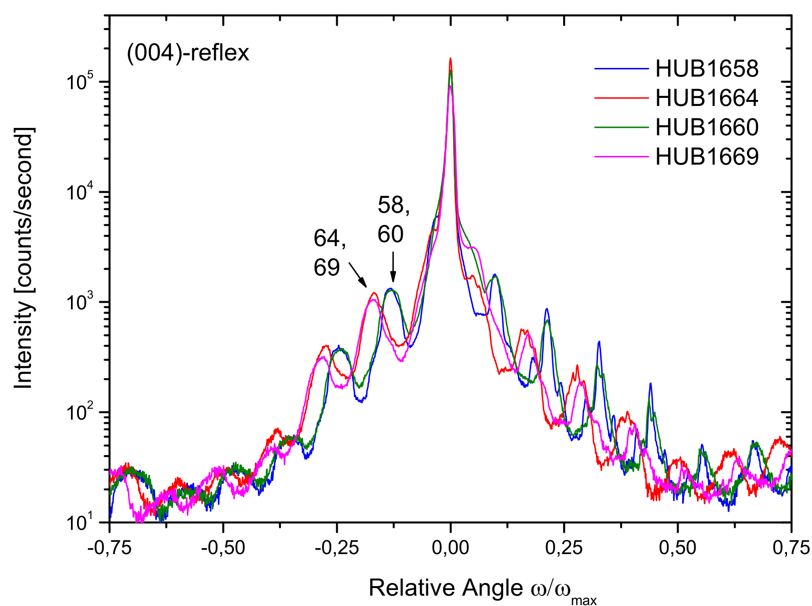

Figure 4.20: High-resolution X-ray diffraction spectrum of all four samples.

cladding layers. Further satellites mark the periodicity of the 30 periods of InGaAs/InAlAs/AlAs active/injector regions. As can be seen in the plot there is some difference in distance from the highest 0.-order peak to the 1.-order satellite between samples HUB1664/58 and HUB1660/69 (indicated by arrows). This can be dedicated to different material composition. In this case this could mean that the indium fraction in the QW or barriers in not the same for all samples. However, this could explain the higher threshold for the samples HUB1664/58 and the wavelength deviation shown in figure 4.16(d). The equidistant spacing between the higher order satellites for all four samples indicates the same active region period length L_P.

Individual characteristics

The wall-plug efficiency P_{opt}/P_{el} given as the ratio between the emitted optical power and the injected electrical power $P_{el} = U \cdot I$ (voltage U and laser current I). This value is significant

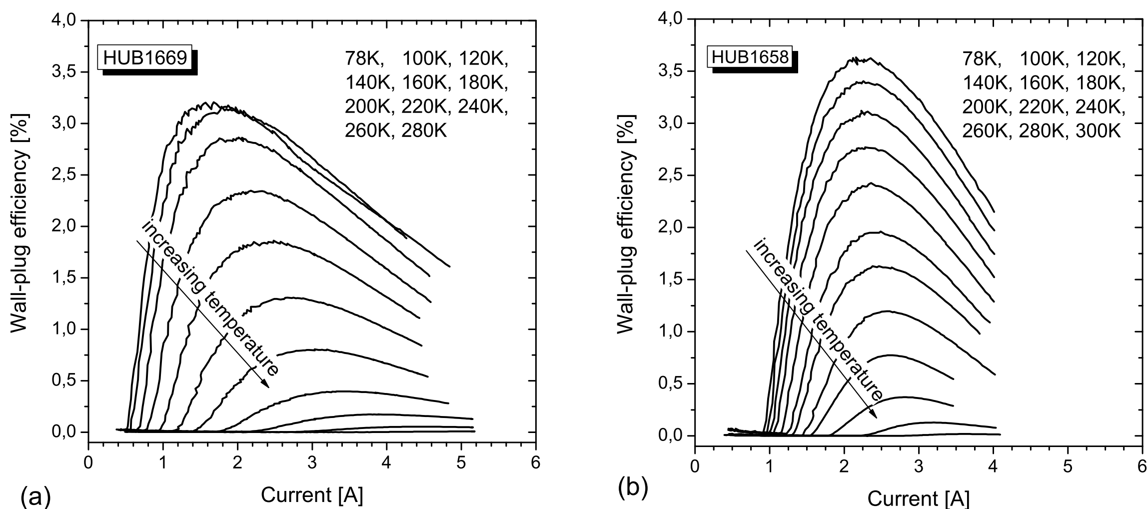

Figure 4.21: Wall-plug efficiency of samples (a) HUB1669 and (b) HUB1658 at different heat sink temperatures.

for continuous wave operation since a high efficiency indicates less dissipated power yielding reduced heating of the active region. Despite the higher threshold current sample HUB1658 shows the highest wall-plug efficiency of $3.63\,\%$ at 78K (Figure 4.21(b)). This higher value, compared to sample HUB1669 with wall-plug efficiency of $3.22\,\%$ (Figure 4.21(a)), can be explained by the higher optical power and slope efficiency.

Figure 4.22(a) shows the LI and IV-characteristics of a $12\,\mu m$ wide and $2\,mm$ long laser (HUB1658). Emission was observed from 78 K to 300 K. The break down in optical power ("roll-over") occurs when sufficient voltage has been applied to break the coupling between the injector and the excited upper laser state, thus reducing the injection efficiency. At room temperature lasing starts at $11.58\,kA/cm^2$ 4.22(b) and shows a peak power of 10 mW.

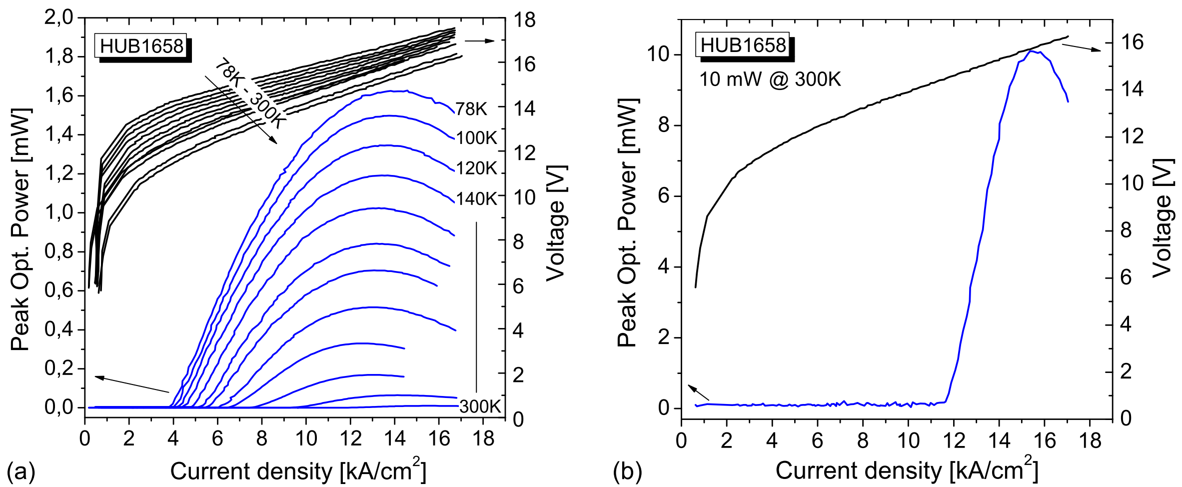

Figure 4.22: (a) LI- and IV-characteristic of sample HUB1658. (b) Room temperature characteristic.

The characterization of the lowest doped sample showed an interesting effect. During the first measurement (solid line), after cooling the cryostate down to 78K, the laser current was increased and held constant at the roll-over point. Instead of an usually constant peak power a decrease in power was observed (Figure 4.23(a)). Turning off the laser and the measuring the LI for a second time showed a reduced peak power and the lasing stoped after a while (dashed line). Further measurements showed no lasing. After heating up to RT and cooling down to 78 K, the laser was characterized again. The QCLs were lasing again with the highest power at

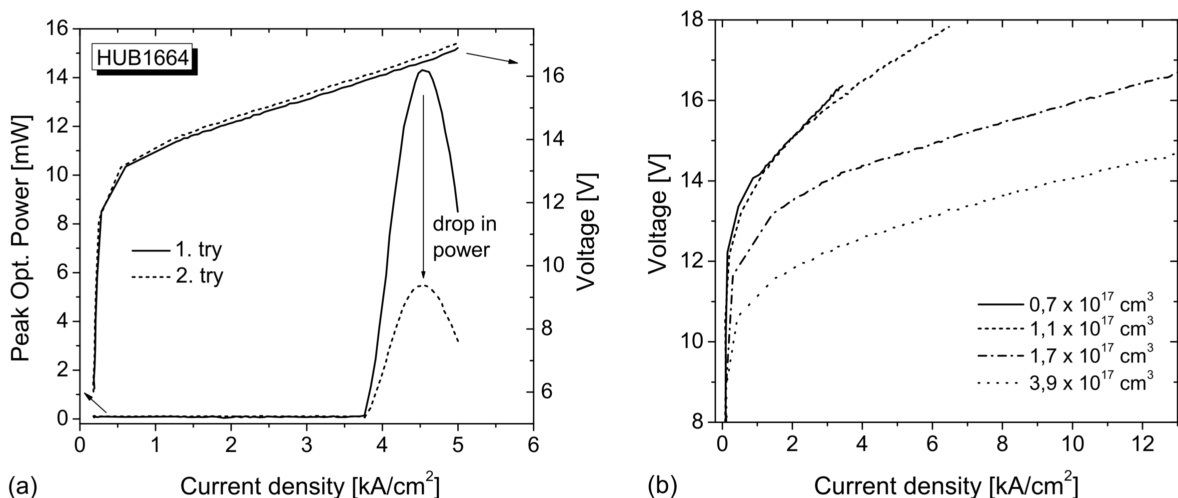

Figure 4.23: LI- and IV-characteristic of a 12 μm wide and 1.96 mm long HUB1664 laser at 78 K. (b) Voltage dependance on doping density at 78 K.

the first turn-on followed by a decrease in power and a stop of lasing. One explanation can be given by reducing the effective carrier density due to traps in the material. At low temperatures the energy of the electrons is to low to escape out of the traps. This lower electron density leads to reduced inversion population and thus optical power. By heating up to a certain temperature enough activation energy can be gained to extract the electrons from the traps. However, this effect is only significant for low doping densities. For higher dopings some electrons are also being trapped, but there are still sufficient carriers to reach high population inversion. This loss of electrons can also be confirmed by the somewhat higher voltage of the IV-characteristic in case of the second measurement ((Figure 4.23(a)). In general a higher laser voltage was observed for higher doping densities (Figure 4.23(b)).

Emission spectra

In order to obtain high resolution emission spectra the heating effect in the active region has to be considered. Due to the higher thermal conductance of InP compared to GaAs measuring a proper emission spectra requires more effort. During one electrical pulse (100 ns) the laser ridge goes through a heating-cooling cycle that changes the refractive index. This on the other hand results in a change of the spectral mode spacing (Eq. 3.13). Since the DTGS detector is integrating, the obtained spectra is given by a superposition of several mode spacings caused by the active region heating during one electrical pulse. This yields a broad and ”blurred” spectrum (inset of Fig. 4.24). Using a fast (non-integrating) Vigo detector and the Boxcar technique the influence of the temperature can be minimized. The working principle of a Boxcar is based on the ”Sample and Hold” method. Here, the electrical signal of the detector is sampled within a gate width by the Boxcar and held constant during the Fourier transformation, in this way eliminating the refractive index shift. Figure 4.24 shows the emission spectra obtained for three different gated puls length, according to the described method. The longer the sampled pulse length the higher the heating influence, resulting in superpositioned resonances (compare 20ns and 100 ns gate lengths). Spectra recorded at different currents are shown in figure 4.25. The broadening of the spectrum at higher currents can be explained by the coupling of the injector miniband states and the lower laser level due to the relatively thin injection barrier (see section 4.3.2 on page 58).

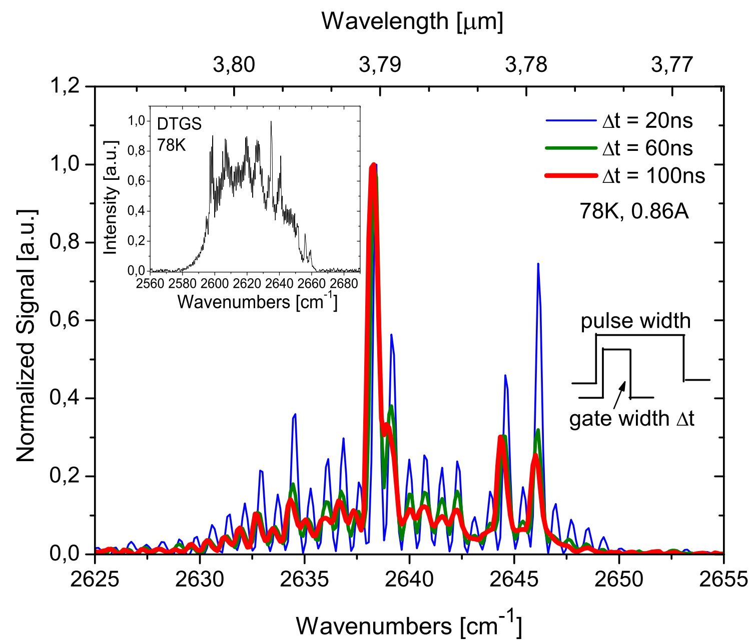

Figure 4.24: Emission spectra of a 12 μm wide and 1.97 mm long sample HUB1660 with different Boxcat gate length (pulse length 100 ns, 5 kHz, 78 K) at a drive current of 0.86 A. Inset shows a emission spectrum obtained with the DTGS detector under the same conditions.

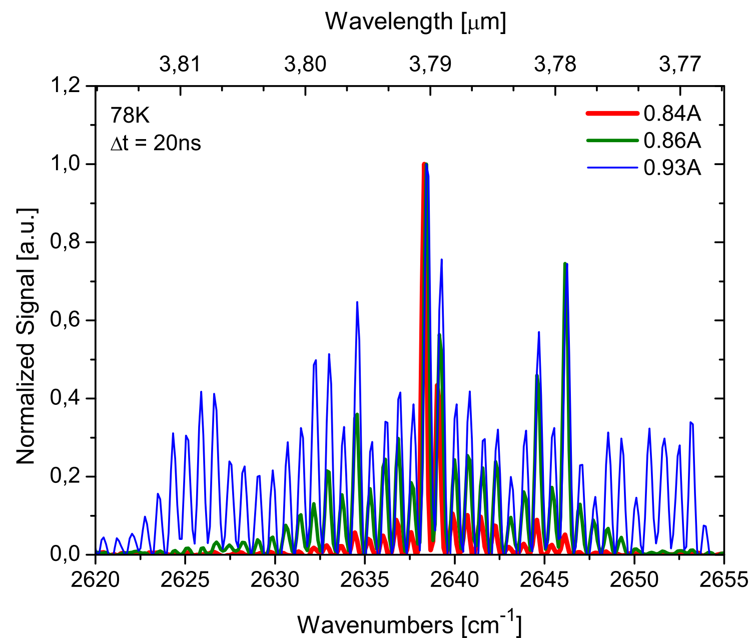

Figure 4.25: Emission spectra of a 12 μm wide and 1.97 mm long sample HUB1660 at different drive currents with a 20 ns long gate (pulse length 100 ns, 5 kHz, 78 K).

Far-field measurement

The far-field distribution of the laser emission was determined according to the setup described in fig. 4.13 using a liquid-nitrogen cooled InSb detector. The distance between the detector and the laser chip was 124 mm. Figure 4.26 shows two facet beam intensity distributions obtained for the samples HUB1658 and HUB1664. Both structures show a single lobe (lowest order mode) far-field pattern described by a Gauss-beam in both directions. The full width at half maximum (FWHM) in vertical direction is about 40°. In lateral direction the FHWM depends on the laser width and is about 20° for 12 μm wide laser ridges.

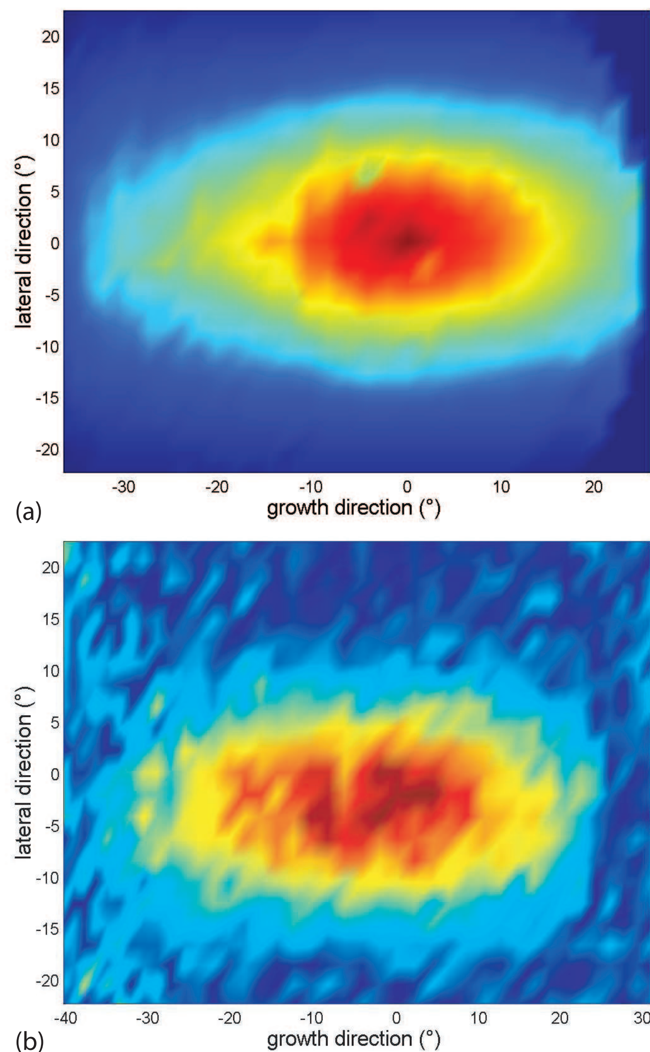

Figure 4.26: Far-field distributions of sample (a) HUB1658 and (b) HUB1664 of 12 μm wide ridges at 78 K.

Chapter 5

Summary and outlook

The development of quantum cascade lasers operating at short wavelength (3-5 μm) is driven by a number of applications including communication, gas sensing for both environmental and medical uses and military countermeasures. The approach toward this wavelength range has been taken by incorporating semiconductor structures with high conduction band discontinuities. A further possibility to extend the conduction band offset is given by strain-compensated structures which require more effort in the growth of such semiconductor heterostructures.
In this thesis investigation on quantum cascade lasers based on the strain-compensated InGaAs/ InAlAs/AlAs material system grown on an InP substrate has been performed. By utilizing this kind of semiconductor heterostructures QCLs with a wavelength of $3.05\,\mu m$ have been realized, which is the shortest wavelength presented so far in this material system [26]. However, room temperature as well as continuous wave operation has proven to be very challenging.
The main part of this work dealt with the influence of doping density in the active region of the QCLs. Several differently doped samples were characterized showing a strong dependence of lasing properties on the doping level: Maximum values for peak optical power, slope efficiency and wall-plug efficiency have been measured showing an optimum doping level for this kind of structure. In this case also the best temperature performance was achieved and lasing up to room temperature was observed. The measurements showed the there is a limit in the low doping region. The lasers have to be doped sufficiently to avoid reducing effective electron density due to the deep traps in the semiconductor material. Thus, a minimum doping density is a necessity to provide stable lasing performance. In case of the maximum current density, which determines the lasers' dynamic range, an almost linear dependence on the doping was found. The doping of the active region could have an influence on the field destribution in a QCL which yields different emission energies for generally the same designed QCLs. In order to unambiguously determine the origin of the observed variation of the lasing

energy with the doping, a more detailed modelling of the QCLs as a function of doping density would be necessary.
In general, strain-compensated structures based on InGaAs/InAlAs/AlAs/InP offer several benefits. On the one hand the comparably large conduction band discontinuity can be used to realise QCLs emitting down to $\sim 3\,\mu m$, but on the other hand due to this increased band offset, loss mechanisms can be reduced for smaller emission energies. In both cases further improvement of lasing performance can be achieved by the finding the optimal doping density for the active region, as shown in this thesis.

Appendix A

Appendix: Material parameters

parameter	unit	GaAs	AlAs	InAs	InP
crystal structure	-	zinc blende	zinc blende	zinc blende	zinc blende
a_0	Å	5.6533	5.6611	6.0583	5.8687
$E_g(\Gamma)$	eV	1.424	2.9	0.36	1.344
$E_g(X)$	eV	1.9	2.17	1.37	2.19
$E_g(\Lambda)$	eV	1.71	2.4	1.08	1.93
Δ_{SO}	eV	0.34	0.3	0.39	0.11
m_e^*	m_0	0.063	0.19	0.023	0.08
$m_h^* h$	m_0	0.51	0.76	0.41	0.6
$m_l^* h$	m_0	0.082	0.15	0.026	0.089
ε_{static}	-	12.9	10.06	15.5	12.5
ε_∞	-	10.89	8.162	12.3	9.61
a_C	eV	-7.17	-5.64	-5.08	-6.0
a_C	eV	1.16	2.47	1.0	0.6
b	eV	-2.0	-2.3	-1.8	-2.0
C_{11}	MPa	1.188	1.202	0.834	1.011
C_{12}	MPa	0.538	0.57	0.454	0.561
$\hbar\omega_{LO}$	meV	36	50	30	43

Table A.1: Material parameters for the binary III/V semiconductor compounds GaAs, AlAs, InAs and InP at $T = 300\,K$ [29], [37], [92].

parameter	unit	$In_xGa_{1-x}As$	$In_yAl_{1-y}As$
$E_g(\Gamma)$	eV	0.477	0.7
$E_g(X)$	eV	1.4	0
$E_g(\Lambda)$	eV	0.33	0
Δ_{SO}	eV	0.15	0.15
m_e^*	m_0	0.0091	0.049
$m_h^* h$	m_0	-0.145	0
$m_l^* h$	m_0	0.0202	0
a_C	eV	2.61	-1.4

Table A.2: Nonzero bowing parameters $\mathcal{C}$ for the ternary III/V semiconductor compounds $In_xGa_{1-x}As$ and $In_yAl_{1-y}As$ [92].

References

[1] R. D. Dupuis. An introduction to the development of the semiconductor laser. *IEEE J. Quant. Electr.*, 23:651, 1987.

[2] R. N. Hall, G. E. Fenner, J. D. Kingsley, T. J. Soltys, and R. 0. Carlson. Coherent light emission from GaAs junctions. *Phys. Rev. Lett.*, 9:366, 1962.

[3] M. I. Nathan, W. P. Dumke, G. Burns, Jr. F. H. Dill, and G. Lasher. Stimulated emission of radiation from GaAs p-n junctions. *Appl. Phys. Lett.*, 1:62, 1962.

[4] Jr. N. Holonyak and S. F. Bevacqua. Coherent (visible) light emission from Ga($As_{1-x}P_x$) junctions. *Appl. Phys. Lett.*, 1:82, 1962.

[5] M. A. Herman and H. Sitter. *Molecular Beam Epitaxy*. Springer Verlag, Berlin Heidelberg New York, second edition, 1996.

[6] A. Y. Cho, editor. *Molecular Beam Epitaxy - Key papers in applied physics*. American Institute of Physics, New York, 1994.

[7] H. Kressel and H. Nelson. Close-confinement gallium arsenide p-n junction lasers with reduced optical loss at room temperature. *RCA Review*, 30:106, 1969.

[8] I. Hayashi and M. B. Panish. A low-threshold room-temperature injection laser. *IEEE J. Quant. Electr.*, 5:211–212, 1969.

[9] I. Hayashi, M. B. Panish, P. W. Foy, and S. Sumski. Junction lasers that operate continuously at room temperature. *Appl. Phys. Lett.*, 17:109–111, 1970.

[10] S. Nakamura, T. Mukai, and M. Senoh. Candela-class high-brightness InGaN/AlGaN double-heterostructure blue-light-emitting diodes. *Appl. Phys. Lett.*, 64:1687–1689, 1993.

[11] J. M. Gaines, R. R. Drenten, K. W. Habern, T. Maeshall, P. Mensz, and J. Petruzello. Blue-green injection lasers containing pseudomorphic $Zn_{1-x}Mg_xS_ySe_{1-y}$ cladding layers and operating up to 394 k. *Appl. Phys. Lett.*, 62:2462–2464, 1993.

[12] Z. Shi, M. Tacke, A. Lambrecht, and H. Böttner. Midinfrared lead salt multi-quantum-well diode lasers with 282 K operation. *Appl. Phys. Lett.*, 66:2537–2539, 1995.

[13] J. Faist, F. Capasso, D. L. Sivco, C. Sirtori, A. L. Hutchinson, and A. Y. Cho. Quantum cascade laser. *Science*, 264:553–556, 1994.

[14] R. F. Kazarinov and R. A. Suris. Possibility of amplification of electromagnetic waves in a semiconductor with a superlattice. *Sov. Phys. Semicond.*, 5:797–800, 1971.

[15] R. F. Kazarinov and R. A. Suris. Electric and electromagnetic properties of semiconductors with a superlattice. *Sov. Phys. Semicond.*, 6:120–131, 1972.

[16] G. Strasser, P. Kruck, M. Helm, J. N. Heyman, L. Hvozdara, and E. Gornik. Mid-infrared electroluminescence in GaAs/AlGaAs structures. *Appl. Phys. Lett.*, 71:2892–2894, 1997.

[17] C. Sirtori, P. Kruck, S. Barbieri, P. Collot, J. Nagle, M. Beck, J. Faist, and U. Oesterle. GaAs/Al_xGa_{1-x}As quantum cascade lasers. *Appl. Phys. Lett.*, 73:3486–3488, 1998.

[18] G. Strasser, S. Gianordoli, L. Hvozdara, W. Schrenk, K. Unterrainer, and E. Gornik. GaAs/AlGaAs superlattice quantum cascade lasers at $\lambda = 13\mu\mathrm{m}$. *Appl. Phys. Lett.*, 76:1345–1347, 1999.

[19] C. Gmachl, A. Tredicucci, D. L. Sivco, A. L. Hutchinson, F. Capasso, and J. A. Y. Cho. Bidirectional semiconductor laser. *Science*, 286:749, 1999.

[20] C. Gmachl, D. L. Sivco, J. N. Baillargeon, A. L. Hutchinson, F. Capasso, and A. Y. Cho. Quantum cascade lasers with a heterogeneous cascade: Two-wavelength operation. *Appl. Phys. Lett.*, 79:572, 2001.

[21] C. Gmachl, D. L. Sivco, R. Colombelli, F. Capasso, and A. Y. Cho. Ultra-broadband semiconductor laser. *Nature*, 415:6874, 2002.

[22] M. Beck, D. Hofstetter, T. Aellen, J. Faist, U. Oesterle, M. Illegems, E. Gini, and H. Melchior. Continuous wave operation of a mid-infrared semiconductor laser at room temperature. *Science*, 295:5553–5557, 2002.

[23] A. Evans, J. S. Yu, S. Slivken, and M. Razeghi. Continuous-wave operation of λ ~4.8 μm quantum-cascade lasers at room temperature. *Appl. Phys. Lett.*, 85:2166, 2004.

[24] R. Köhler, A. Tredicucci, F. Beltram, H. E. Beere, E. H. Linfield, A. G. Davis, D. A. Ritchie, R. C. Iotti, and F. Rossi. Terahertz semiconductor-heterostructure laser. *Nature*, 417:156–159, 2002.

[25] M. P. Semtsiv, M. Wienold, S. Dressler, and W. T. Masselink. Short-wavelength ($\lambda \approx 3.3$ μm) InP based strain-compensated quantum cascade laser. *Appl. Phys. Lett.*, 89:211124, 2006.

[26] M. P. Semtsiv, M. Wienold, S. Dressler, and W. T. Masselink. Short-wavelength ($\lambda \approx 3.05$ μm) InP based strain-compensated quantum cascade laser. *Appl. Phys. Lett.*, 90:051111, 2007.

[27] A. B. Chen and A. Sher. *Semiconductor Alloys-Physics and Materials Engineering*. Plenum Press, New York and London, 1995.

[28] M. L. Cohen and J. R. Chelikowsky. *Electronic Structure and Optical Properties of Semiconductors*. Springer Verlag, Berlin, Heidelberg, second edition, 1988.

[29] M. Levinstein, S. Rumyantsev, and M. Suhr, editors. *Ternary and Quarternary III-V Compounds*, volume 2 of *Handbook Series on Semiconductor Parameters*. World Scientific, Singapor, New York, London, Hong Kong, 1999.

[30] M. J. Kelly. *Low-Dimensional Semiconductors*. Clarendon Press, Oxford, 1995.

[31] J. H. Van der Merwe. Crystal Interfaces. Part II. Finite Overgrowths. *J. Appl. Phys.*, 34:123, 1962.

[32] J. W. Matthews and A. E. Blakeslee. Defects in epitaxial multilayers: I. Misfit dislocations. *J. Cryst. Growth*, 27:118, 1974.

[33] S. C. Jain, M. Willander, and H. Maes. Stress and strains in epilayers, stripes and quantum structures of III-V compound semiconductor. *Semicond. Sci. Technol.*, 11:641–671, 1996.

[34] R. People and J. C. Bean. Calculation of critical layer thickness versus lattice mismatch for Ge_xSi_{1-x}/Si strained-layer heterostructures. *Appl. Phys. Lett.*, 47:322, 1985.

[35] C. G. van de Walle. Band lineups and derformation potentials in the model-solid theory. *Phys. Rev. B*, 39:1871–1883, 1989.

[36] Pallab Bhattacharya. *Properties of Lattice-Matched and Strained Indium Gallium Arsenide*. INSPEC, the Institution of Electrical Engineers, London, 1993.

[37] S. Adachi. *Physical Properties of III/V Semiconductor Compounds: InP, InAs, GaAs, GaP, InGaAs and InGaAsP*. John Wiley & Sons, New York, 1992.

[38] W. W. Chow, editor. *Semiconductor-Laser Physics*. Springer Verlag, Berlin Heidelberg New York, 1994.

[39] C. Sirtori, F. Capasso, and J. Faist. Nonparabolicity and sum rule associated with bound-to-bound and bound-to-continuum transitions in quantum wells. *Phys. Review B*, 50:8663–8674, 1994.

[40] J. Smet, C. G. Fonstad, and Qing Hu. Intrawell and interwell intersubband transitions in multiple quantum wells for far-infrared sources. *J. Appl. Phys.*, 79:9305–9320, 1996.

[41] Ed. H. C. Liu and F. Capasso. *Intersubband Transitions in Quantum Wells: Physics and Device Applications II*. Academic Press, San Diego, 2000.

[42] G. Yu, N. L. Rowell, D. J. Lockwood, and P. J. Poole. Infrared dielectric response function of strained $In_{1-x}Ga_xAs$/InP epilayers. *Appl. Phys. Lett.*, 81:2175–2177, 2002.

[43] G. Yu, N. L. Rowell, D. J. Lockwood, and P. J. Poole. Erratum: „infrared dielectric response function of strained $In_{1-x}Ga_xAs$/InP epilayers" [appl. phys. lett. 81, 2175 (2002)]. *Appl. Phys. Lett.*, 82:1136, 2003.

[44] L. Pavesi, R. Houdré, and P. Giannozi. Strain and alloying effects on the electronic andvibrational properties of $In_yAl_{1-x}As$ on InP. *J. Appl. Phys.*, 78:470, 1995.

[45] S. Emura, T. Nagakawa, S. I. Gonda, and S. Shimizu. Raman spectra of $Al_xIn_{1-x}As$ grown by molecular-beam epitaxy. *J. Appl. Phys.*, 62:4632, 1987.

[46] J. Faist, C. Sirtori, F. Capasso, L. Pfeiffer, and K. W. West. Phonon limited intersubband lifetimes and linewidths in a two–dimensional electron gas. *Appl. Phys. Lett.*, 64:872–874, 1994.

[47] S. Barbieri, C. Sirtori, H. Page, M. Stellmacher, and J. Nagle. Design strategies for GaAs-based unipolar lasers: Optimum injector-active region coupling via resonant tunneling. *Appl. Phys. Lett.*, 78:282 – 284, 2001.

[48] C. Sirtori, F. Capasso, J. Faist, A. L. Hutchinson, D. L. Sivco, and A. Y. Cho. Resonant tunneling in quantum cascade lasers. *IEEE J. of Quantum Electron.*, 34:1722 – 1729, 1998.

[49] J. Faist, F. Capasso, C. Sirtori, D. L. Sivco, J. N. Baillargeon, A. L. Hutchinson, S. G. Chu, and A. Y. Cho. High power mid-infrared ($\lambda = 5\mu$m) quantum cascade lasers operating above room temperature. *Appl. Phys. Lett.*, 68:3680–3682, 1996.

[50] L. C. West and S. J. Eglash. First observation of an extremely large dipole infrared transition within the conduction band of a GaAs well. *Appl. Phys. Lett.*, 46:1156–1158, 1985.

[51] C. Gmachl, F. Capasso, D. L. Sivco, and A. Y. Cho. Recent progress in quantum cascade lasers and applications. *Rep. Prog. Phys.*, 64:1533–1601, 2001.

[52] G. Scamarcio, F. Capasso, J. Faist, C. Sirtori, D. L. Sivco, A. L. Hutchinson, and A. Y. Cho. High-power infrared (8 μm wavelength) superlattice lasers. *Science*, 276:773–776, 1997.

[53] J. Faist, M. Beck, and T. Aellen. Quantum-cascade lasers based on a bound-to-continuum transition. *Appl. Phys. Lett.*, 78:147–149, 2001.

[54] C. Pflügl, W. Schrenk, S. Anders, G. Strasser, C. Becker, C. Sirtori, Y. Bonetti, and A. Müller. High-temperature performance of GaAs-based bound-to-continuum quantum-cascade lasers. *Appl. Phys. Lett.*, 83:4698–4700, 2003.

[55] E. E. Mendez and G. Bastard. Wannier-Stark ladders and Bloch oscillations in superlattices. *Physics Today*, 6:34, 1993.

[56] L. Esaki and L.L. Chang. New transport phenomenon in a semiconductor superlattice. *Phys. Rev. Lett.*, 33:495, 1974.

[57] H.T. Grahn. *Semiconductor superlattices*. World Scientific Publishing, Singapore, 1995.

[58] J. Faist, F. Capasso, C. Sirtori, D. L. Sivco, A. L. Hutchinson, S. N. G. Chu, and A. Y. Cho. Narrowing of the intersubband electroluminescent spectrum in coupled-quantum-well heterostructures. *Appl. Phys. Lett.*, 65:94–96, 1994.

[59] H. Schneider and K. von Klitzing. Thermionic emission and gaussian transport of holes in a GaAs/Al_x/Ga_{1-x} multiple-quantum-well structure. *Phys. Rev. B*, 38:6160–6165, 1988.

[60] A. M. Fox, D. A. B. Miller, G. Livescu, J. E. Cunningham, and W. Y. Jan. Quantum well carrier sweep out: Relation to electroabsorption and exciton saturation. *IEEE J. Quantum. Electron.*, 27:2281–2295, 1991.

[61] C. Mann. *Entwurf und Charakterisierung von Quantenkaskadenlasern*. PhD thesis, Albert-Ludwigs-Universität Freiburg im Breisgau, Fakultät f"ur Mathematik und Physik, 2004.

[62] D. Hofstetter, T. Aellen, M. Beck, and J. Faist. High-temperture operation of distributed feedback quantum-cascade lasers at 5.3 μm. *Appl. Phys. Lett.*, 78:396–398, 2001.

[63] D. Hofstetter, M. Beck, T. Aellen, J. Faist, U. Oesterle, M. Ilegems, E. Gini, and H. Melchior. Continuous wave operation of a 9.3 μm quantum cascade laser on a peltier cooler. *Appl. Phys. Lett.*, 78:1964–1966, 2001.

[64] L. R. Wilson, D. A. Carder, M. J. Steer, J. W. Cockburn, M. Hopkinson, C. K. Chia, G. Hill, and R. Airey. Strategies for reducing the emission wavelength of GaAs-AlAs quantum cascade laser. *Phys. E*, 13:835, 2002.

[65] J. Faist, F. Capasso, D. L. Sivco, A. L. Hutchinson, S. N. G. Chu, and A. Y. Cho. Short wavelength ($\lambda \approx 3.4\ \mu m$) quantum cascade laser based on strain compensated InGaAs/InAlAs. *Appl. Phys. Lett.*, 72:680–682, 1998.

[66] M. P. Semtsiv, M. Ziegler, S. Dressler, W. T. Masselink, N. Georgiev, T. Dekorsy, and M. Helm. Above room temperature operation of short wavelength (3.8 μm) strain-compensated $In_{0.73}Ga_{0.27}As$–AlAs quantum cascade lasers. *Appl. Phys. Lett.*, 85:1478–1480, 2004.

[67] L. Diehl, D. Bour, S. Corzine, J. Zhu, G. Höfler, M. Loncar, M. Trocolli, and F. Capasso. High-temperature continuous wave operation of strain-balanced quantum cascade lasers grown by metalic organic vapor-phase epitaxy. *Appl. Phys. Lett.*, 89:081101, 2006.

[68] J. Faist, C. Gmachl, M. Striccoli, C. Sirtori, F. Capasso, D. L. Sivco, and A. Y. Cho. Quantum cascade disk lasers. *Appl. Phys. Lett.*, 69:2456–2458, 1996.

[69] S. Gianordoli, L. Hvozdara, G.Strasser, W. Schrenk, K. Unterrainer, and E. Gornik. GaAs/AlGaAs-based microcylinder lasers emitting at 10 μm. *Appl. Phys. Lett.*, 76:1045–1047, 1999.

[70] L. Hvozdara, A. Lugstein, S. Gianordoli, W. Schrenk, G. Strasser, K. Unterrainer, E. Bertagnolli, and E. Gornik. Self-aligned coupled cavity GaAs/AlGaAs midinfrared quantum-cascade laser. *Appl. Phys. Lett.*, 77:1077–1079, 2000.

[71] R. Maulini, M. Beck, J. Faist, and E. Gini. Broadband tuning of external cavity bound-to-continuum quantum-cascade lasers. *Appl. Phys. Lett.*, 84:1659–1661, 2004.

[72] J. Faist, C. Gmachl, F. Capasso, C. Sirtori, D. L. Sivco, J. N. Baillargeon, A. L. Hutchinson, and A. Y. Cho. Distributed-feedback quantum cascade lasers. *Appl. Phys. Lett.*, 70:2670–2672, 1997.

[73] W. Schrenk, N. Finger, S. Gianordoli, L. Hvozdara, G. Strasser, and E. Gornik. GaAs/AlGaAs distributed feedback quantum cascade lasers. *Appl. Phys. Lett.*, 76:253–255, 2000.

[74] Ed. H. C. Liu and F. Capasso. *Intersubband Transitions in Quantum Wells: Physics and Device Applications I.* Academic Press, San Diego, 2000.

[75] D. Hofstetter, J. Faist, M. Beck, and U. Oesterle. Surface-emitting $10.1\,\mu\mathrm{m}$ quantum-cascade distributed feedback lasers. *Appl. Phys. Lett.*, 75:3769–3771, 1999.

[76] W. Schrenk, N. Finger, S. Gianordoli, L. Hvozdara, G. Strasser, and E. Gornik. Surface emitting distributed feedback quantum cascade lasers. *Appl. Phys. Lett.*, 77:2086–2088, 2000.

[77] C. Pflügl, M. Austerer, W. Schrenk, S. Golka, G. Strasser, R. P. Green, L. R. Wilson, J. W. Cockburn, A. B. Krysa, and J. S. Roberts. Single-mode surface-emitting quantum-cascade lasers. *Appl. Phys. Lett.*, 86:211102, 2004.

[78] R. Colombelli, K. Srinivasan, M. Troccoli, O. Painter, C. Gmachl, D. M. Tennant, A. M. Sergent, D. L. Sivco, A. Y. Cho, and F. Capasso. Quantum cascade surface-emitting photonic crystal laser. *Science*, 302:1374–1377, 2004.

[79] G. Scarpa, N. Ulbrich, A. Sigl, M. Bichler, D. Schuh, M. C. Amann, and G. Abstreiter. Improved large optical cavity design for $10.6\,\mu m$ (Al)GaAs quantum cascade lasers. *Phys. E*, 13:844–847, 2002.

[80] C. Hilsum. Simple empirical relationship between mobility and carrier concentration. *Electron. Lett.*, 10 (13):259–260, 1974.

[81] F. Capasso, A. Y. Cho, J. Faist, A. L. Hutchinson, C. Sirtori, and D. L. Sivco. *United States Patent*, 5,502,787, 1996.

[82] M. K. Gunde and M. Macek. Infrared optical constants and dielectric response functions of silicon nitride and oxynitride films. *Phys. Stat. Sol. (a)*, 183:439–449, 2001.

[83] M. A. Ordal, L. L. Long, R. J. Bell, S. E. Bell, R. R. Bell, R. W. Alexander Jr., and C. A. Ward. Optical properties of the materials Al, Co, Cu, Au, Fe, Pb, Ni, Pd, Pt, Ag, Ti and W in the infrared and far infrared. *Appl. Optics*, 22:1099–1119, 1983.

[84] H. Page, C. Becker, A. Robertson, G. Glastre, V. Ortiz, and C. Sirtori. 300 K operation of a GaAs based quantum cascade laser at $\lambda \approx 9 \mu m$. *Appl. Phys. Lett.*, 78:3529–3531, 2001.

[85] S. Izumi, Y. Kouji, N. Hayafuji, and K. Sato. Gas source molecular beam epitaxy as a multi-wafer epitaxial production technology. *J. Cryst. Growth*, 201/202:8–11, 1999.

[86] M. Semtsiv. *InGaAs-AlAs and InGaAs-InGaP Strain-Compensated Heterostructures for Short-Wavelength Intersubband Transitions and Lasers*. PhD thesis, Humboldt Universität Berlin, Mathematisch-Naturwissenschaftliche Fakultät I, 2004.

[87] D. Manos and D. L. Flamm. *Plasma etching*. Academic Press, London, 1989.

[88] S. M. Rossnagel, J. J. Cuomo, and W. D. Westwood. *Handbook of plasma processing*. Noyes Publications, USA, 1990.

[89] A. Bergauer and C. Eisenmenger-Sittner. *Physik und Technologie Dünner Schichten*. Technische Universität Wien, LVA Nr. : 133.463.

[90] T. Aellen, M. Beck, N. Hoyler, M. Giovannini, E. Gini, and J. Faist. Doping in quantum cascade lasers. i. inalas-ingaas/inp midinfrared devices. *J. Appl. Phys.*, 100:043101, 2006.

[91] M. Giehler, R. Hey, H. Kostial, S. Cronenberg, T. Ohtsuka, L. Schrottke, and H. T. Grahn. Lasing properties of GaAs(Al,Ga)As quantum-cascade lasers as a function of injector doping density. *Appl. Phys. Lett.*, 82:671, 2003.

[92] I. Vurgaftman, J. R. Meyer, and L. R. Ram-Mohan. Band parameters for III-V compound semiconductors and their alloys. *J. Appl. Phys.*, 89:5815–5875, 2001.

Conference contributions

S. Schartner, M. Austerer, E. Mujagić, L. Hoffmann, W. Schrenk, A.M. Andrews, P. Klang and G. Strasser, *Probing the photonic band structure by resonant responsivity enhancement in QWIPs* (invited talk), 9th International Conference on Intersubband Transitions in Quantum Wells (ITQW07), Ambleside, UK, 9.-14.9.2007.

E. Mujagić, M. P. Semtsiv, M. Austerer, S. Schartner, W. T. Masselink and G. Strasser, *Influence of doping density variation in InP-based strain-compensated quantum-cascade lasers* (oral), 8th International Conference on Mid-Infrared Optoelectonics: Materials and Devices (MIOMD-VIII), Bad Ischl, Austria, 14.-16.5.2007

Acknowledgements

I would like to acknowledge all those, who assisted me with information and advices at various stages of this thesis. In particular I am very grateful to Prof. Gottfried Strasser for the opportunity to work in the highly sophisticated research unit at the Institute of Solid State Electronics at the Vienna University of Technology. I am very thankful for his constant advice and support.

I am greatly indepted to Maximilian Austerer for his unwearying assistance throughout this work. Further I would like to thank Stephan Schartner, Werner Schrenk, Pavel Klang, Michele Nobile, Gianmauro Pozzovivo, Sebastian Golka, Matthias Schramböck, Leonard Hoffmann and Max Andrews for their valuable suggestions and sharing their know-how.

In addition, I would like to thank Mykhaylo Semtsiv from the Department of Physics, Humboldt University Berlin, for supplying me with state of the art InP-samples and his great support during this thesis.

Finally, I want to thank my parents for making my studies possible and for their great support and patience.